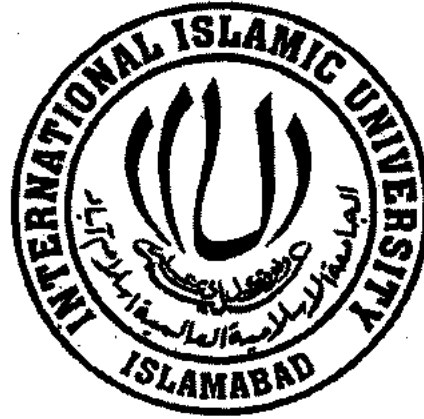


**Applications of Compressed Sensing to
Biomedical Imaging**



By

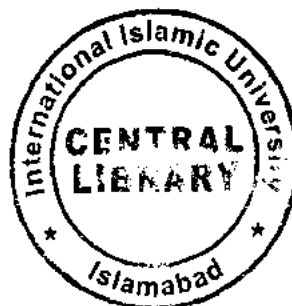
Jawad Ali Shah

Reg. No. 44-FET/PHDEE/F11

**A dissertation submitted to I.I.U. in partial
fulfillment of the requirements for the degree of**

DOCTOR OF PHILOSOPHY

**Department of Electronic Engineering
Faculty of Engineering and Technology
INTERNATIONAL ISLAMIC UNIVERSITY
ISLAMABAD
2015**



Accession No TH-14593 $\frac{1}{2}$

PhD
621.3822
SHA

Signal processing

Compressed sensing

Computed tomography

Magnetic resonance imaging (MRI)

10/1/2011
10/1/2011
10/1/2011

DATA ENTERED

Copyright © 2015 by J. Shah

All rights reserved. No part of the material protected by this copyright notice may be reproduced or utilized in any form or by any means, electronic or mechanical, including photocopying, recording or by any information storage and retrieval system, without the permission from the author.

DEDICATED TO

My Teachers,

Students

And

Friends

CERTIFICATE OF APPROVAL

Title of Thesis: Applications of Compressed Sensing to Biomedical Imaging

Name of Student: Jawad Ali Shah

Registration No: 44-FET/PhDEE/F11

Accepted by the Faculty of Engineering and Technology, International Islamic University, Islamabad, in partial fulfillment of the requirement for the Doctor of Philosophy in Electronic Engineering.

Viva voce committee:

Dr. Ihsan Ul Haq (Co. Supervisor)
Assistant Professor, DEE,FET, IIUI



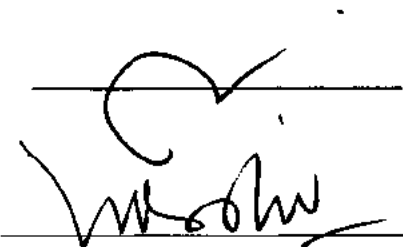
Dr. Ijaz Mansoor Qureshi (Supervisor)
Professor , DEE, Air University ,Islamabad.



Dr. Aqdas Naveed Malik (Internal Examiner)
Professor, DEE,FET,IIUI



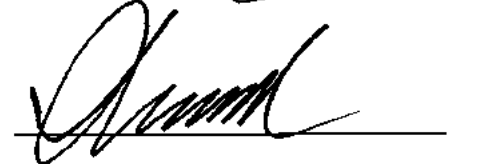
Dr Mohammad Usman (External Examiner)
POS , AERO , Wah Cantt.



Dr. Aamir Saleem Chaudary (External Examiner)
Professor, DEE, University of Lahore.



Dr. Muhammad Amir
Chairman, DEE, FET, IIUI



Dr. Aqdas Naveed Malik
Dean, FET, IIU, Islamabad

ABSTRACT

The application of compressed sensing (CS) to biomedical imaging is exciting because it allows a reasonably accurate reconstruction of images from far fewer measurements. For biomedical imaging, CS can increase the imaging speed and consequently decrease the radiation dose. While the idea of CS has been used to reduce the acquisition time of magnetic resonance imaging (MRI), x-ray computed tomography (CT) and microwave imaging (MWI), unfortunately the computation time of image recovery has increased as the nonlinear CS reconstruction algorithms are fairly slow. Reconstructing high-dimensional signals or biomedical images from compressively sampled data is a fundamental challenge faced by the CS.

In this dissertation, we propose a suite of novel CS recovery methods that can efficiently recover the Fourier encoded biomedical images (MRI, parallel-beam CT and MWI) from a small set of randomized measurements. The initial part of the current work presents CS based reconstruction of sub-sampled biomedical imaging modalities using projection onto convex sets (POCS) and separable surrogate functional (SSF) methods. The iterative shrinkage based SSF algorithm incorporates the linear estimate of the error to improve the reconstruction quality. It does not involve any matrix inversion and is used to estimate the missing Fourier samples of the original image by applying data consistency in the frequency domain and soft thresholding in the sparsifying domain. The idea of using hybrid evolutionary techniques for the sparse signal recovery is presented next. It proposes how to combine the heuristic techniques such as Differential evolution (DE), genetic algorithms (GA), and Particle Swarm Optimization (PSO) with

iterative shrinkage algorithms to faithfully reconstruct sparse signals from a small number of measurements. Based on the notion of GA, a modified POCS based algorithm is developed. This novel CS recovery technique uses two different estimates for the initialization and iteratively combines them to recover the original Fourier encoded image.

In the last part, we use hyperbolic tangent function separately to develop a reconstruction algorithm and a non-linear shrinkage curve for thresholding. As the l_1 -norm penalty is not differentiable, the proposed hyperbolic tangent based function is used to closely approximate the l_1 -norm regularization by a differentiable surrogate function. Using the method of gradient descent, a simple update rule is developed. The algorithm is shown to perform well for one dimensional (1-D) sparse signal recovery as well as CS reconstruction of Fourier encoded biomedical imaging. The idea is further extended by using hyperbolic tangent based approximations for the soft-thresholding that provide flexibility in terms of its adjustable parameters. Besides using synthetic data, the effectiveness of the proposed techniques are also validated using the real data collected from the MRI and MWI scanners.

LIST OF PUBLICATIONS AND SUBMISSIONS

- [1] **J. Shah**, I. Qureshi, H. Omer, and A. Khaliq, "A modified POCS-based reconstruction method for compressively sampled MR imaging," *International Journal of Imaging Systems and Technology*, vol. 24, pp. 203-207, 2014, John Wiley & Sons.
- [2] **J. Shah**, I. Qureshi, H. Omer, A. Khaliq, and Y. Deng, "Compressively sampled MR image reconstruction using separable surrogate functional method", *Concepts in Magnetic Resonance, Part A*, John Wiley & Sons. 2014. DOI: 10.1002/cmr.a.21314.
- [3] **J. Shah**, I. Qureshi, J. Proano, Y. Deng, "Compressively Sampled Fourier encoded Image Reconstruction using hyperbolic tangent based soft-thresholding", '*Applied Magnetic resonance*'. DOI: 10.1007/s00723-015-0683-2.
- [4] **J. Shah**, I. Qureshi, Y. Deng, A. Khaliq, "Reconstruction of Sparse Signals and Compressively Sampled Biomedical Images Based on Smooth l_1 -Norm Approximation", **submitted to** '*Journal of Signal Processing Systems*'.
- [5] **J. Shah**, I. Qureshi, A. Khaliq, H. Omer, "Sparse Signal Recovery based on Hybrid Genetic Algorithm" , *Research Journal of Recent Sciences*, vol. 3(5), pp. 86-93, 2014, ISSN 2277-2502.
- [6] **J. Shah**, I. Qureshi, A. Khaliq, H. Omer, "Sparse Signal Reconstruction from Compressed Measurements using Hybrid Differential Evolution", *World Applied Sciences Journal*, vol. 27 (12), pp. 1614-1619, 2013, ISSN 1818-4952.
- [7] **J. Shah**, I. Qureshi, A. Khaliq, M. Iqbal, "Adaptive equalization of a nonlinear recursive channel using Gaussian RBF based network". *IEEE 15th International Multitopic Conference (INMIC) 2012*.

- [8] H. Haider, **J. Shah**, U. Ali, "Comparative Analysis of Sparse Signal Recovery Algorithms based on Minimization Norms". *World Congress on Sustainable Technology 2014*.
- [9] H. Haider, **J. Shah**, I. Qureshi, H. Omer, "Compressively Sampled MRI Recovery using Modified Iterative Reweighted Least Square Method", **submitted to 'Inverse Problem and Imaging Journal'**.
- [10] S. Khursheed, A. Khaliq, S. Abdullah, **J. Shah**, S. Khan "Poisson noise removal using wavelet transforms", *Science International*.
- [11] A. Khaliq, I. Qureshi, **J. Shah**, "Source Extraction from Functional magnetic resonance imaging (fMRI) data using ICA based on Fourth order and Exponential contrast functions", *Journal of the Chinese Institute of Engineers*, vol. 36 (6), 730-742, 2013.
- [12] A. Khaliq, **J. Shah**, S. Malik, "De-noising of Functional Magnetic Resonance Imaging (fMRI) data using Nonlinear Anisotropic 1D and 2D filters", *International journal of advanced research in computer science*, vol. 4 (4), pp. 13-17, 2013.
- [13] A. Khaliq, I. Qureshi, Ihsanulhaq, **J. Shah**, "Detection of brain activity in functional magnetic resonance imaging data using matrix factorization", *Research journal of applied sciences, engineering and technology*, vol. 5(24), pp. 8566-8571, 2013
- [14] A. Khaliq, I. Qureshi, **J. Shah**, S. Malik, "High order Differential Covariance based source separation of Monkey's fMRI data", *International Journal of Engineering Sciences and Research Technology*, vol. 2 (5), pp. 1287-1292, 2013
- [15] A. Khaliq, I. Qureshi, **J. Shah**, S. Malik, Ihsanulhaq, "De-Noising Functional Magnetic Resonance Imaging (fMRI) data using Exponential Gradient filter", *Middle east journal of scientific research*, vol. 18 (9), pp. 1349-1356, 2013
- [16] S. Khursheed, A. Khaliq, **J. Shah**, S. Abdullah, S. Khan, "Third order NLM filter for Poisson noise removal from medical images", *MAGNT Research Reviews*, vol.2 (7): pp. 482-48

- [17] A. Khaliq, I. Qureshi, **J. Shah**, “Un-mixing Functional Magnetic Resonance Imaging (fMRI) data using Matrix Factorization”, *International journal of imaging system and Technology*, vol. 22 (4), pp. 195-199, 2012 John Wiley & Sons.
- [18] A. Khaliq, I. Qureshi, **J. Shah**, “Temporal Correlation based spatial filtering of Functional MRIs”, *Chinese Physics Letters*, vol. 29(1), 2012.

Awards and Grants

- Award of scholarship by Higher Education Commission (HEC) Pakistan under “International Research Support Initiative Program (IRSIP)” for six months research fellowship at Electromagnetic and Accoustic Imaging and Prognostics (LEAP) lab of the University of Colorado Denver/Anschutz Medical Campus USA covering:
 - Stipend (9000 USD)
 - Bench fee (2500 USD)
 - Travel grant (150 USD)

- Full fee waiver for PhD studies by the International Islamic University Islmabad (IIUI), Pakistan.

- Grant of study leave for nine months with full pay.

ACKNOWLEDGEMENTS

This dissertation would have not been written without the consistent support and encouragement from many colleagues, family members and friends that surround me. First, I would like to express my gratitude to Dr. Ijaz Mansoor Quershi, my PhD supervisor, mentor, teacher, brother and friend. He has been an inspiring figure and role model for me since I joined the teaching profession. I am also grateful to my foreign supervisor, Dr. Yiming Deng, for his valuable suggestions and ideas that has a great influence on my research work. I really appreciate the unbounded support of Dr. Julio Proano for providing useful and valuable comments, reviews and suggestions about my work. I owe a lot to Dr. Hammad Omer who introduced me to the fascinating area of MRI and provided access to original MR scanner data.

It has been an absolute pleasure and honor to be the student of Dr. Aqdas Naveed Malik from whom I learned and benefited a lot. He is one of my ideal teachers. The role and support of Dr. Ihsanul Haq during my PhD course work was exceptional. His encouraging approach is always a source of motivation for me.

My sincere thanks also goes to my colleagues: Dr. Muhammad Amir, Dr. Adan Umer, Dr. Saeed Badshah, Dr. Muhammad Afzal Khan and Dr. Suheel Abdullah. I have been fortunate to receive their long-standing support during each stage of PhD and throughout difficult times. I am also grateful to Engr. Hassaan Haider and Engr. Shahid Ikram for the experience of working with them, guiding them and learning so much from them in the process.

I would like to acknowledge and express my gratitude to Higher Education Commission (HEC) Pakistan for providing me the opportunity to conduct my six months research at the UC Denver, USA. I am also indebted to Pakistani-origin US citizens: Ehsan Gillani, Tahseen Ibrahim, Faqir Mohammad (FM), Ahmad Zia, Muhammad Imran, Ahsan Awan, Naseer and Rukhsana Baji who provided me a home-like environment in Denver and never realized me that I am away from Pakistan.

I would like to acknowledge the support of International Islamic University Islamabad Pakistan for providing me nine months study leave and full fee waiver during the PhD studies. It was indeed a generous award and investment from my university.

The biggest thanks goes to my family members: My father (late), mother, sisters and brothers. It is only because of their love, never-ending support and prayers that I could do this or anything else. I owe a lot to my devoted wife for her unending encouragement and patience. Finally, I express my special gratitude to my kids: Ahmad Mujtaba, Abdul Mohaimin and the newcomer Abdul Mannan for always making me smile and allowing me to utilize their time in my research against their wishes!

(Jawad Ali Shah)

Table of Contents

Abstract.....	iv
List of Publications and submissions.....	vi
Awards and Grants.....	ix
ACKNOWLEDGEMENTS.....	x
List of figures.....	xvi
List of Tables.....	xxi
List of abbreviations.....	xxii
CHAPTER-1 Introduction.....	1
1.1 Compressed Sensing.....	3
1.2 Main Contributions.....	4
1.3 Thesis Outline.....	6
CHAPTER-2 Sparse Representation and Compressed Sensing.....	8
2.1 Sparse Representation.....	8
2.1.1 Sparsity: From Basis Expansion to Sparse Representation.....	8
2.2 Compressed Sensing for Biomedical Images.....	11
2.2.1 Sparsifying transforms for biomedical images.....	12
2.2.2 Non-Linear Recovery.....	25

2.3	Related Work.....	27
2.4	Quality assessment parameters.....	30
2.5	Summary	31
CHAPTER-3 Biomedical Imaging Modalities and Projection onto Convex Sets Based CS recovery.....		32
3.1	Magnetic Resonance Imaging (MRI).....	32
3.2	Parallel beam CT.....	38
3.2	Microwave Imaging (MWI).....	40
3.3	POCS based Recovery of Fourier encoded images.....	43
3.4	Summary	49
CHAPTER-4 Compressively sampled Fourier-encoded image reconstruction using Seperable Surrogate Functional.....		50
4.1	Rapid imaging and compressed sensing.....	50
4.2	l_1 -regularized least square problem for Orthonormal basis	52
4.3	Proposed Recovery algorithm	54
4.4	Recovery of MR images using the proposed algorithm	56
4.5	Recovery of parallel beam CT using the proposed method	61
4.6	Reconstruction of MWI using SSF based method	63
4.7	Summary	65
Chapter-5 Sparse signal reconstruction using hybrid evolutionary algorithms.....		67

5.1	Evolutionary algorithms	67
5.2	The Proposed Hybrid Particle Swarm Optimization	70
5.3	Proposed Hybrid Genetic Algorithm	72
5.4	Results and Discussions	73
5.4	Proposed modified POCS algorithm for biomedical images	76
5.5	Summary	80
Chapter-6 CS Recovery Based on Smooth l_1-Norm Approximation		81
6.1	Problem Statement	81
6.2	Proposed hyperbolic Tangent based surrogate function	82
6.3	Proposed Recovery Algorithm	85
6.4	Results of Simulation with Discussions	87
6.5	Summary	96
Chapter-7 A flexible soft thresholding for Iterative Shrinkage algorithms		98
7.1	CS Recovery and denoising	98
7.2	MAP estimator for denoising and proposed thresholding.....	102
7.3	CS recovery of biomedical imaging (Denoising approach)	106
7.4	Experimental results.....	107
7.5	Summary	112
CHAPTER-8 Conclusion.....		113
8.1	Summary of thesis	113

8.2	Directions for future work.....	115
	References.....	117

LIST OF FIGURES

Figure-2.1: DCT basis $\psi_{l,j}(l, p)$ for $0 \leq l, j \leq 7$	13
Figure-2.2: Original and reconstructed microwave image from 10% DCT coefficients	14
Figure-2.3: Block diagram of the QMF algorithm for DWT.....	15
Figure-2.4: Block diagram for IDWT using QMF algorithm	16
Figure-2.5: Original MR Image of human head	17
Figure 2.6: 7-bands of Daubechies 2-tap filters when applied to brain MRI.	17
Figure-2.7: Sorted coefficients of MRI in pixel and wavelet domain. Only 1000 significant values are shown for comparison.....	18
Figure-2.8: Gradient based sparsity of Shepp-Logan image	19
Figure-2.9: Aliasing due to linear reconstruction of MRI from its partial Fourier data	22
Figure-2.10: Different domains and transformations in CS.....	22
Figure-2.11: Behavior of scalar function $ \alpha ^p$	26
Figure-3.1 Pulse sequence diagram representing various gradients for spatial encoding	34
Figure-3.2: Fourier encoded MR image.....	36
Figure-3.3: Aliasing due to the uniform undersampling of k -space	37
Figure-3.4: Effect of undersampling the k -space on reconstructed image.....	38

Figure-3.5: Projections in parallel beam CT.....	39
Figure-3.6: Radial lines used to sample the Fourier transform of an object for CT imaging	41
Figure-3.7: Measurement configuration for MWI.....	42
Figure-3.8: POCS algorithm (with block diagram) for Fourier-encoded image recovery	44
Figure-3.9: Recover of compressively sampled MRI using POCS	46
Figure-3.10: Effect of thresholding parameter on the quality (MSE) of reconstructed MR image.....	47
Figure-3.11: Original MWI along with the undersampling pattern.....	48
Figure-3.12: POCS based recovery of compressively sampled MWI.....	48
Figure-4.1: The proposed SSF based recovery algorithm (with block diagram).....	56
Figure-4.2: Original phantom and brain images taken from the MRI scanner.	57
Figure-4.3: Recovery (phantom MRI) using various techniques.....	58
Figure-4.4: Recovery of phantom image with proposed algorithm.	59
Figure-4.5: Comparison (phantom MR image) based on Structural similarity (SSIM)	59
Figure-4.6: Comparison based on ISNR (brain image)	60
Figure-4.7: Comparison on the basis of fitness value (brain image).....	60
Figure-4.8: Difference of the recovered images with the original brain image.	61
Figure-4.9: CT phantom image (a) and corresponding sinogram (b).....	62

Figure-4.10: (a) undersampling pattern (b) aliased CT image.....	62
Figure-4.11: Final reconstructed CT image with various algorithms	63
Figure-4.12: fully sampled SAR image of SUT	64
Figure-4.13: Selective raster scanning for MWI acquisition	64
Figure-4.14: Under-sampled (top) and recovered microwave image (bottom)	65
Figure-5.1: Flow chart of generic GA.....	69
Figure-5.2: The proposed hybrid PSO algorithm	71
Figure-5.3: The proposed hybrid genetic algorithm for sparse signal recovery	72
Figure-5.4: Performance of PSO with varying inertial weights	73
Figure-5.5 showing fast convergence achieved with the proposed method	74
Figure-5.6: Signal reconstruction through conventional and hybrid PSO.....	75
Figure-5.7: Comparison of hybrid GA based on mean-square-error	75
Figure-5.8: Modified POCS based algorithm for CS recovery.....	77
Figure-5.9: Final image recovery with modified POCS algorithm.....	78
Figure-5.10: Comparison of proposed algorithm with POCS and SSF	79
Figure-6.1 Comparison of approximation for different values of γ	84
Figure-6.2 Mean-square error of the approximation for different bounds of signal....	84
Figure-6.3: Graphical solution to Eq-6.7 corresponding to $\gamma = 50$	86
Figure-6.4: Proposed hyperbolic tangent based iterative algorithm for (1-D) sparse recovery.....	87

Figure-6.5: Compressively sampled sparse signal.....	88
Figure-6.6: Recovery with the proposed reconstruction algorithm	89
Figure-6.7: Signal recovery with and without knowledge of sparsity	90
Figure-6.8: Proposed hyperbolic tangent based algorithm for CS recovery of Fourier encoded imaging.....	91
Figure-6.9: Phantom image and the under-sampling pattern used	92
Figure-6.10: Recovery of phantom image (parallel-beam CT) with proposed algorithm	92
Figure-6.11: Original human head MR image and the corresponding sampling pattern	93
Figure-6.12: Recovery of original MR image using proposed algorithm.....	94
Figure-6.13: SSIM improvement of the reconstruction images in each iteration.....	94
Figure-6.14: SAR image and corresponding under-sampling pattern used.....	95
Figure-6.15: Under-sampled and recovered microwave image	96
Figure-7.1: Transformed based denoising	99
Figure-7.2: Histogram of error (between original Fourier encoded image and linear reconstructed image) for (a) parallel beam CT (b) MRI.....	101
Figure-7.3: Reduction in the variance of error during CS recovery	101
Figure-7.4: Versatility of the hyperbolic-tangent based soft-thresholding.....	104
Figure-7.5: Approximation of Eq-7.10 using the proposed soft-thresholding (Eq-7.11)	104
Figure-7.6: performance of the proposed thresholding function	105

Figure-7.7: A general denoising based CS recovery algorithm.....	107
Figure-7.8: Distribution of pixel values of the original MR image	108
Figure-7.9: Distribution of pixel values of the original undersampled image.....	109
Figure-7.10: Distribution of pixel values of the reconstructed image	109
Figure-7.11: Improvement in correlation using soft (Eq-7.10) and proposed (Eq-7.11) thresholding function for MR recovery	110
Figure-7.12: Reconstruction of MR phantom image using thresholding of Eq-7.11	111
Figure-7.13: Comparison based on SSIM using two different thresholding	111
Figure-7.14: SSF based Original MR Image reconstruction using soft-thresholding (Eq-7.10) and the proposed (Eq-7.11)	112

LIST OF TABLES

Table-3.1 Values of MSE and correlations attained by the final MR image.....	47
Table-4.1: Comparison of MR brain image based on PSNR, AP and correlation.....	61
Table-5.1: Values of various parameters such as correlation, MSE etc. achieved by different recovery algorithms.....	76
Table-5.2: Comparison of algorithms for MR image reconstruction	79
Table-6.1: Comparison based on various performance metrics.....	96

LIST OF ABBREVIATIONS

AP	Artifact Power
BP	Basis Pursuit
CoSaMP	Compressively Sampled Matching Pursuit
CT	Computed Tomography
CS	Compressed (or compressive) Sensing (or sampling)
DAQ	Data Acquisition
dB	Decibel
db2	Daubechies-2
DCT	Discrete Cosine Transform
DE	Differential Evolution
DFT	Discrete Fourier Transform
DWT	Discrete Wavelet Transform
FBP	Filtered Back Projection
FID	Free Induction Decay
FOV	Field of View
fMRI	Functional Magnetic Resonance Imaging
GA	Genetic Algorithms
IDCT	Inverse Discrete Cosine Transform
IDFT	Inverse Discrete Fourier Transform
IDWT	Inverse Discrete Wavelet Transform
IHT	Iterative Hard Thresholding
ISNR	Improved-Signal-to-Noise Ratio
IST	Iterative Shrinkage Thresholding
LMS	Least-mean-square
LR	Low Resolution
RF	Radio Frequency
RIP	Restricted Isometry Property
SPECT	Single Photon Emission Computed Tomography
SSF	Separable Surrogate Functional
SSIM	Structural Similarity Index

SNR	Signal-to-Noise Ratio
SUT	Sample Under-test
MAP	Maximum a posteriori probability
MSE	Mean Square Error
MWI	Microwave Imaging
NP	Non-deterministic Polynomial-time
OMP	Orthogonal Matching pursuit
PCD	Parallel Coordinate Descent
PET	Positron Emission Tomography
pdf	Probability density function
POCS	Projection Onto Convex Set
PSO	Particle Swarm Optimization
PSNR	Peak Signal-to-Noise Ratio
TV	Total Variation
ZF	Zero-Filling

CHAPTER-1

INTRODUCTION

Medical imaging techniques such as Magnetic Resonance Imaging (MRI), x-rays Computed Tomography (CT) and Microwave Imaging (MWI) etc. are becoming increasingly important tools in medical decision making that offer useful information about the medical conditions of the patients.

Unlike CT scanners which generate images by passing x-ray (ionizing) radiations through the body, MRI is considered to be a nonionizing and non-invasive imaging modality as it uses magnet and radio waves to produce images. MRI provides excellent depiction of soft tissue contrast and its variant, known as Functional MRI (fMRI) can be used to record the functional activities of the brain by measuring the associated changes in the blood flow. However, MRI is much slower and takes longer acquisition time than CT.

Microwave imaging is another promising modality that is based on the scattering phenomena of microwave signals (1GHz to 30 GHz). Microwave radiations can penetrate inside the human body and can retrieve various structural and functional information based on the tissue water content. It is a noninvasive imaging modality and is becoming popular because of its ability to detect breast cancer in the early stages.

The recent technological advancement in the field of biomedical imaging has resulted in massive clinical data. It is therefore necessary to find methods and tools that can sparsely represent the biomedical data. This will not only reduce the storage requirements but will also be beneficial in extracting the useful information efficiently thereby reducing the diagnosis time. There is another challenging problem related to

the data acquisition. The scanners used to acquire these images are generally claustrophobic, loud, slow, uncomfortable, and may involve exposure of patient to the harmful radiations. In order to get a high resolution image, the Nyquist rate is very high. So, it is necessary to reduce the massive amount of the acquired data for the following purposes:

1. To speed up the long acquisition time and increase the imaging rate to achieve a full or nearly real-time monitoring.
2. To obtain high resolution in time, and high resolution in 3-dimensional space of internal body structure for image-guided surgery imaging.
3. To minimize the processing/diagnosis time and less exposure of patient to the ionizing radiation dose as in the case of CT.
4. To alleviate discomfort of the patients because of the slow acquisition, even if there are no hazards of EM radiations as in the case of MRI, fMRI and MWI.
5. To keep the dataflow tractable for diagnosis and follow-up of human diseases.
6. To reduce to the storage size and save battery power in case of wireless applications such as telemedicine.

The accelerated acquisition time can also reduce the motion artifacts due to respiratory and cardiac cycles which is a common issue in dynamic cardiac imaging. Furthermore, in biomedical imaging via neutron scattering, limited sensors may be available or measurements may be extremely expensive. Therefore, reconstructing a high quality image from reduced number of measurement may be highly cost-effective.

While the underlying principle and physical quantities being imaged by CT, MRI and MWI are different but their scanners naturally acquire the encoded samples instead of direct pixel values. So the acquisition process can be modeled by a set of linear

measurements of the form $y = \Phi x$, making these imaging modalities a potential application for the CS.

1.1 Compressed Sensing

Like natural images taken by digital cameras, biomedical images can also be compressed using popular compression techniques. However, in the conventional transform coding such as JPEG and JPGE-2000 etc., the measurements of the image are acquired first (through Nyquist criteria) and then using a sparsifying transforms e.g. Discrete Cosine (DCT) and Wavelet Transforms (DWT), most of the small energy coefficients are discarded to achieve the desired level of compression. This sample-then-compress framework of conventional compression methods introduces extra overhead thus making these algorithms inefficient.

Compression using transformed coding is essentially a post-processing operation. In recent years, a new data acquisition protocol known as compressive (or compressed) sampling (or sensing) has seen enormous growth and interest in the areas of signal/image processing, information theory, statistics and neural networks. The theory of compressed sensing (or sampling) suggests that a sparse or compressible signal can essentially be recovered using measurement rates below the conventional Nyquist rate [1-3].

A sparse signal is one that has many zero and few nonzero coefficients. CS uses non-linear recovery techniques to reconstruct the original sparse signal from small number of non-adaptive random projections that are proportional to the sparsity level of the signal, instead of its ambient dimensionality [4-5].

Contrary to the transform coding, CS suggests that the encoding process can be made efficient by combining the compression step directly with the acquisition thus avoiding

the unnecessary information to be captured and processed. CS has enormous practical applications in biomedical imaging such as MRI, fMRI, CT and MWI which involves slow acquisition process. Three essential requirements for the application of compressed sensing to biomedical images are the image sparsity, incoherent sampling and non-linear reconstruction algorithm [6-8].

The encoder part of CS is relatively simple and consists of the non-adaptive and incoherent linear measurements of the form $\mathbf{y} = \Phi\mathbf{x}$. However, the CS decoder is very challenging because of the computation cost in the (nonlinear) image reconstruction process. Many reconstructions algorithms have been proposed for compressed sensing in the recent past. However, most of these algorithms are general purpose and require too many iterations making the recovery inefficient, specifically if the images have large dimensions as in the case of biomedical applications [9-11].

The numerical algorithms used for the sparse signal recovery frequently involve finding solution to the least squares optimization problem with l_1 -norm regularization. As the l_1 -norm penalty is not differentiable, so it rules out the possibility of using the efficient optimization techniques that call for the derivative of the objective function. Devising an efficient and lower cost CS recovery technique for high dimensional biomedical images is still considered as one of the fundamental challenging task which is the main focus of this dissertation.

1.2 Main Contributions

This work is motivated by the desire to propose a number of efficient reconstruction methods for compressively sampled biomedical imaging modalities such as MRI, parallel-beam CT and MWI. The proposed recovery algorithms are based on the iterative shrinkage methods which are well suited for large dimensional signals. These

suits of algorithms estimate the original image from its perturbed observation (measurements) and therefore recast the reconstruction as denoising or interference cancellation problem.

The dissertation also presents some novel work related to the shrinkage curves used for soft-thresholding. A flexible hyperbolic tangent function is proposed for approximating the shrinkage curve. Hyperbolic tangent function is also used in a totally different context to surrogate the l_1 -norm by a differentiable function for developing a gradient based sparse reconstruction algorithm.

The main contributions of this work are summarized below:

Development of fast and efficient CS recovery techniques for Fourier encoded biomedical imaging using the family of iterative-thresholding algorithms. By incorporating data consistency constraint in the Fourier domain, computationally low-cost sparse recovery algorithms such as separable surrogate functional (SSF) and parallel coordinate descent (PCD) are shown to perform well in CS recovery of biomedical images .

Sparse signal reconstruction has been carried out using heuristic techniques such as differential evolution (DE), genetic algorithm (GA) and particle swarm optimization (PSO). It has been shown that, by using deterministic algorithm, the convergence speed of evolutionary algorithm can be improved.

Using the idea of GA, a modified projection onto convex set based algorithm is developed for the recovery of compressively sampled MR images.

A novel sparse recovery algorithm is proposed to surrogate the l_1 -norm by a differentiable function. The algorithm is shown to efficiently recover MRI, parallel-beam CT and MWI from sub-Nyquist measurements.

A flexible hyperbolic tangent based soft-thresholding is proposed. The novel thresholding is shown to perform well with iterated-shrinkage algorithms to recover the biomedical images from compressive measurements. The proposed nonlinear function can also be used in place of soft-thresholding for imaging denoising.

The proposed techniques are applied to various biomedical imaging modalities using phantom as well as original images from the scanners. All the results related to MRI experiments are validated using the real brain images taken from the MRI scanner at St. Mary's Hospital, London. The microwave imaging uses a phantom image developed at the Laboratory of Electromagnetic and Acoustic Imaging and Prognostics (LEAP), University of Colorado Denver, USA.

1.3 Thesis Outline

The rest of the thesis is organized as follows:

Chapter-2 starts with an introduction of sparse representation and compressed sensing with special focus on biomedical imaging modalities. It also provides a brief literature review of the related work, followed by the quality assessment metrics used in the CS reconstruction methods.

Chapter-3 provides the underlying physics and mathematical details to show that the data acquisition of MRI, parallel CT and MWI scanner can be model as a Fourier encoded measurement process, making it a potential application for the compressed sensing. POCS based algorithm is then applied to recover MR, CT and microwave images from sub-sampled measurements.

Chapter-4 presents the mathematical detail of SSF based CS recovery algorithm. It incorporates the linear estimate of the residual error in POCS algorithm to further

improve the reconstruction quality. The viability of the technique is used to reconstruct Fourier encoded images from a reduced dataset.

Chapter-5 provides two hybrid sparse recovery algorithms based on evolutionary techniques. Particle swarm optimization and genetic algorithms are combined with SSF to speed up the convergence. Based on the idea of GA, a novel CS reconstruction method for Fourier encoded imaging is also presented. The novel approach uses multiple initialization and randomly combines two estimates to reconstruct the final image.

Chapter-6 is based on the differentiable surrogate approximation of l_1 -norm. The proposed smooth function is used to develop an iterative algorithm for the CS reconstruction using a simple gradient descent for the solution update. The results are validated to recover 1-D sparse signal, original MR, CT and MW images.

Chapter-7 starts by providing an equivalence between undersampling and denoising. It presents a novel thresholding scheme based on hyperbolic tangent function. This flexible thresholding can be used with any of the iterative shrinkage algorithm for the recovery of biomedical images as well as denoising.

Chapter-8 concludes the work along with the future work.

CHAPTER-2

SPARSE REPRESENTATION AND COMPRESSED SENSING

This chapter revisits the basic concepts of sparse representation and compressed sensing, mainly in the context of biomedical imaging modalities such as MRI, CT and MWI. It also provides a brief description of the background work related to the application of compressed sensing to various biomedical imaging. Different quality assessment parameters used in the experimental work are also discussed.

2.1 Sparse Representation

Sparse representation aims to approximate an image or signal in the most parsimonious way by representing it as a linear combination of few elementary signals (known as the basis or atoms) drawn from a fixed collection (called dictionary) [9-10]. The sparse representation for a signal or image gives us the advantage of fast computation, less storage requirement and efficient transmission. The recently developed theory of compressed sensing (CS) has further revolutionized the field of sparse signal approximation with the claim that a sparse signal can be recovered from far few measurements that are needed by the conventional Nyquist theorem [1-4].

2.1.1 Sparsity: From Basis Expansion to Sparse Representation

Basis representation breaks up the (discrete and continuous time) signals as a linear combination of fixed basis signals (atoms). In its general form, the basis expansion of a signal $x(t)$ can be expressed as [12]:

$$x(t) = \sum_{\gamma \in \Gamma} \alpha_{\gamma} \psi_{\gamma}(t) \quad (2.1)$$

where $\{\psi_{\gamma}(t)\}_{\gamma \in \Gamma}$ is a fixed set of basis signals, α_{γ} is a discrete list of numbers called the transformed coefficients and $\Gamma \in \mathbb{Z}$ is a discrete index set.

The basis expansion of Eq-2.1 discretizes a signal $x(t)$ by translating it into discrete list of numbers (α_{γ}) in such a way that the signal can be reconstructed. It is also referred to as the ‘‘atomic decomposition’’.

If the basis are orthonormal i.e. $\langle \psi_{\gamma}, \psi_{\gamma'} \rangle = \delta(\gamma - \gamma')$, the coefficients can be computed through a simple inner product:

$$\alpha_{\gamma} = \langle x(t), \psi_{\gamma}(t) \rangle \quad (2.2)$$

The well-known examples of orthonormal basis expansion are the continuous and discrete time Fourier series, discrete Fourier transform (DFT), Sinc interpolation or reconstruction, convolution, DCT and wavelet.

Mathematically, any real or complex-valued DT signal of length n can be treated as (column) vector in an n -dimensional space. Similarly, a (gray-scale) biomedical image X can be represented by a matrix. However, without loss of generality, the biomedical images can be brought into a vector form by stacking all its columns into a single vector. Thus, for the discrete case ($x \in \mathbb{R}^n$), Eq-2.1 can be written as [13]:

$$x = \sum_{l=0}^{n-1} \alpha_l \psi_l = \sum_{l=0}^{n-1} \langle x, \psi_l \rangle \psi_l = \Psi^H \alpha \quad (2.3)$$

where α_l are the expansion coefficients and $\alpha \in \mathbb{C}^n$ is the representation vector. The operator $\Psi = [\psi_0 \ \psi_1 \ \dots \ \psi_{n-1}]$ is a unitary matrix (i.e. $\Psi \Psi^H = \mathbf{I}$), known as the basis matrix or dictionary or sparsifying transform. In the classical example of Fourier series,

ψ_i are harmonically related complex sinusoids, Ψ is the normalized Fourier matrix and α_i are the Fourier coefficients.

Eq-2.3 represents a linear system with the same number of equations as unknowns. As Ψ is a square and invertible matrix ($\Psi^{-1} = \Psi^H$) having no null-space, the representation of signal \mathbf{x} is unique [14].

An orthonormal basis representation of the signal has the following advantages:

- i. The transformed coefficients α_i may carry semantic information such as the frequency contents (as in the case of Fourier series or DFT).
- ii. According to the Parseval theorem, energy of the original signal is preserved in its transformed coefficients i.e. $\|\mathbf{x}\|_2^2 = \|\boldsymbol{\alpha}\|_2^2$, where $\|\cdot\|_2$ represents the Euclidean norm corresponding to $p = 2$ of the general l_p -norm defined as:

$$\|\mathbf{x}\|_p = \left(\sum_{i=1}^n |x(i)|^p \right)^{\frac{1}{p}} \quad (2.4)$$

- iii. The expansion gives a discrete representation even for the continuous time signals. The coefficients can therefore be processed through digital computers.
- iv. The transformation may provide the energy compaction that leads to the sparse representation of the signal or images.

A simple example of the energy compaction property can be seen in the Fourier series, where the Fourier coefficients of a signal falls off quickly if it has more derivatives (in time domain), leading to an implicit compression in the frequency domain.

Energy compaction property has a direct relation with the sparse representation. If a signal or image \mathbf{x} can be represented as a superposition of k atoms in the Ψ -domain,

then the column vector α is known as the k -sparse representation of x and Eq-2.3 can be re-written as [11]:

$$x = \sum_{i=1}^k \alpha_{n_i} \psi_{n_i}$$

where the k set of indices $\{n_i\}_{i=1}^k$ correspond to the k non-zero entries of the coefficients of the basis signals. The representation vector $\alpha \in \mathbb{R}^n$ is said to be k -sparse and will only have $k < n$ non-zero coefficients. Mathematically speaking, $\|\alpha\|_0 = k$ where $\|\cdot\|_0$ is the l_0 pseudo-norm defined as:

$$\|\alpha\|_0 = \lim_{p \rightarrow 0} \|\alpha\|_p^p = \lim_{p \rightarrow 0} \sum_{i=1}^n |\alpha(i)|^p = \#\{i: \alpha(i) \neq 0\} \quad (2.5)$$

Where it is assumed that $0^0 = 0$. Thus the l_0 quasi norm is a counting function that returns the number of non-zero elements (sparsity) of the signal.

Real world signals including biomedical images are seldom sparse in a transformed domain but are instead compressible. A compressible signal has magnitude of coefficients that decay according to a power law when sorted in a descending order. A compressible signal can be closely approximated by a sparse signal by setting all the small values of its coefficients equal to zero [15, 16].

2.2 Compressed Sensing for Biomedical Images

As the information contents of a sparse signal are much smaller than its bandwidth, one can design an efficient sampling scheme by taking the number of measurements proportional to its information contents. The theory of CS claims that for the class of sparse or compressible signals, the required number of measurements is usually smaller than the Nyquist limit and is instead proportional to the sparsity level of the signal. CS

is based on three important principles, namely sparsity, incoherent sampling or measurements and non-linear recovery which are discussed briefly below.

2.2.1 Sparsifying transforms for biomedical images

The most popular analytical transforms used for the sparse representation of biomedical images are discrete cosine transform, total variation and wavelet.

2.2.1.1 Discrete Cosine Transform (DCT)

DCT is an alternative to the Fourier series with the following two main differences that makes it more attractive for certain applications:

- i. The expansion coefficients and the (ortho) basis functions are real-valued.
- ii. Each basis has half integer number of cycle.

The (1-D) DCT basis for \mathbb{R}^n are defined as [17]:

$$\psi_i(l) = \begin{cases} \sqrt{1/n} , & i = 0 \\ \sqrt{2/n} \cos\left(\frac{\pi i}{n}\left(l + \frac{1}{2}\right)\right), & i = 1 \dots n - 1 \end{cases} \quad l = 0, 1 \dots n - 1 \quad (2.6)$$

For 2-D biomedical images, one can extend the 1-D DCT basis of Eq-2.6 into separable bases. Let $\psi_{i,j}(l, p)$ be the 2-D DCT basis for $\mathbb{R}^n \times \mathbb{R}^n$, then:

$$\psi_{i,j}(l, p) = \psi_i(l)\psi_j(p), \quad 0 \leq i, j \leq n - 1$$

As the bases $\psi_i(l)$ and $\psi_j(p)$ are orthogonal, the 2-D DCT basis $\psi_{i,j}(l, p)$ are also orthogonal. As an example, Fig-2.1 shows the 64 DCT basis functions for $n = 8$. The basis are indexed by two integers i and j an each basis comprises of 8×8 image block. So, any arbitrary 8×8 image patch can be represented as a weighted sum of these 64 different DCT basis functions (image block). The transformed domain (DCT)

coefficients can be obtained by a simple inner product of the image patch with each of these basis functions.

The DCT is widely used for image compression because of its ability to sparsify the images. The basic idea is that while the energy of an 8×8 image block is less evenly distributed in the pixel domain, the DCT concentrates this energy onto a relatively small number of transform coefficients. To demonstrate the energy compaction property of DCT, we apply it to a microwave image. Fig-2.2 shows a 6×1.5 inches near field microwave image developed at the Electromagnetic and Acoustic Imaging and prognostics (LEAP) lab of the University of Colorado Denver and Anschutz Medical Campus, using a customized coaxial tip antenna. The image was acquired by using raster scanning with excitation frequency =10 GHz. The image reconstructed from its 10% largest DCT coefficients is also shown in the figure. It is clear that by acquiring the most significant DCT coefficients, the original image can be reconstructed faithfully.

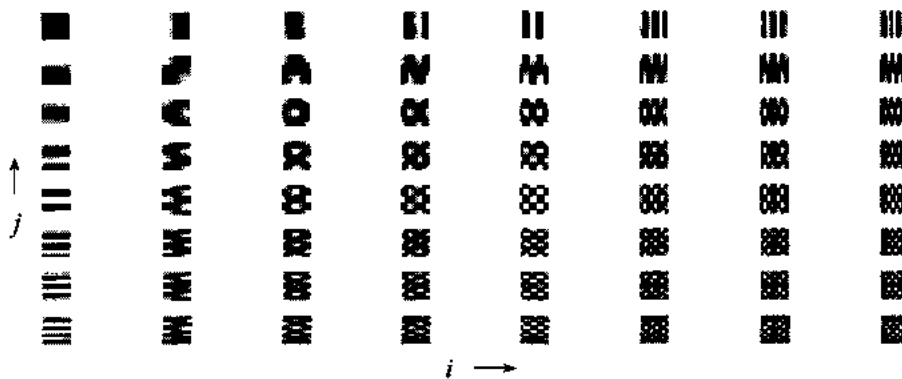


Figure-2.1: DCT basis $\psi_{i,j}(l,p)$ for $0 \leq i,j \leq 7$

Sparse representation with DCT is good if the image is smooth. However, it suffers when transforming a signal that has time varying and/or singularity characteristics.

There is a general issue with the transforms that are based on Fourier basis. The general Fourier basis uses complex exponentials which are periodic and time-unlimited. Once the signal is transformed using Fourier basis, it loses time information. So, in certain cases, it may not be the best solution to use it for the representation of time-limited signals or if temporal resolution is required. Wavelet transform is a useful tool and captures both frequency and time information of the signal [18].

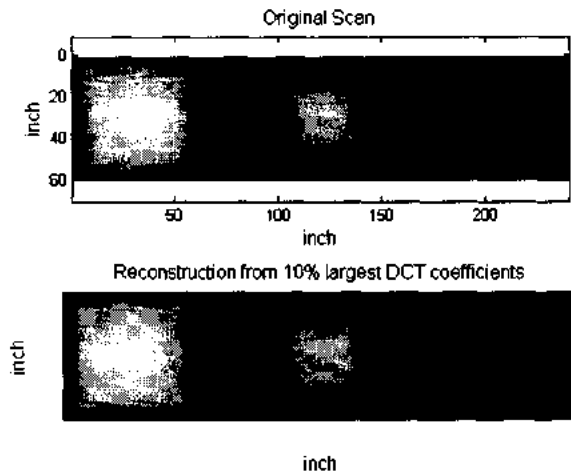


Figure-2.2: Original and reconstructed microwave image from 10% DCT coefficients

2.2.1.2 Wavelet Transform

The wavelet consists of a single time-limited basis function (“little wave”) that satisfies certain properties and is known as the mother wavelet. The entire library of the ortho-basis is created from it by the operations of time-shift and scaling. The wavelet representation of a 1-D, continuous-time finite energy signal is given by:

$$x(t) = \sum_{i,j} \alpha_{i,j} \psi_{i,j}(t) = \sum_{i,j} \langle x, \psi_{i,j} \rangle \psi_{i,j}(t) \quad (2.7)$$

where the wavelet basis $\psi_{i,j}(t)$ are indexed by two variables. These basis are reconstructed from a single mother wavelet $\psi(t)$. Changing the choice of $\psi(t)$ can lead

to different types of wavelet transforms. For the case of discrete wavelet transform (DWT), a typical wavelet is compressed i -times and shifted j -times to obtain the orthonormal basis i.e.

$$\psi_{i,j}(t) = \frac{1}{\sqrt{2^i}} \psi(2^{-i}t - j), i, j \in \mathbb{Z} \quad (2.8)$$

For a DT signal $x \in \mathbb{R}^n$, the DWT is computed by passing it through a series of low and high-pass filters. Using quadrature mirror filter (QMF) algorithm, the impulse response of the high-pass filter $g(i)$ is calculated from that of the low-pass filter $h(i)$ by the relation:

$$g(i) = h(2n - 1 - i), 0 \leq i \leq n - 1 \quad (2.9)$$

After filtering, half of the samples are retained by down-sampling (decimating) the outputs of the filters. The schematic diagram of (two-level) wavelet decomposition is shown in Fig-2.3.

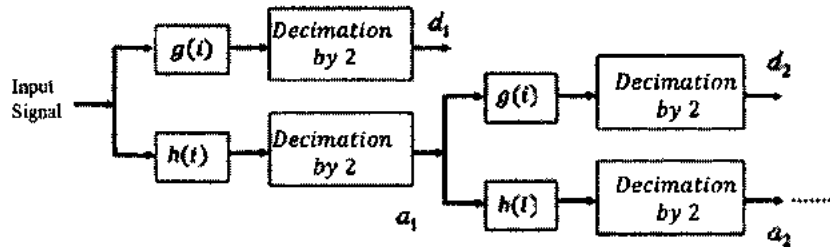


Figure-2.3: Block diagram of the QMF algorithm for DWT

The signal transformation is generally repeated for as many levels as desired by further decomposing the low-pass version of the signal.

The inverse discrete wavelet transform (IDWT) is computed by a similar multilevel process as shown in Fig-2.4. The impulse responses of the IDWT filters are calculated as follows:

$$h_1(i) = (-1)^{1-n}h(1-i)$$

$$g_1(i) = (-1)^{1-n}g(2n-1-i)$$

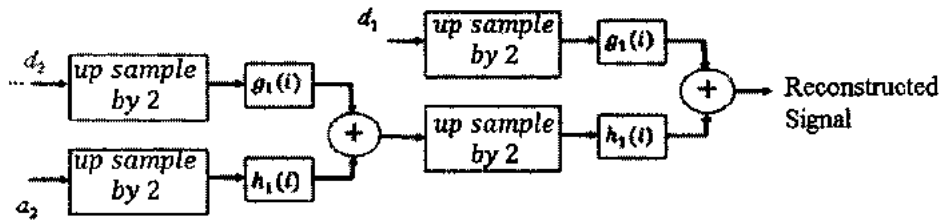


Figure-2.4: Block diagram for IDWT using QMF algorithm

Wavelets are extremely useful tools and are widely used for the sparse representation of biomedical images such as CT and brain MRI [6, 7]. They have the ability to automatically adapt to the singularities in the images. DWT is also used for compression in JPEG-2000 [5, 19].

The 2-D wavelet transform can be easily implemented for biomedical images. This is usually done by treating an $n \times n$ image once as a series of 1-D row signals and once as a series of 1-D column signals. The 1-D DWT for all the n -rows of the image is calculated first and the same process is repeated on the n -columns after that.

Fig-2.5 shows a real MR image of human head that was acquired at St. Mary's Hospital London using 1.5 Tesla GE HDxt scanner. To obtain its Daubechies-2 (db2) wavelet, the Haar transform is applied by filtering the image with 1-D kernels horizontally and applying the same filters vertically resulting in four output images. The process is further continued with the low-low pass image thereby resulting in a total of 7 images. The resulting 7 bands obtained using the Daubechies 2-taps filter ($h = [1/2, 1/2], g = [1/2, -1/2]$) with two layers of resolution are shown in Fig-2.6.

Original MR image



Figure-2.5: Original MR Image of human head

LL_2	LH_2	LH_1
HL_2	HH_2	
HL_1		HH_1

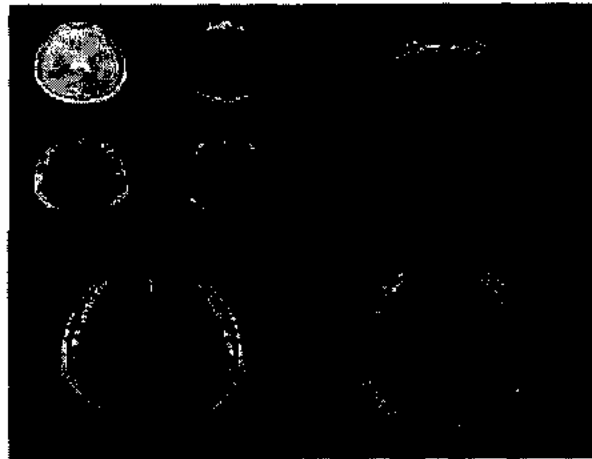


Figure 2.6: 7-bands of Daubechies 2-tap filters when applied to brain MRI.

Furthermore, Fig-2.7 demonstrates the compressibility of the MR image (Fig-2.5) in the Wavelet domain. The figure is obtained by sorting the pixel values and wavelet coefficients in descending order. The rapid decay of the wavelet coefficients of the MR image shows that it can have a nearly sparse representation in the transformed (wavelet) domain

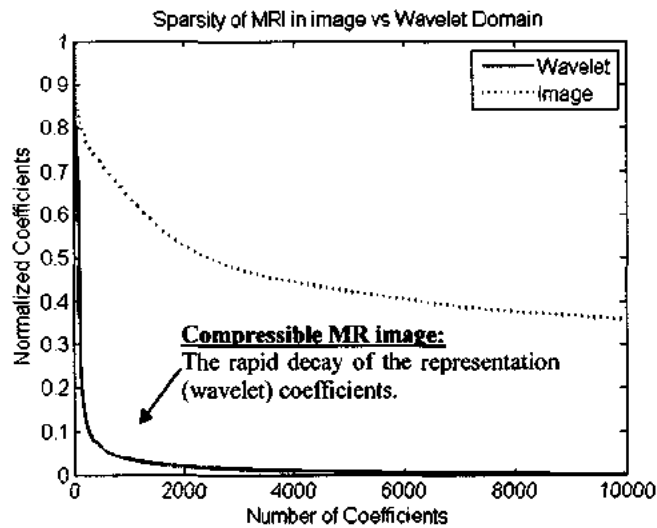


Figure-2.7: Sorted coefficients of MRI in pixel and wavelet domain. Only 1000 significant values are shown for comparison

The sparse approximation using transform coding may be either adaptive or non-adaptive. In the non-adaptive (linear) sparse approximation, only the desired number of transformed coefficients are retained at fixed location. However, in the adaptive (non-linear) approximation, the biggest number of transformed coefficients are kept and the rest are thrown away. For DCT, there is little difference between the two. However, nonlinear wavelet approximations adapt to the singularities and outperform the linear approximation [5].

2.2.1.3 Total Variation (TV)

TV is a commonly used to sparsely represent piece-wise smooth biomedical images. It measures the variations in the images and is computed by summing the norms of the discrete gradient [20]. Let $X \in \mathbb{C}^{n \times n}$ be a discrete space biomedical image with $x_{i,j}$ denoting the pixel value at i th row and j th column, then its TV is defined as:

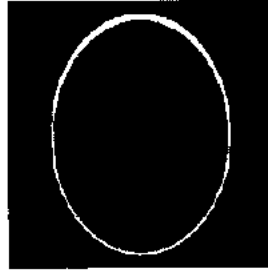
$$TV(X) = \sum_{i,j} \sqrt{|\nabla_{1(i,j)}X|^2 + |\nabla_{2(i,j)}X|^2} = \sum_{i,j} \|\nabla_{(i,j)}X\|_2 \quad (2.10)$$

where $\nabla_{1(i,j)}X \in \mathbb{C}^{n \times n}$ and $\nabla_{2(i,j)}X \in \mathbb{C}^{n \times n}$ are the horizontal and vertical difference on image X respectively i.e.

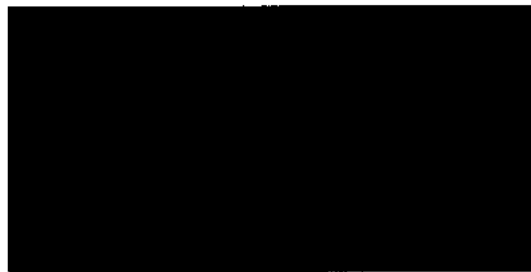
$$\nabla_{1(i,j)}X = \begin{cases} x_{i+1,j} - x_{i,j}, & i < n \\ 0, & i = n \end{cases}$$

$$\nabla_{2(i,j)}X = \begin{cases} x_{i,j+1} - x_{i,j}, & j < n \\ 0, & j = n \end{cases}$$

and $\nabla_{(i,j)}X = [\nabla_{1(i,j)}X \ \nabla_{2(i,j)}X]^T \in \mathbb{C}^{n \times n \times 2}$ is the discrete gradient of the image. A biomedical image is said to be k -sparse in the total-variation sense if $\|TV(X)\|_0 = k$. Fig-2.8 shows a 256×256 standard shepp-Logan phantom image that is used primarily in the biomedical image reconstruction such as computed tomography (CT). This image is not directly sparse but has gradient-based sparsity.



Shepp-Logan phantom image



Horizontal Difference Vertical Difference

Figure-2.8: Gradient based sparsity of Shepp-Logan image

Once a signal has sparse representation (direct or in a transformed domain), CS provides a framework for its recovery from sub-Nyquist incoherent measurements

2.2.2 Incoherent Sampling (measurements)

In the theory of CS, the sensing or sampling mechanism at the encoder can be represented as a linear transformation of a length n signal vector \mathbf{x} to a length m vector \mathbf{y} with $m \ll n$:

$$y_i = \sum_{j=1}^n \varphi_{ij} x_j = \langle \varphi_i, \mathbf{x} \rangle, \quad 1 \leq i \leq m \quad \text{or} \quad \mathbf{y} = \Phi \mathbf{x} \quad (2.11)$$

where the transformation matrix $\Phi: \mathbb{R}^n \rightarrow \mathbb{R}^m$ is known as the measurement or sensing matrix and is formed from the sampling/sensing waveforms (or test functions) $\varphi_1^T, \varphi_2^T \dots \varphi_m^T$ as rows. Thus, the measurement or observation vector \mathbf{y} is obtained from the non-adaptive linear projections (transformation) of the original signal \mathbf{x} .

As given in Eq-2.11, the generic notion of the sampling as inner product of the signal/image \mathbf{x} against the test functions (φ_i) allow us to successfully apply CS to biomedical images where the scanners naturally acquire the encoded samples instead of direct pixel values. The choice of φ_i varies from one imaging modality to another. For example, if the sensing waveforms (φ_i) are sinusoids at different frequencies, then Φ is essentially a Fourier matrix and the measurement vector contains Fourier coefficients as in the case of magnetic resonance imaging (MRI). Similarly, if the test functions are delta ridges then Φ is the discrete Radon transform and the measurements are line integrals as in the case of computed tomography (CT) [5].

For a square ($m = n$) and invertible matrix Φ , the transformation is reversible which means that the input signal can be exactly recovered from the output (*i. e.* $\hat{\mathbf{x}} = \Phi^{-1}\mathbf{y}$).

However, there are some practical situations where it is preferable to use a rectangular transformation matrix ($m \ll n$) having less number of rows than the columns. In context of linear algebra, this leads to an under-determined system of linear equations. In the framework of CS, this is equivalent to acquiring less number of measurements than the ambient dimensionality of the original signal while in the application of biomedical imaging e.g. MRI and CT, this directly corresponds to a reduction in the acquisition (scan) time and less exposure to the radiation dose respectively [7,21].

For the under-determined system, the matrix Φ has a null space which means that different vectors can result in the same measurements after the transformation. Thus, there are infinitely many solutions that make the recovery process ill-conditioned. In the MRI case, it means that the final linear reconstructed image from its partial Fourier data will have aliasing artifacts because of violation of the Nyquist criterion. Figure-2.9 depicts the issue of aliasing during the final reconstruction of the undersampled MR image by skipping every other line at the MR scanner (coherent sampling). The folding over of the image is clearly seen in the final reconstructed image that is obtained using a linear recovery technique by acquiring 50% equispaced samples of the original MRI data of Fig-2.5.

Thus, it is not possible to reduce the acquisition time of the biomedical images by simply reducing the data points collected by the scanners. However, the theory of CS suggests that if the images are sparse or compressible and the measurements are incoherent (i.e. the sensing matrix Φ satisfies certain properties), then the recovery from the partial data is possible using a non-linear reconstruction algorithm.

CS recovery works well when the representation and measurement basis pair (Ψ, Φ) are highly uncorrelated. In the context of CS, there are three domains and two different transformations associated with a biomedical image, as shown in Fig-2.10.

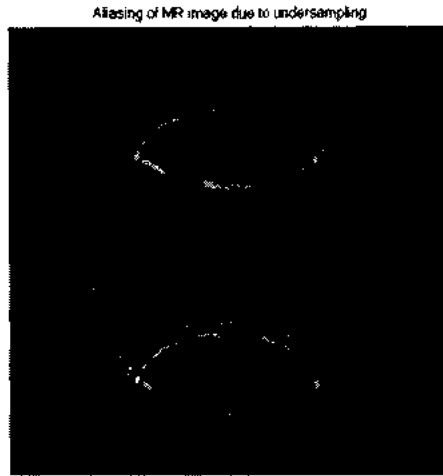


Figure-2.9: Aliasing due to linear reconstruction of MRI from its partial Fourier data

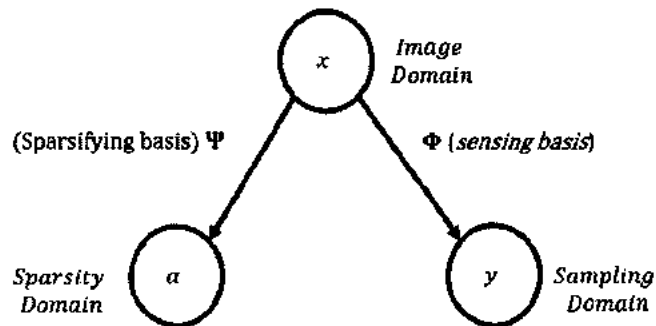


Figure-2.10: Different domains and transformations in CS

Assuming the measurement and sparsifying bases to be orthonormal, their mutual coherence is defined as the maximum value of the inner product between the vectors of the two bases [4]:

$$\mu(\Psi, \Phi) = (\sqrt{n} \max_{1 \leq i, j < n} |\langle \psi_i, \phi_j \rangle|) \in [1, \sqrt{n}]$$

here both $\Psi, \Phi \in \mathbb{C}^{n \times n}$ and \sqrt{n} is the normalization constant. As an example, the Fourier basis and canonical basis are maximally incoherent with $\mu = 1$. High value of coherence indicates that there are correlated vectors between the two bases which is

undesirable in CS. High value of incoherence leads to higher undersampling factors and specifies that a signal with sparse representation in a given sparsifying domain (Ψ) must be spread out in the domain where it is acquired. It means that the measurement basis vectors φ_j needs to be completely unstructured (noise-like) [5]. This is where the importance of random matrices comes into the theory of CS.

It has been shown that Gaussian random matrices can be used for the acquisition at CS encoder as they are largely incoherent with any choice of basis Ψ [3]. However, purely random matrices cannot be used for practical problems as they are computationally inefficient and need a large storage. Other preferable choices of sensing matrices are Bernoulli matrices with entries ± 1 , noiselets and random Fourier matrices.

The notion of coherence allows us to choose the domain where the image can be compressively sampled. In the example of MRI, MWI and parallel-beam CT, Φ is taken as the Fourier matrix and Ψ can be a DCT or DWT matrix.

When $\Phi \in \mathbb{C}^{m \times n}$ and $\Psi \in \mathbb{C}^{n \times n}$, the measurements as CS encoder can be treated as a dimensionality reduction problem. Using Eq-2.3 an Eq-2.11, the observation vector can be written as:

$$\mathbf{y} = \Phi \mathbf{x} = \Phi(\Psi \boldsymbol{\alpha}) = \mathbf{A} \boldsymbol{\alpha} \quad (2.12)$$

Here $\mathbf{A} = \Phi \Psi \in \mathbb{C}^{m \times n}$ is the new measurement matrix that maps the sparse representation of \mathbf{x} into the measurements. From Eq-2.12, it is clear that the problem of CS recovery is equivalent to the sparse representation problem. For Matrix \mathbf{A} to be good for CS, it has to satisfy the restricted Isometry Property (RIP) [22,23]. RIP is a necessary condition on matrix \mathbf{A} that guarantee a stable recovery for k -sparse or compressible signals. An $m \times n$ measurement matrix \mathbf{A} is said to satisfy the RIP of order k with isometry constant $\delta_k \in (0,1)$ if:

$$(1 - \delta_k)\|\alpha\|_2^2 \leq \|A\alpha\|_2^2 \leq (1 + \delta_k)\|\alpha\|_2^2 \quad (2.13)$$

for all k -sparse vector α (i.e. $\|\alpha\|_0 \leq k$).

For good measurements matrices the isometry constant δ_k is close to 0 which assures that k -sparse vectors cannot be in the null space of A . This is equivalent to saying that every subset of k columns taken from matrix A are nearly orthogonal. It is known that random Gaussian or Bernoulli matrices as well as matrix formed by randomly selecting columns from Fourier matrix have small isometry constants.

The philosophy of CS is based on the fact that the number of measurements required for the reconstruction of a signal is proportional to the compressed size of the signal, rather than its uncompressed size. The number of compressively sampled measurements (m) directly depends on the coherence of the sensing matrix ($A = \Phi\Psi$) and sparsity level (k) [1,4].

$$m \geq C \cdot \mu^2(\Phi, \Psi) \cdot k \cdot \log n$$

here $\mu(\Phi, \Psi)$ is the coherence and C is a positive constant. Empirical results show that a k -sparse signal can be recovered from $m \geq 4k$ incoherent measurements.

For biomedical images such as MRI and MWI the data is acquired by recording the Fourier coefficients and not the pixels, DCT or wavelet coefficients. At the encoder (scanner), the acquired measurements can be written in the form of $y = F_u x$ (i.e. $A=F_u$), where F_u is the partial Fourier matrix. So, if the random undersampling of frequency domain (Fourier) data results in incoherent artifacts in the sparsifying domain such as DCT or wavelet, then the final image can be reconstructed using a nonlinear recovery algorithm. In MRI, the incoherence between sparsity and sampling bases can be improved using variable density, spiral or radial sampling. For MWI, a nonuniform raster scan provides better incoherence with sparsifying basis [24]. However, it is

appropriate to consider the prior knowledge of the image class before designing a sampling pattern.

2.2.2 Non-Linear Recovery

Given the sensing matrix Φ (or A) and measurement vector \mathbf{y} , the aim of the CS reconstruction algorithm is to estimate the original signal \mathbf{x} (or α). From Eq-2.3, it clear that the CS recovery (finding α given A and \mathbf{y}) is a specific type of sparse approximation problem. Therefore, sparse representation algorithms plays a vital role in the recovery of compressively sampled biomedical images. Mathematically speaking, the CS recovery algorithm has to solve an underdetermined systems of linear equations where the number of equations (acquired data at the scanner) is less than the number of unknowns (pixel values of the biomedical image).

One possible approach is to find the minimum norm solution by solving the following least square minimization problem:

$$\hat{\alpha} = \underset{\alpha}{\operatorname{argmin}} \frac{1}{2} \|\mathbf{y} - A\alpha\|_2^2 \quad (2.14)$$

However, the final reconstructed image obtained from (2.14) is severely distorted even if the sampling is incoherent. An improved solution can be obtained by including a proper regularization term in the objective (cost) function. So, for the general inverse problem corresponding to Eq-2.12, the recovery algorithm can be formulated by the following Lagrangian form:

$$\hat{\alpha} = \underset{\alpha}{\operatorname{argmin}} \frac{1}{2} \|\mathbf{y} - A\alpha\|_2^2 + \beta \mathcal{R}(\alpha) \quad (2.15)$$

where $\beta \in \mathbb{R}^+$ is the Lagrange multiplier that adjusts a trade-off between the representation error (data fidelity) and the regularizer term $\mathcal{R}(\alpha)$. The function $\mathcal{R}(\alpha)$

operates element-wise on vector α . It is selected to promote sparsity and usually takes the form [3-5]

$$\mathcal{R}(\alpha) = \|\Psi x\|_p^p = \|\alpha\|_p^p = \sum_{i=1}^n |\alpha(i)|^p \quad (2.16)$$

Fig-2.11 shows the scalar function $|\alpha|^p$ that is used in the computation of norm. It is clear that as p approaches zero, the curve becomes an indicator function of the l_0 -norm. For $p = 2$, the problem presented in Eq-2.15 reduces to the classical Tikhonov regularization with a proper closed form solution. But again, this will not work for the CS recovery as it uses l_2 -norm which does not promote sparsity. Ideally, the l_0 -norm ($p = 0$) of an image provide the exact measure of its sparsity. However, its practical implementation is limited as the problem becomes computationally intractable (NP-hard). Surprisingly, it has been shown that in many situations of practical interest, the l_1 -norm (corresponding to $p = 1$) can be used in place of the l_0 -norm to recover the compressively sampled biomedical images [1-4].

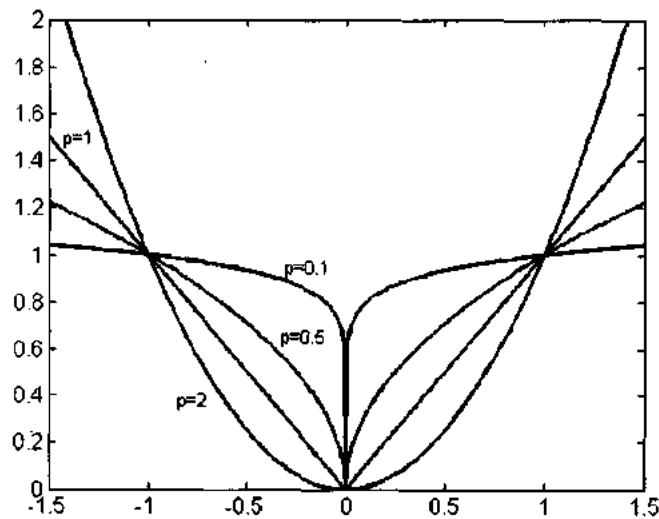


Figure-2.11: Behavior of scalar function $|\alpha|^p$

To conclude, the encoder part of CS is relatively simple and consists of the non-adaptive linear measurements. However, the CS decoder is very challenging because of the computation cost in the image reconstruction process. Devising an efficient and lower cost CS recovery technique for high dimensional biomedical images is still considered as one of the fundamental challenging task which is one of the main goals of this dissertation.

2.3 Related Work

Before the development of modern CS theory, some of the key ideas of CS were applied to biomedical imaging. In the earlier work, reweighted least-squares and its variants were used for sparsity based imaging methods to solve the associated nonlinear reconstruction problems [25]. The method of combining random sampling with nonlinear recovery algorithm for the recovery of MRI and tomography was presented in [26]

The introduction of CS theory immediately found important applications in the diverse medical imaging modalities. Its first potential application was MRI because of the slow acquisition and its pressing need to reduce the sampling rate. The subsequent work includes brain [7], coronary [27], dynamic and cardiac [28, 29], pediatric [30] and parallel MR imaging [31]. CS has also been successfully applied to optical imaging modalities including diffusion optical tomography [32] and opto-acoustics tomography [33]. Because of its ability to shorten the scan time and consequently reduce the radiation dose, CS has seen fast growth in CT over the last decade [34-35]. The application of CS to imaging modalities like Positron Emission Tomography (PET) or Single Photon Emission Computed Tomography (SPECT) is relatively few because

these modalities are mainly photon-limited instead of sampling-limited [36,37]. In a relatively recent work, several encouraging results have been reported by using CS for 2D and 3D ultrasound images [38]. CS applications to microwave imaging is relatively new. In [24], CS is demonstrated to improve the efficiency of microwave imaging. The new and cutting-edged applications includes motion corrected CS [39], matrix completion [40], tensor completion [41] and dictionary learning for biomedical imaging [10, 42].

Because of the transformative potential for preclinical and clinical applications, algorithm development and system designs, the applications of compressed sensing to biomedical imaging are enormous. Almost all of these applications strongly rely on a non-linear recovery algorithm for the image recovery from the undersampled data which is a challenging and fascinating task. While CS has reduced the acquisition time and the amount of raw data, unfortunately the computation time of the image recovery has increased. In the initial work of CS, convex optimization was used to solve the recovery problem by developing algorithms for the following constrained formulation [12]:

$$\hat{\alpha} = \arg \min_{\alpha} \|\alpha\|_1 \text{ subject to } y = A\alpha \quad (2.17)$$

which is known formally as a Basis Pursuit (BP). BP is a natural convex relaxation of the sparse decomposition problem and is computationally tractable. Other major classes of CS reconstruction algorithms include greedy pursuit, non-convex optimization and Bayesian framework [43]. Greedy algorithms such as Orthogonal Matching Pursuit (OMP) [44], Stagewise OMP [45] and Compressively Sampled Matching Pursuit (CoSaMP) [46] operate by iteratively selecting the columns of the dictionary while keeping track of the current approximation and the residual. At each iteration, it chooses

TF-14593

the column that is most closely correlated with the residual and possibly involves least square projections which makes the iterations computationally expensive.

Other popular recovery methods include Bregman iterations [47], Gradient Projection for Sparse Reconstruction (GPSR) [48] and sparse reconstruction by Separable Approximation (SpaRSA) [49]. A comparison of three CS reconstruction algorithms (SPGL1, NESTA and RecPF) for biomedical imaging can be found in [50]. Most of the CS reconstruction algorithms are general purpose and require too many iterations making the recovery inefficient, specifically if the images have large dimensions as in the case of biomedical applications [11,51].

Contrary to the previous algorithms that mostly involve expensive operations e.g. solving least square and matrix factorization, Iterative Shrinkage-Thresholding (IST) algorithms utilize only simple operations such as matrix-vector multiplications. Shrinkage is an appealing sparsity inducing method and is known to be best suited for the denoising of Gaussian noise [51,52]. The popular types of IST are Iterative Hard Thresholding (IHT) [53,54], fast iterative shrinkage thresholding algorithm (FISTA) [55], separable surrogate functional (SSF) and parallel coordinate descent (PCD) [56]. IST algorithms minimize the following Lagrangian formulation to get the sparse signal approximation [57]:

$$\hat{\alpha} = \underset{\alpha \in \mathbb{C}^n}{\operatorname{argmin}} \frac{1}{2} \|\mathbf{y} - \mathbf{A}\alpha\|_2^2 + \beta \|\alpha\|_1 \quad (2.18)$$

where $\beta \geq 0$ is the regularization parameter. For the orthonormal basis ($\mathbf{A} = \Psi$), it has been shown that a closed form solution to the optimization problem of (2.18) is given by [55-57]:

$$\hat{\alpha}_i = T_\beta(\alpha_i) = \begin{cases} \alpha_i - \beta, & \alpha_i > \beta \\ \alpha_i + \beta, & \alpha_i < -\beta \\ 0, & \text{Otherwise} \end{cases} \quad (2.19)$$

Where $\alpha = \Psi x = \{\alpha_i\}_{i=1}^n$ are the transformed coefficients and $T_\beta(\cdot)$ is the element-wise thresholding (shrinkage) operator.

Because of the computational simplicity, near-optimal error guarantee and robustness, the suite of algorithms presented in this dissertation are mainly based on IST methods such as SSF, PCD etc. These methods are applied to solve the following optimization problem for the Fourier encoded image such as MRI, parallel-beam CT and MWI.

$$\hat{x} = \underset{x}{\operatorname{argmin}} \left(\frac{1}{2} \|y - F_u x\|_2^2 + \beta \|\Psi x\|_1 \right) \quad (2.20)$$

2.4 Quality assessment parameters

To assess the quality of the final reconstructed image, standard performance metrics such as correlation, fitness value, peak signal-to-noise ratio (PSNR), structural similarity index (SSIM) [58], improved-signal-to-noise ratio (ISNR) and artifact power (AP) are used.

PSNR is one of the widely used quality assessment measure and is considered to be an approximation to human perception of reconstruction quality. For a (256×256) biomedical image, the standard definition of PSNR is [5]:

$$PSNR = 20 \cdot \log_{10} \left\{ \frac{255 \cdot 256}{\|\hat{x} - x\|_2^2} \right\} [dB] \quad (2.21)$$

ISNR is another commonly used metric for quantitative evolution of reconstruction results and is defined as:

$$ISNR = 10 \cdot \log_{10} \left\{ \frac{\|x - |F_u x|\|_2^2}{\|\hat{x} - x\|_2^2} \right\} [dB] \quad (2.22)$$

The higher the value of ISNR, the better the quality of reconstructed image.

AP has been derived from “square difference error” and is calculated as:

$$AP = \frac{(\sum_i |x(i) - \hat{x}(i)|^2)}{\sum_i |x(i)|^2} \quad (2.23)$$

Reconstructed image with a smaller value of AP indicates a better quality.

The computation of SSIM between two images (x and \hat{x}) is based on the luminance, contrast and structure of the images. It is computed on various windows of the reconstructed image using the relation:

$$SSIM(x, \hat{x}) = \frac{(2\mu_x\mu_{\hat{x}} + C_1)(2\sigma_{x\hat{x}} + C_2)}{(\mu_x^2 + \mu_{\hat{x}}^2 + C_1)(\sigma_x^2 + \sigma_{\hat{x}}^2 + C_2)} \quad (2.24)$$

where C_1 and C_2 are constants that depends on the dynamic range of the images. μ_x and $\mu_{\hat{x}}$ represent the mean values while σ_x^2 and $\sigma_{\hat{x}}^2$ denote the variances of the original and estimated image respectively. $\sigma_{x\hat{x}}$ is the covariance between of original and recovered image. SSIM is a scalar value in the interval $[-1, 1]$. The maximum value 1 is achieved when both images are exactly identical.

2.5 Summary

This chapter presented an overview of the sparse representation and compressed sensing with focus on biomedical imaging. The commonly used analytical sparsifying transforms were reviewed as well. Finally, quality assessment metrics were also discussed after briefly reviewing the applications of compressed sensing to various biomedical imaging modalities.

CHAPTER-3

BIOMEDICAL IMAGING MODALITIES AND PROJECTION ONTO CONVEX SETS BASED CS RECOVERY

This chapter presents the physical principles and mathematical descriptions related to the data acquisition of three biomedical imaging modalities, namely parallel-beam CT, MRI and MWI. The underlying physics for each of these imaging techniques is different but they share some common properties. For example, their scanners record the encoded (Fourier) measurements and the acquisition process can be represented by a linear model of the form $\mathbf{y} = \Phi\mathbf{x}$, making them a potential application of CS. It has been shown that iterative POCS algorithm can be used to recover these images from less number of Fourier data.

3.1 Magnetic Resonance Imaging (MRI)

MRI scanners use magnetic field and radio frequencies rather than ionizing radiations such as x-rays used in CT. Majority of the clinical MRI machines use a superconducting magnet having magnetic flux density, B_0 , of 1.5 or 3 Tesla (T). This field is about 50,000 times the earth magnetic field (0.00003 T).

The human body is composed of 70% water (H_2O) which comprises of hydrogen and oxygen atoms. MRI uses the magnetic properties of hydrogen atom to produce images. The hydrogen atom has only one proton that yields a magnetic field (called magnetic moment) due to its spinning. In the absence of an external magnetic field, the net magnetic moment is zero because of the random orientation of the protons. However, in the presence of an external magnetic field (B_0), a greater proportion of the protons

(hydrogen nuclei) align themselves parallel (low energy state) than antiparallel (high energy state) to the direction of the applied field. This gives rise to a net magnetic moment, M_0 , in the direction of B_0 and is called longitudinal magnetization. The proton spins around the long axis of the applied magnetic field at a frequency known as Larmor frequency which is about 63.9 MHz for 1.5 T clinical scanner.

MRI scanners use three gradient coils, one in each of the cardinal directions to alter the longitudinal magnetic field. It gives MRI the capacity to image directionally along the x , y and z -axis. Gradient coils help to excite only a slice of interest in the imaging volume by varying the precession in the object. The x , y and z -gradients (G_x , G_y , G_z) run along the horizontal, vertical and long axes to produce sagittal, coronal and axial images respectively.

MRI scanners also use radio frequency (RF) coils that come with different designs for each body part to produce best possible diagnostic images. The RF coils are used to transmit a second magnetic field, B_1 , or RF pulse (at Larmor frequency) which results in the disturbance of the proton alignment. This causes some low energy parallel protons to flip to a high energy state decreasing the longitudinal magnetization and producing a magnetization component M_{xy} that is transverse to M_0 . The flip angle (α) depends on the duration of the pulse and the strength of the magnetic field (B_1) which is usually a few μT .

When the RF pulse is removed, the transverse magnetization M_{xy} experiences an exponential decay with a time constant T_2 while the longitudinal component M_z recovers exponentially with a time constant T_1 . The T_1 and T_2 relaxation times will vary depending on the tissue composition and structure. The changing magnetic moment of the net magnetic vector (sum of longitudinal and transverse magnetization) results in

free induction decay (FID) that induces a changing voltage in the receiver coil and is used for imaging in MRI.

As shown in Figure 3.1, three types of spatial encoding are generally used for MRI. These are called slice selection, phase encoding and frequency encoding [59].

Magnetic resonance occurs at a particular slice (subvolume) where the transmitted RF pulse has a frequency close to the Larmor frequency at that slice. Other slices cannot absorb this RF energy because of different precession frequencies due to gradient fields. The frequency of the RF pulse is determined by the magnitude of the slice selection gradients and the slice position (B_0, G_z, z). The thickness of the slice is controlled by the range of frequencies (bandwidth) of the applied RF pulse. After the slice selection, the scanner measures the transverse magnetization with two dimensional distribution by applying additional gradients that cause spins at different spatial locations to precess at different rate, so that their individual contributions can be measured.

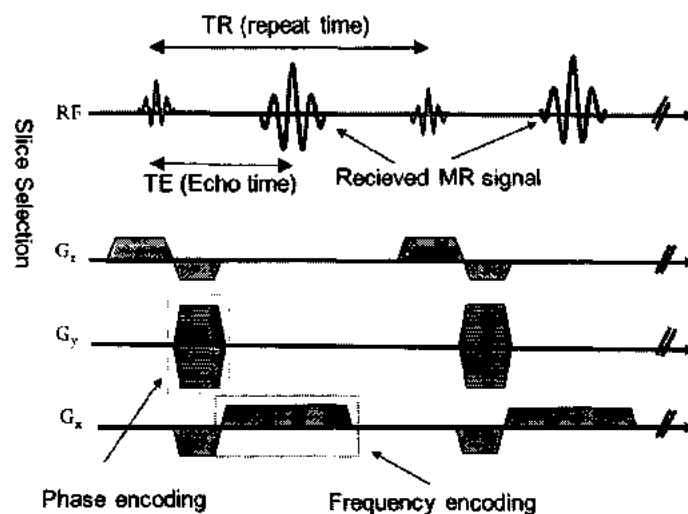


Figure-3.1 Pulse sequence diagram representing various gradients for spatial encoding

By applying a constant gradient G_y (in the y direction) to the selected slice, the precession frequency will change linearly in this direction. The phase encode gradient is turned on for a brief period of time. When the gradient is turned off, the Larmor frequency returns to a constant value. The signal at different positions will accumulate a different phase along the y axis. This process of locating MR signal by changing the phase of spins is called phase encoding. Spatial resolution directly depends on the number of phase encoding levels used.

Similarly, by applying a constant gradient G_x (in the x direction), the Larmor frequency will vary linearly in that direction. With gradient on, the recorded signal will exhibit different frequencies along the x axis. This process is known as frequency encoding and the corresponding gradient is known as read out gradient.

Final MR image is obtained after collecting a series of frames of data involving many RF excitations and the application of gradient fields in an orderly manner that generates a map with unique phase-frequency pair at each point in the two spatial dimensions. During each readout, the samples are stored in a raw matrix known as k -space. To fill a single line in the k -space, the RF pulse is applied which is followed by phase and frequency encodings. This process is repeated after every TR (repetition time) seconds till the entire k -space is filled. It is worth mentioning that the acquisition time of MRI heavily depends on the number of phase encoding steps as the frequency encoding process is fast and the samples along the frequency encoding dimension are acquired instantaneously.

For the conventional MRI using spatial encoding, the complex data collected by the receiver coils at the scanner takes the form of a volume integral [7, 60]:

$$y(\mathbf{k}) = \int_{\text{slice}} x(\mathbf{r}) e^{-j\mathbf{k}\mathbf{r}} d\mathbf{r} = \langle \varphi_{\mathbf{k}}(\mathbf{r}), x(\mathbf{r}) \rangle \quad (3.1)$$

The vector k , which is the integral of the gradients, is interpreted as the vector of spatial frequency coordinates and $\varphi_k(\mathbf{r}) = e^{-jk\mathbf{r}}$ are the Fourier Basis. $x(\mathbf{r})$ represents the spatial domain image. So the conventional MR gives a Fourier encoded image.

As the data is recorded digitally, so all the measurements are taken at discrete space \mathbf{r}_n .

Thus, the discrete version of Eq-2.1 is [7-8]:

$$\mathbf{y} = \begin{bmatrix} y_1 \\ y_2 \\ \vdots \\ y_m \end{bmatrix} = \begin{bmatrix} \langle \varphi_1(\mathbf{r}_n), x(\mathbf{r}_n) \rangle \\ \langle \varphi_2(\mathbf{r}_n), x(\mathbf{r}_n) \rangle \\ \vdots \\ \langle \varphi_m(\mathbf{r}_n), x(\mathbf{r}_n) \rangle \end{bmatrix} \text{ or } \mathbf{y} = \Phi \mathbf{x} \quad (3.2)$$

Where the matrix $\Phi = F$ is the Fourier matrix. So the k -space is the 'raw data space' with Fourier coefficients of the desired MR image. The original MR image is reconstructed by taking the inverse Fourier transform (IFFT) of the acquired k -space data i.e. $\mathbf{x} = \Phi^{-1}\mathbf{y} = F^{-1}\mathbf{y}$.

Fig-3.2 shows the k -space and the original MR image that is extensively used in our MRI related experiments. It was acquired at St. Mary's Hospital London using 1.5 Tesla GE HDxt scanner with an eight-channel head coil and a gradient echo sequence with the following specifications: TR/TE=55/10 msec, FOV =20 cm, bandwidth=31.25 KHz, slice thickness= 3 mm, flip angle= 90°, matrix size=256×256.

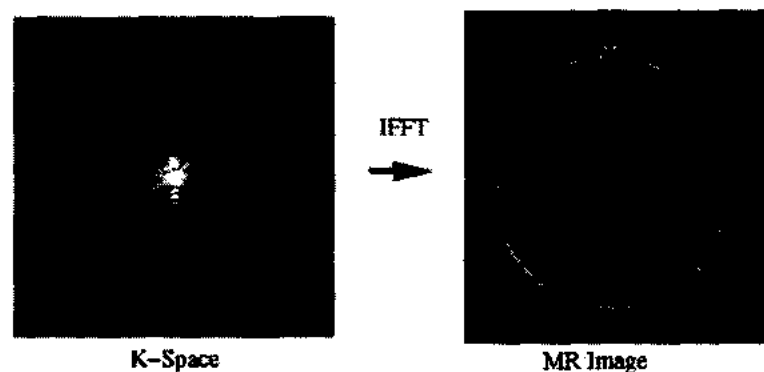


Figure-3.2: Fourier encoded MR image

Reducing the scan time of MRI by simply undersampling the k -space (as is done in CS), results in a smaller field of view (FOV). FOV of the MR image is defined by the gap between the phase encode lines. If the distance (Δk_y) between phase encode lines is doubled by uniformly undersampling the k -space, FOV will reduce to half of the original and aliasing will occur [61]. This effect is shown in Fig-3.3.

Instead of uniform undersampling, CS uses other undersampling patterns such as radial and variable density which take more samples at the center of the k -space than its outer periphery [47, 62]. It is due to the fact that most of the energy of MRI is concentrated at the center of the k -space. High frequency information about the image such as edges, contours etc. are preserved at the outer edges of the k -space. Fig-3.4 shows the relationship between the image space and k -space. To show how different parts of k -space contribute in the MR image formation, two different MR images are reconstructed by sampling the center and outer periphery of the k -space. This information is quite useful in designing an undersampling pattern for CS acquisition.

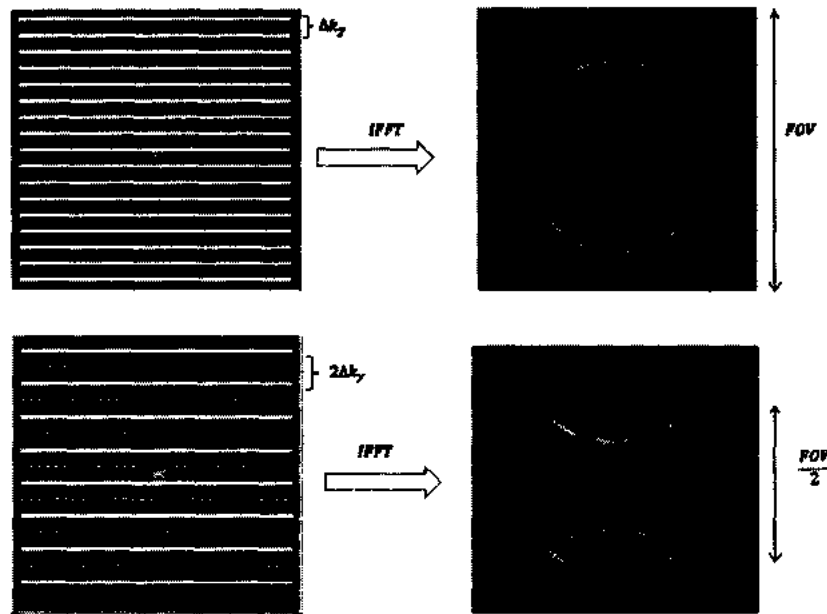


Figure-3.3: Aliasing due to the uniform undersampling of k -space

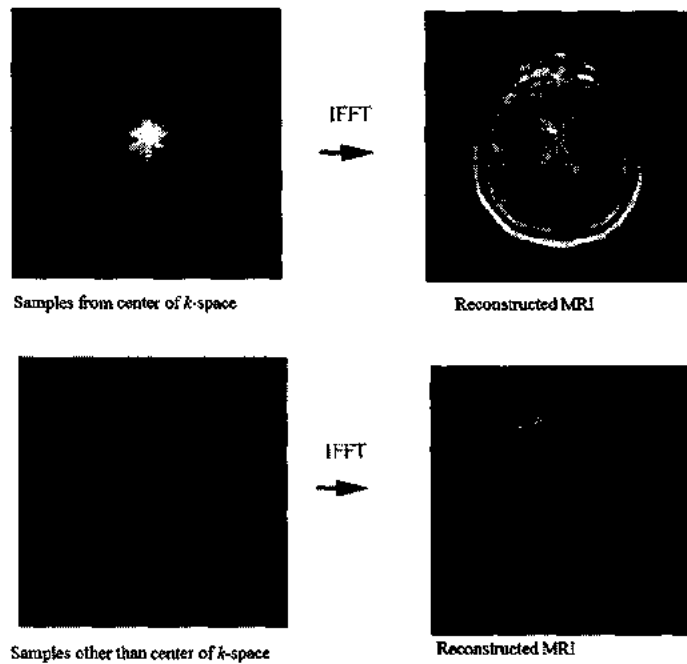


Figure-3.4: Effect of undersampling the k -space on reconstructed image

3.2 Parallel beam CT

Unlike MRI which uses magnetic field and RF pulses, CT involves shooting x-rays through the human body. CT imaging measures the attenuation coefficients $f(x, y)$ of the object being imaged. The scanner acquires the projection data $p_\theta(r)$ by recording the intensities of x-ray radiations after it has passed through the object at different angles. As shown in Fig-3.5, parallel beam CT uses parallel beams of radiation with angle θ to form projections. For a single measurement, the x-ray beam travels along a projection line $r = x \cos(\theta) + y \sin(\theta)$ defined by the space parameters (r, θ) . The final image is reconstructed using the Fourier transforms of these projection functions (measurements) at various angles.

Mathematically, the projection and attenuation functions are related by a line integral [63]:

$$p_{\theta}(r) = \int_{L_{\theta,r}} f(x,y) dl \quad (3.3)$$

where $L_{\theta,r}$ represents a line passing through the point $(x \cos(\theta), y \sin(\theta))$ and parallel to the t -axis. Eq-3.3 is often known as the Radon transform. So in CT, the Radom transform is computed physically by the attenuation of the x-rays as they pass through the tissues.

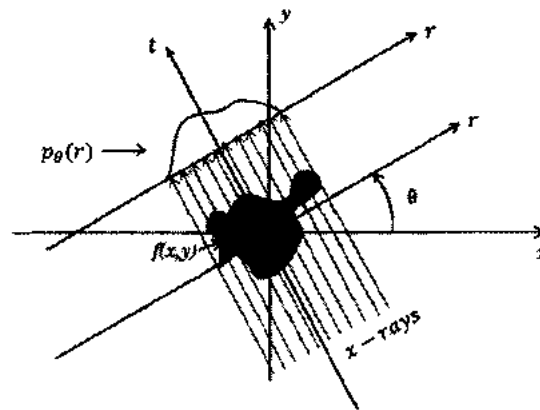


Figure-3.5: Projections in parallel beam CT

Using change of variables, $x = -t \sin \theta + r \cos \theta$ and $y = t \cos \theta + r \sin \theta$, the line integral of Eq-3.3 can be parametrized in the form [63,64]:

$$p_{\theta}(r) = \int_{-\infty}^{\infty} \int_{-\infty}^{\infty} f(x,y) \delta(x \cos \theta + y \sin \theta - r) dx dy \quad (3.4)$$

Here $\delta(\cdot)$ is the Dirac delta or continuous-time impulse. In modern CT, the x-ray beam is directed and the detector sweeps around the patient to collect thousands of projections at various angles. To discretize the collected data, a square grid is superimposed on the image with the assumption that the value of attenuation coefficient is small within each

cell of the grid. Thus, for a given set of discrete measurements p_i ($i = 1, 2 \dots m$) corresponding to line integrals at different angles θ_i and offsets r_i , the discrete version of Eq-3.4 becomes [65]:

$$p_i = \int_{-\infty}^{\infty} \int_{-\infty}^{\infty} f(x, y) \delta(x \cos \theta_i + y \sin \theta_i - r_i) dx dy = \langle f, \varphi_i \rangle \quad (3.5)$$

$$\mathbf{p} = \begin{bmatrix} p_1 \\ p_2 \\ \vdots \\ p_m \end{bmatrix} = \begin{bmatrix} \langle f, \varphi_1 \rangle \\ \langle f, \varphi_2 \rangle \\ \vdots \\ \langle f, \varphi_m \rangle \end{bmatrix} \text{ or } \mathbf{p} = \Phi \mathbf{f} \quad (3.6)$$

This equation is similar to Eq-3.2 ($\mathbf{y} = \Phi \mathbf{x}$) of MRI. However, for CT Φ is constructed from delta ridges by observing line integrals.

The parallel beam CT image can be recovered by using the Fourier slice theorem which relates the Fourier transform of a projection to the Fourier transform of the object along a radial line. It states that the one-dimensional Fourier transform of a parallel projection of an image $f(x, y)$ taken at angle θ gives the value of the two-dimensional Fourier transform $F(\omega_x, \omega_y)$ along one line subtending an angle θ with the ω_x -axis. Therefore, if the two-dimensional Fourier transform of the cross-sectional image $f(x, y)$ are restricted to the radial lines (as shown in Fig-3.6), the original image can be estimated by the inverse Fourier transform. It means that parallel beam CT can be modeled as a Fourier encoded imaging modality where the measurement matrix Φ is a radially sampled Fourier matrix.

3.2 Microwave Imaging (MWI)

MWI not only finds applications in the medical imaging, but it has widely been used for non-destructive testing as well. It is considered to be a preferred imaging technique

for early breast cancer detection as compared to X-rays and MRI because of its low cost, safety and high contrast [66].

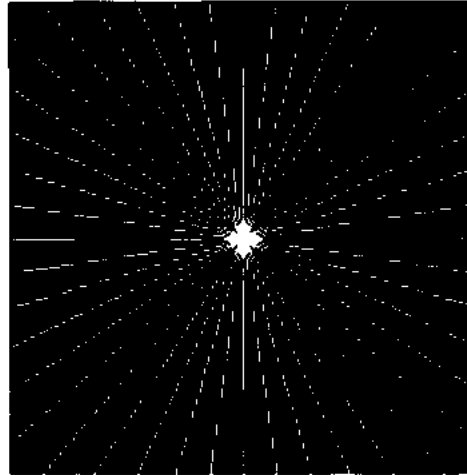


Figure-3.6: Radial lines used to sample the Fourier transform of an object for CT imaging

MWI is transmission-reflection imaging modality that uses a scanning system with a single antenna probe. In its simplest form, the scanner starts measurements on the sample under test (SUT) and utilizes raster scanning with uniform stepsize. The antenna collects data (reflection coefficients) as it moves from one position to another. Tissues with anomaly have different electrical and magnetic properties that result in a different reflection coefficient which is translated into a contrast during the final image formation. For high resolution image, the stepsize is very small resulting in a longer acquisition time. The theory of CS can, therefore, be used to randomly sample the SUT and reduce the acquisition time.

Fig-3.7 shows the measurement arrangement for MWI. The transceiver (antenna probe) is shown to be located at position (x', y', z_0) and a general point on SUT is selected at location $(x, y, 0)$. Let $f(x, y)$ represent the reflectivity function of the SUT, which is

defined to be the ratio of the reflected to incident field. The backscattered microwave reflection coefficients $s(x', y')$ is essentially the superposition of reflections from all points on the illuminated area of SUT multiplied with the roundtrip phase [67,68]:

$$s(x', y') = \iint f(x, y) e^{-j2kR} dx dy \quad (3.7)$$

Where $R = \sqrt{(x - x')^2 + (y - y')^2 + z_0^2}$ is the distance between transceiver and target point on SUT and $k = \omega/c$ is the wavenumber (c represents speed of light and ω is the angular frequency).

As in the case of CT and MRI, the data is acquired in discrete form. So if m discrete measurements are acquired, then Eq-3.7 takes the form:

$$s = \begin{bmatrix} s_1 \\ s_2 \\ \vdots \\ s_m \end{bmatrix} = \begin{bmatrix} \langle f, \varphi_1 \rangle \\ \langle f, \varphi_2 \rangle \\ \vdots \\ \langle f, \varphi_m \rangle \end{bmatrix} \text{ or } s = \Phi f \text{ with } \varphi_i = e^{-j2kR_i} \text{ (} 1 \leq i \leq m \text{)} \quad (3.8)$$

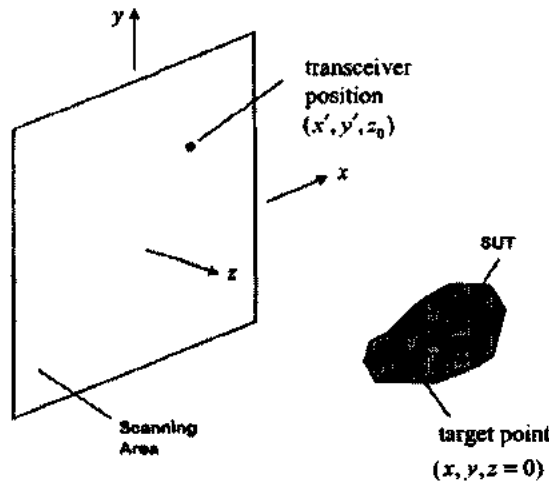


Figure-3.7: Measurement configuration for MWI

Fourier transform plays an important role in the MWI reconstruction. It has been shown that Eq-3.8 can be solved for $f(x, y)$ using the relation [67,69]:

$$f(x, y) = F_{2D}^{-1}\{F_{2D}\{s(x, y)\}e^{-jk_z z_0}\} \quad (3.9)$$

where $F_{2D} = F(\omega_x, \omega_y)$ is the 2-D Fourier transform and $k_z = \sqrt{4k^2 - k_x^2 - k_y^2}z_0$ (where k_x and k_y are the spatial wavenumbers).

Eq-3.9 shows that MWI shares one important property with MRI and CT. It can also be modeled to obtain the image from the Fourier measurements.

3.3 POCS based Recovery of Fourier encoded images

Based on the idea of projection onto convex sets [15,70,71], a computationally low cost algorithm can be obtained to recover Fourier encoded images from partial set of measurements. The algorithm can be derived by considering solution to the scalar version of the minimization problem presented in Eq-2.18. i.e.

$$T_\beta(z) = \underset{x}{\operatorname{argmin}} \left(\frac{1}{2}(z-x)^2 + \beta|x| \right)$$

$$\frac{1}{2}(z-x)^2 + \beta|x| = \begin{cases} \frac{1}{2}(z-x)^2 - \beta x, & x < 0 \\ \frac{1}{2}(z)^2, & x = 0 \\ \frac{1}{2}(z-x)^2 + \beta x, & x > 0 \end{cases} \quad (3.10)$$

Where $z, x \in \mathbb{R}$ and $T_\beta(z)$ is the scalar-valued shrinkage function. Its value depends on the minimizing variable x and z . As $|x|$ is not differentiable at $x = 0$, each term of (3.10) is differentiated separately and solved for x . This yields the desired shrinkage function that is given by [55,72]:

$$T_\beta(z) = \max(|z| - \beta, 0) \operatorname{sig}(z)$$

$$= \begin{cases} z + \beta, & z < -\beta \\ z - \beta, & z > \beta \\ 0, & \text{otherwise} \end{cases} \quad (3.11)$$

The parameter β is recognized as the thresholding parameter. The shrinkage function $T_\beta(z)$ maps the input value z to a desired output value. It induces sparsity by setting smaller values of z ($|z| < \beta$) to zero and shrinking the larger values ($|z| \geq \beta$) towards zero.

With the assumption that the elements x_i of vector \mathbf{x} are independent, each term of the objective function of the form $f(x) = \frac{1}{2}\|y - x\|_2^2 + \beta\|x\|_1$ can be minimized separately by solving $\operatorname{argmin} \frac{1}{2}(y_i - x_i)^2 + \beta|x_i|$ which has a closed form solution $\hat{x}_i = T_\beta(y_i)$ [73].

Fig-3.8 shows how the computationally low-cost POCS based algorithm can be used to recover the Fourier encoded image iteratively by solving (2.20).

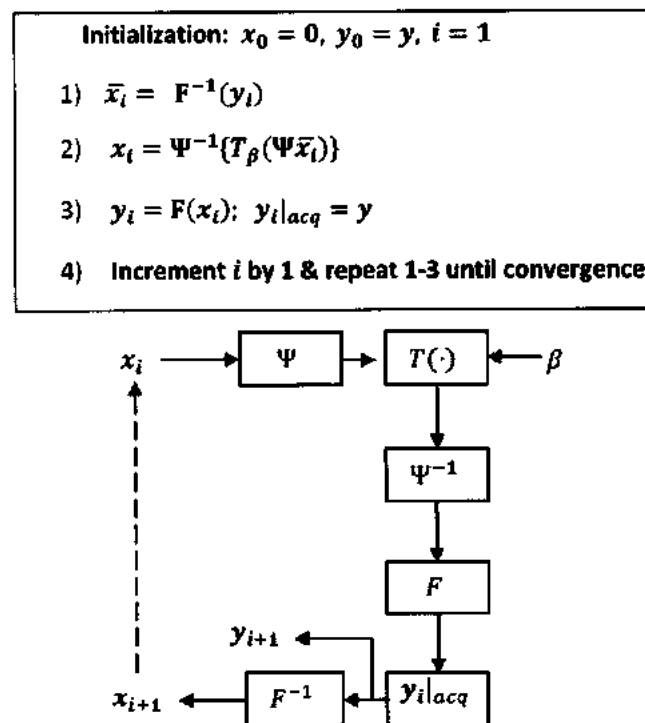


Figure-3.8: POCS algorithm (with block diagram) for Fourier-encoded image recovery

The algorithm moves back and forth between two main steps to estimate the missing samples. It uses data consistency and soft-thresholding in the Fourier and sparsifying domains respectively.

Fig-3.9 shows the experimental results of POCS based recovery when the original MR image of Fig-2.5 is compressively undersampled in the k -space. Partial Fourier samples are collected using variable density sampling pattern. The original image is recovered using linear reconstruction and POCS based recovery technique. Linear recovery is done by taking inverse FFT of the undersampled image by replacing the missing sampling data with zeros. The resulting image is severely distorted. However, the POCS based algorithm produces a reasonably accurate image. It uses soft-thresholding in the wavelet domain with $\beta=0.019$. During each iteration, the missing samples are estimated while the already acquired data remain unchanged.

The quality of the final reconstructed image vary with the selection of the thresholding parameter β . Its actual value mainly depends on the undersampling pattern and the sparsifying transform used. For improved reconstruction quality, proper selection of the thresholding parameter is important. Fig-3.10 shows the decrease in mean-square-error (MSE) between the original and the final reconstructed image for various values of β . Similarly, Table-3.1 lists the final values of the MSE and correlations attained by the final reconstructed MR image. These values are recorded by fixing different values of the parameter β and running the POCS algorithm for 10 iterations.

The algorithm of Fig-3.8 treats the CS recovery as a denoising problem. The effect of undersampling in the Fourier domain is equivalent to adding (Gaussian-like) noise in the image domain. So, the POCS based algorithm essentially estimates the original image from its noisy (undersampled) version. The transformed domain coefficients of

the image having values less than the thresholding parameter β are treated as noise and are discarded during the shrinkage operation. However, values sparse coefficients above the threshold are linearly adjusted to recover the original image.

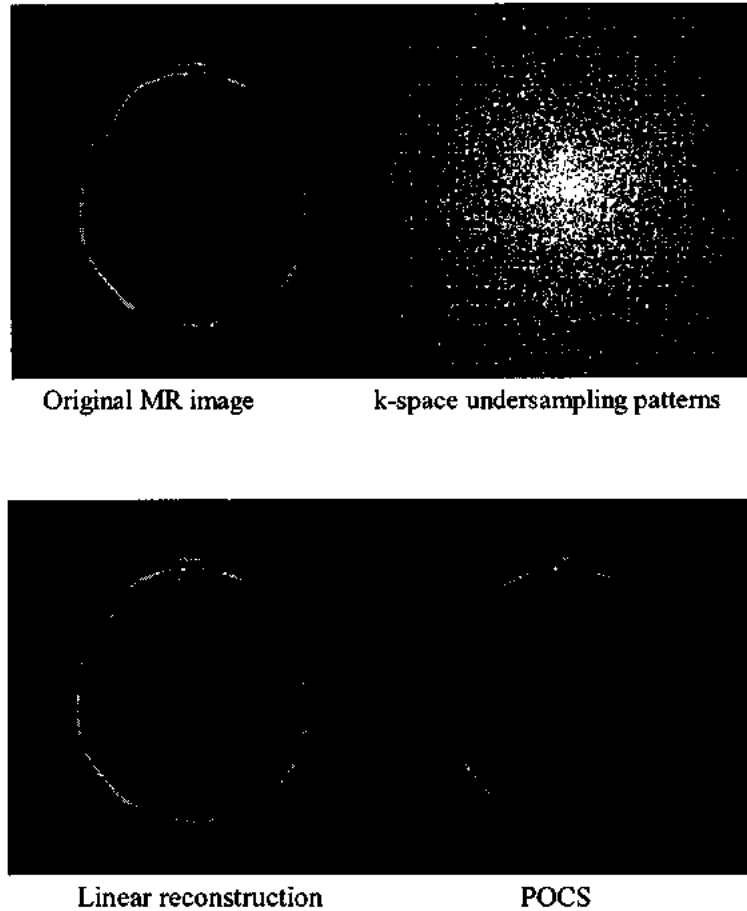


Figure-3.9: Recover of compressively sampled MRI using POCS

To further demonstrate the effectiveness of the POCS based recovery scheme, the algorithm is applied to reconstruct a microwave image as shown in Fig-3.11. This image was obtained using random raster scanning. The undersampling pattern used in the experiment is also shown in Fig-3.11. In this case, the recovery uses DCT as a

sparsifying transform and therefore the nonlinear shrinkage is applied to the DCT coefficients. The algorithm runs for 10 iterations to generate the final image which is shown in Fig-3.12. It can be seen that the simple POCS algorithm can produce reasonably good image from the undersampled Fourier data.

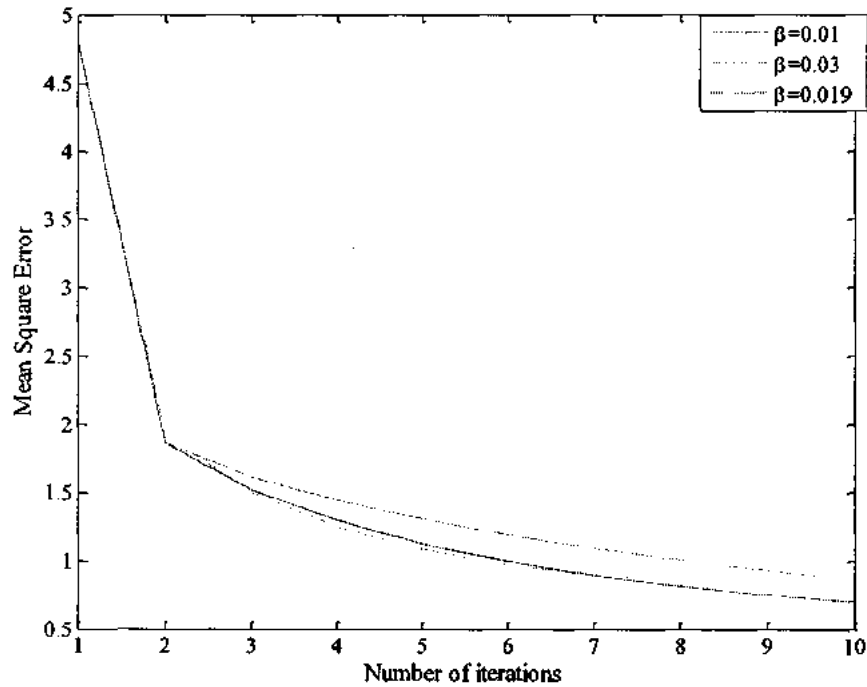


Figure-3.10: Effect of thresholding parameter on the quality (MSE) of reconstructed MR image.

Value of β	0.0100	0.0122	0.0144	0.0189	0.0233	0.0256	0.03
MSE	0.8079	0.7340	0.6903	0.6778	0.6970	0.7224	0.7522
Correlation	0.9966	0.9967	0.9968	0.9969	0.9964	0.9963	0.9959

Table-3.1 Values of MSE and correlations attained by the final MR image

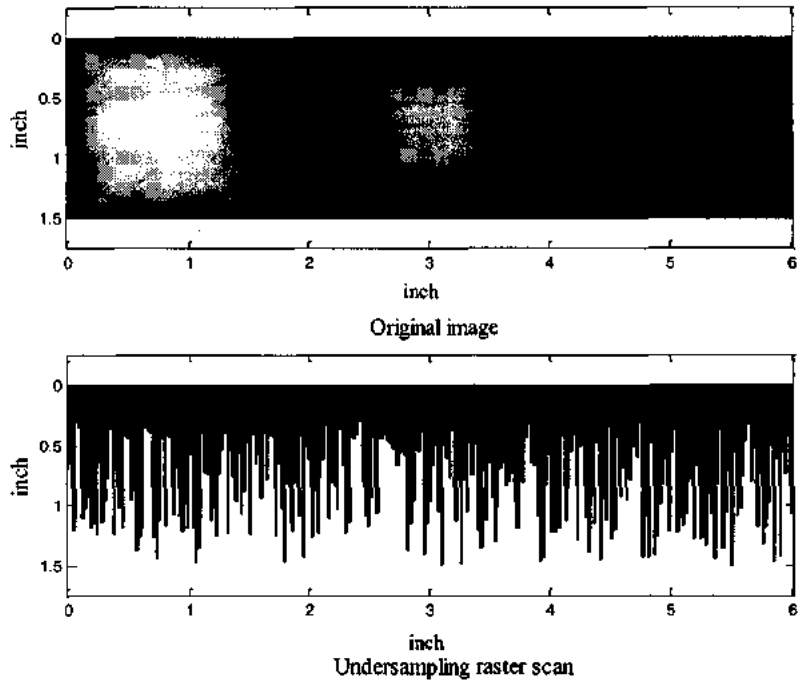


Figure-3.11: Original MWI along with the undersampling pattern

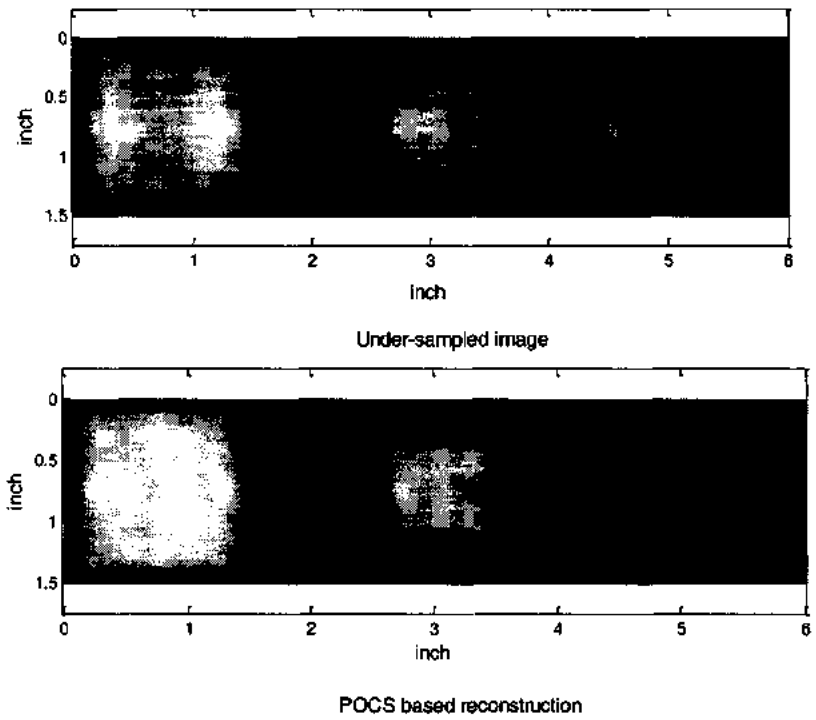


Figure-3.12: POCS based recovery of compressively sampled MWI

3.4 Summary

This chapter presented a common framework for the data acquisition of MRI, parallel-beam CT and microwave imaging. It has been shown that the measurements recorded by the scanners of these imaging modalities can be modeled by a system of linear equations. Fourier transform plays a vital role in the acquisition process. These properties make them suitable for the application of compressed sensing. Finally, a simple POCS based algorithm was used to recover the Fourier-encoded images from less number of random measurements.

CHAPTER-4

COMPRESSIVELY SAMPLED FOURIER-ENCODED IMAGE RECONSTRUCTION USING SEPERABLE SURROGATE FUNCTIONAL

In this chapter, a novel CS recovery technique is proposed that is based on the idea of separable surrogate functional (SSF) method. Like POCS technique, the proposed algorithm iterates between soft-thresholding in sparsifying domain and incorporates the data-consistency constraint in the Fourier domain. However, the reconstruction quality is improved by incorporating the linear estimate of the residual error. The performance of the algorithm is validated using the real human head as well as phantom MR images taken from the MRI scanner. The results of recovery are compared with the POCS and Low-Resolution reconstruction methods based on the standard metrics like improved signal-to-noise ratio, correlation and artifact power (AP). The method is also applied to faithfully recover other Fourier-encoded biomedical images such as parallel-beam CT and MWI.

4.1 Rapid imaging and compressed sensing

Compressed Sampling /Sensing technique facilitates simultaneous acquisition and compression of compressible or sparse signals and has the potential to reduce the scan time of biomedical images during the acquisition. Unlike the hardware-based acceleration, compressed sensing is an algorithmic reduced acquisition method.

In the real world biomedical applications, higher temporal resolution and lower radiation dose have been constantly pursued. The application of CS to Fourier encoded images such as MRI is useful because of the fact that the data acquisition process in

MRI is inherently sequential and the scan time increases linearly with the number of samples taken in the frequency domain (k -space) [74,75] .

One way to reduce the acquisition time in MRI is to decrease the repetition time (TR) by applying stronger gradients for shorter time, that is rapid switching. However, high gradient amplitudes and rapid switching can produce peripheral nerve stimulation leaving little room for MR scanners to improve the imaging speed through the hardware design implementation [76].

The MR imaging time can also be reduced by acquiring more k -space lines (phase encoding steps) in one radio frequency (RF) excitation as in the echo-planer imaging (EPI) [77,78]. However, this limits the amount of spatial information that can be recorded in a single readout resulting in a lower signal to noise ratio (SNR). Another way to reduce the MR data acquisition time is to under-sample the k -space by skipping every other phase encoding line. This can be achieved at the cost of smaller field of view (FOV) that contributes to the aliasing (folding over) of the original image [79, 80].

To increase SNR and improve the imaging speed, simultaneous data acquisition with multiple receive coils in MR scanners have been used which is known as parallel imaging (PI) [81-83]. However, the final image reconstruction needs coil sensitivities information, which is sometimes difficult to measure with high accuracy [7, 84].

The imaging speed of MRI can also be accelerated by using non-Cartesian sampling such as radial or spiral instead of the conventional Cartesian sampling. Although sampling along the spiral trajectories well utilizes the gradient system hardware, the reconstructions from non-Cartesian sampling are not generally robust to system imperfections [6,85].

Accelerating MR measurements using CS exploits the sparsity of MR images during the reconstruction from partial Fourier data. The requirement of incoherent sampling can be achieved with the variable density k -space sampling method to reduce aliasing artifacts during the MR image reconstruction. Variable density sampling scheme sufficiently sample the center of the k -space that contains most of the energy of MR images and significantly under sample the outer k -space region to reduce the scan time [62,86].

Besides MRI, other potential applications of CS in biomedical imaging are CT and MWI [87-91]. The acquisition time of CT is faster as compared to MRI but it involves exposure to ionizing x-ray radiations. The commercially used CT scanners are mostly based on the analytical reconstruction techniques such as filtered back projection (FBP). The traditional FBP algorithm can reconstruct the final image accurately when the projection data are densely sampled. However, if the projection data is sub-sampled for the purpose of reducing the radiation dose, the analytic algorithms yield reconstructed image with severe aliasing artifacts [92-93]. As CS reconstruction techniques have a significant potential to recover the undersampled image, it can be applied to reduce the radiation dose in CT.

In this chapter, we develop a simple CS-based iterative method that can be used to reconstruct the Fourier encoded images (MRI, parallel-beam CT and MWI) from less number of samples. The algorithm solves the l_1 -regularized least square problem to recover the final image from compressively sampled measurements.

4.2 l_1 -regularized least square problem for Orthonormal basis

The general l_1 -regularized least square problem involves solution to the following mixed $l_1 - l_2$ cost function:

$$f(\mathbf{x}) = \frac{1}{2} \|\mathbf{y} - \mathbf{A}\mathbf{x}\|_2^2 + \beta \|\mathbf{x}\|_1 \quad (4.1)$$

Here $\mathbf{A} \in \mathbb{R}^{m \times n}$, $\mathbf{y} \in \mathbb{R}^m$ and $\mathbf{x} \in \mathbb{R}^n$ are the sensing matrix, measurement vector and estimated signal or image respectively. $\beta \in \mathbb{R}$ is the Lagrangian multiplier.

If the basis are orthonormal i.e. $\mathbf{A} = \mathbf{\Psi}$ (with $\mathbf{\Psi}^H \mathbf{\Psi} = \mathbf{I}$), minimizing the objective function of Eq-4.1 is quite simple. Utilizing the fact that unitary matrices preserves the length after transformation. i.e. $\|\mathbf{\Psi}\mathbf{x}\|_2^2 = \|\mathbf{\Psi}^H \mathbf{x}\|_2^2 = \|\mathbf{x}\|_2^2$:

$$\begin{aligned} f(\mathbf{x}) &= \frac{1}{2} \|\mathbf{y} - \mathbf{\Psi}\mathbf{x}\|_2^2 + \beta \|\mathbf{x}\|_1 \\ &= \frac{1}{2} \|\mathbf{\Psi}(\mathbf{\Psi}^H \mathbf{y} - \mathbf{x})\|_2^2 + \beta \|\mathbf{x}\|_1 \\ &= \frac{1}{2} \|\mathbf{x} - \mathbf{\Psi}^H \mathbf{y}\|_2^2 + \beta \|\mathbf{x}\|_1 \\ &= \frac{1}{2} \|\mathbf{x} - \mathbf{x}_0\|_2^2 + \beta \|\mathbf{x}\|_1 \\ &= \sum_{i=1}^n \left[\frac{1}{2} (x_i - x_{0i})^2 + \beta |x_i| \right] \end{aligned}$$

Here $\mathbf{x}_0 = \mathbf{\Psi}^H \mathbf{y}$ is the projection of lower dimensional signal onto the original higher dimension space. The last step shows that the overall problem reduces to n independent one-dimensional problems which can be solved using soft-thresholding of Eq-3.11. So if matrix \mathbf{A} is unitary, the minimizer of Eq-4.1 can be obtained in two steps: (1) Find back-projection using $\mathbf{x}_0 = \mathbf{\Psi}^H \mathbf{y}$ and (2) applying thresholding $T_\beta(\cdot)$ to individual entries of \mathbf{x}_0 .

In the CS recovery problem, the sensing matrix $\mathbf{\Phi}$ is not unitary (and perhaps non-square). However, the problem can be addressed in various ways to use the shrinkage

tools. One approach is to use proximal splitting methods, which is a natural extension of POCS [55,94].

4.3 Proposed Recovery algorithm

The SSF algorithm is proximal algorithm. It works on the idea that instead of minimizing the original cost function of Eq-4.1, a surrogate function $\tilde{f}(\mathbf{x})$ can be used to get a closed form expression for its global minimizer. The new objective function is obtained by adding a distance term $d(\mathbf{x}, \mathbf{x}_0)$ to the original function. Starting with an initial vector \mathbf{x}_0 , and a suitable constant c , the solution to the following simpler optimization problem (based on the proximal functions) can be easily computed:

$$\begin{aligned}
\operatorname{argmin}_{\mathbf{x}} \tilde{f}(\mathbf{x}) &= \operatorname{argmin}_{\mathbf{x}} [f(\mathbf{x}) + d(\mathbf{x}, \mathbf{x}_0)] \\
&= \operatorname{argmin}_{\mathbf{x}} [f(\mathbf{x}) + \frac{c}{2} \|\mathbf{x} - \mathbf{x}_0\|_2^2 - \frac{1}{2} \|\Phi\mathbf{x} - \Phi\mathbf{x}_0\|_2^2] \\
&= \operatorname{argmin}_{\mathbf{x}} [\frac{1}{2} \|\mathbf{y} - \Phi\mathbf{x}\|_2^2 + \beta \|\mathbf{x}\|_1 + \frac{c}{2} \|\mathbf{x} - \mathbf{x}_0\|_2^2 - \frac{1}{2} \|\Phi\mathbf{x} - \Phi\mathbf{x}_0\|_2^2] \\
&= \operatorname{argmin}_{\mathbf{x}} \frac{1}{2} \|\mathbf{x} - \mathbf{z}_0\|_2^2 + \frac{\beta}{c} \|\mathbf{x}\|_1
\end{aligned}$$

The last step can be obtained after a simple mathematical manipulation with $\mathbf{z}_0 = \frac{1}{c} \Phi^T(\mathbf{y} - \Phi\mathbf{x}) + \mathbf{x}_0$. The closed form solution for the minimizer of the surrogate function $\tilde{f}(\mathbf{x})$ can be obtained by applying shrinkage on \mathbf{z}_0 with thresholding parameter equal to $\frac{\beta}{c}$ i.e.

$$\hat{\mathbf{x}} = T_{\beta/c}(\mathbf{z}_0) = T_{\beta/c} \left(\frac{1}{c} \Phi^T(\mathbf{y} - \Phi\mathbf{x}) + \mathbf{x}_0 \right) \quad (4.2)$$

To use SSF for the recovery of compressively sampled Fourier-encoded biomedical images, one needs to minimize the proximal function corresponding to the following cost function (in Lagrangian form):

$$f(x) = \frac{1}{2} \|y - F_u x\|_2^2 + \beta \|\Psi x\|_1 \quad (4.3)$$

The proposed SSF based method iteratively obtain the minimizer of Eq-4.3 by updating the recovered image using the following update equation (derived from Eq-3.5):

$$\hat{x}_{i+1} = \Psi^{-1} \left\{ T_{\beta/c} \left(\Psi \left(\frac{1}{c} F^{-1} (y - F x_i) + x_i \right) \right) \right\} \quad (4.4)$$

The algorithm is initialized with an initial guess that is computed by filling in the uncollected Fourier data with zeros. This essentially corresponds to the least square solution of the undersampled image and is severely degraded by noise artifacts due to undersampling. Shrinkage in the Wavelet or DCT domain is applied to sparsify the image. The proposed algorithm estimates the missing Fourier coefficients due to undersampling, while the already acquired Fourier data remain unchanged. The detailed steps involved in the proposed technique are shown in Fig-4.1. It also depicts the block diagram of the SSF based recovery algorithm. The block ‘‘POCS’’ in Fig-4.1 refers to the steps involved in the diagram of Fig-3.8. The SSF based recovery algorithm utilizes POCS but it applies the thresholding step on the linear combination of the back-projected error term and the previous estimate.

Various stopping criteria such as achieving the desired fitness value or attaining a fixed number of iterations can be used to halt the execution of the algorithm. The fitness at the t^{th} iteration can be computed through $\|F_u x_t - y\|_2^2$.

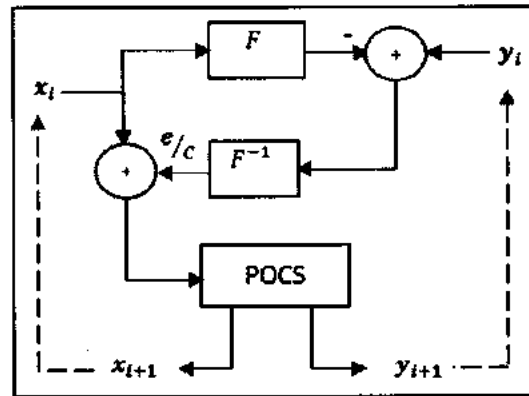
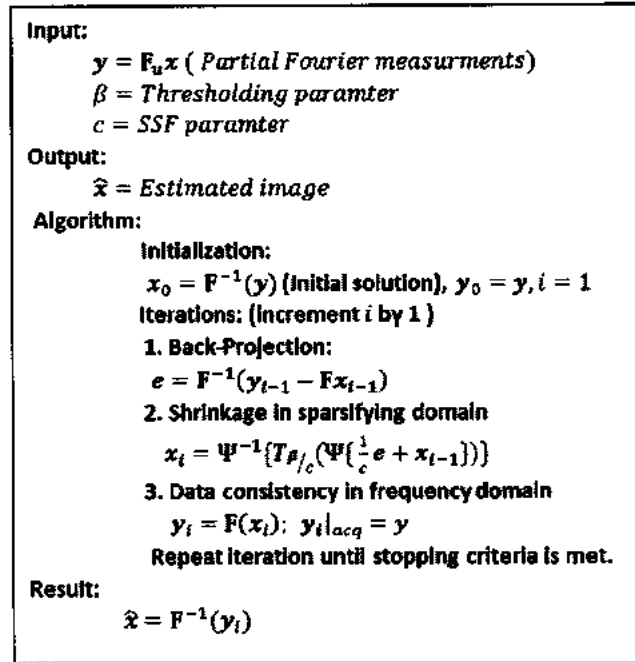


Figure-4.1: The proposed SSF based recovery algorithm (with block diagram)

4.4 Recovery of MR images using the proposed algorithm

We apply the proposed SSF based algorithm to faithfully recover the original human brain and phantom MR images from partial Fourier data. Both of these data sets are acquired through 1.5 Tesla GE HDxt scanner with an eight-channel head coil and a gradient echo sequence with the following parameters: TR/TE=55/10 msec, FOV

=20 cm, bandwidth=31.25 KHz, slice thickness= 3 mm flip angle= 90^0 , matrix size= 256×256 at St. Mary's Hospital London. Fig-4.2 shows both the original brain and phantom images used in the experiments.

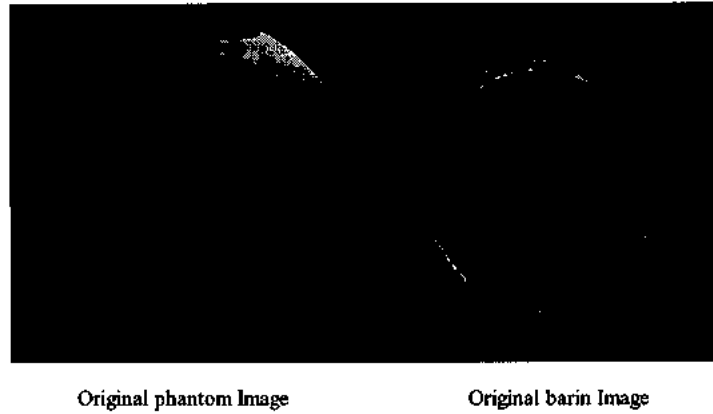


Figure-4.2: Original phantom and brain images taken from the MRI scanner.

The images are undersampled 4-fold in the Fourier domain using variable density sampling. These undersampled images are then reconstructed with the proposed method using Wavelet (Daubechies 4) as the sparsifying transform. The proposed algorithm removes the incoherent artifacts due to the undersampling and essentially acts like a denoising algorithm.

To compare the final results, we also use zero-filling (ZF), low resolution (LR) and POCS techniques to reconstruct the original image. ZF linearly reconstructs the undersampled image by zero-filling the missing k -space data. For LR, the image data is acquired with the same number of data points containing centric-ordered data around the center of the k -space.

The proposed algorithm is initialized with ZF as an initial guess. Other parameters for the reconstruction algorithms are set as follows: number of iterations=10 and SSF

constant $c = 100$. Optimum values of β are selected empirically for each case to have a better performance comparison. Fig-4.3 shows the phantom image reconstruction using LR, POCS and the proposed SSF based techniques along with the Fourier sampling masks. To further emphasize the reconstruction accuracy of proposed algorithm, the final reconstructed phantom image with the proposed algorithm is shown in Fig-4.4. The difference of the recovered image with the original phantom image is also given indicating the accuracy of the algorithm. The improvement in terms of the SSIM at each iteration is depicted in Fig-4.5 for POCS and SSF based recovery. It is clear from the figures that the proposed method is able to reconstruct the phantom image faithfully as compared to LR and POCS.

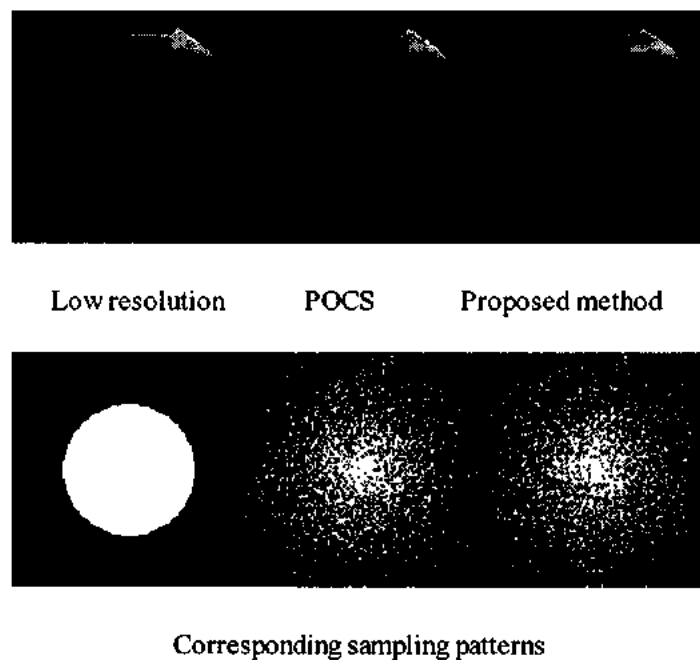


Figure-4.3: Recovery (phantom MRI) using various techniques

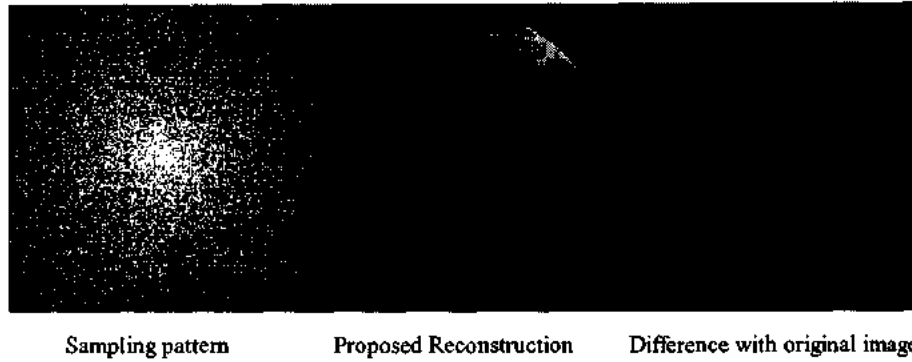


Figure-4.4: Recovery of phantom image with proposed algorithm.

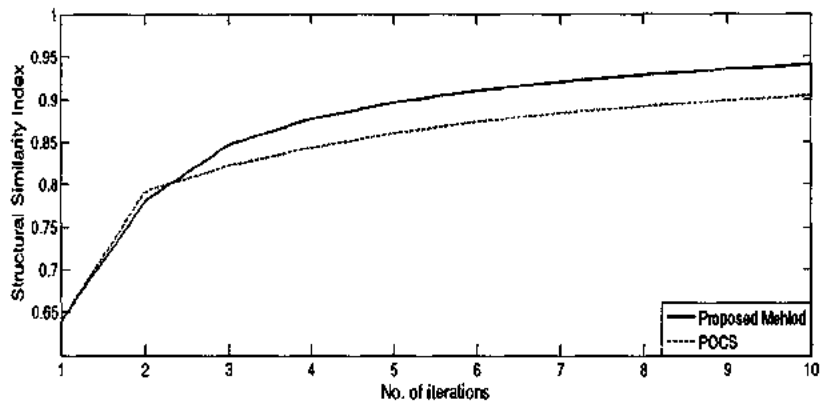


Figure-4.5: Comparison (phantom MR image) based on Structural similarity (SSIM)

The reconstruction accuracy of the proposed algorithm, based on the parameters like ISNR, AP and correlation, has also been shown using the human brain image. Fig-4.6 shows the graphical comparison of POCS and SSF methods on the basis of ISNR, while Fig-4.7 depicts the decrease in the reconstruction cost function at each iteration. It is clear that the proposed SSF-based method yields better performance in the fixed number of iterations. The final brain images reconstructed with ZF, LR, POC and SSF-based methods are given in Fig-4.8. The reconstruction accuracy of the proposed

method can be seen from the outstanding difference of each recovered image with the original MR image. It is clear that the image reconstructed with SSF based algorithm is very close to the original image.

The parametric comparison of the proposed algorithm with other techniques in terms of correlation, PSNR and artifact power, are as given in Table-4.1.

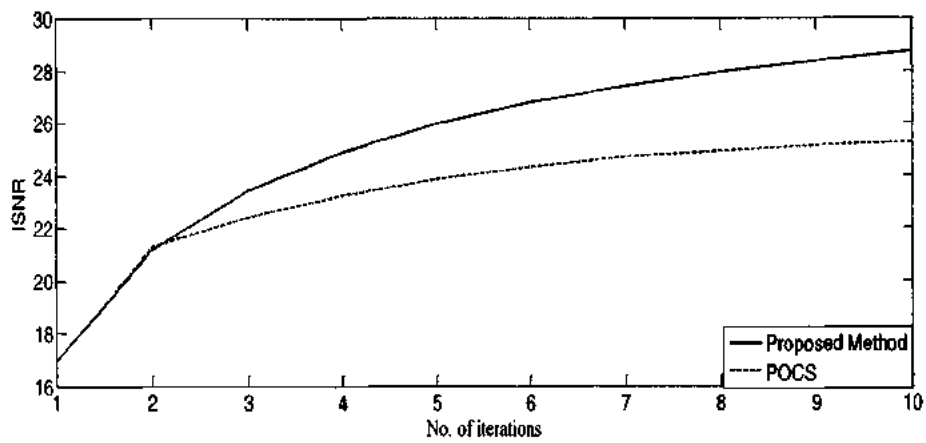


Figure-4.6: Comparison based on ISNR (brain image)

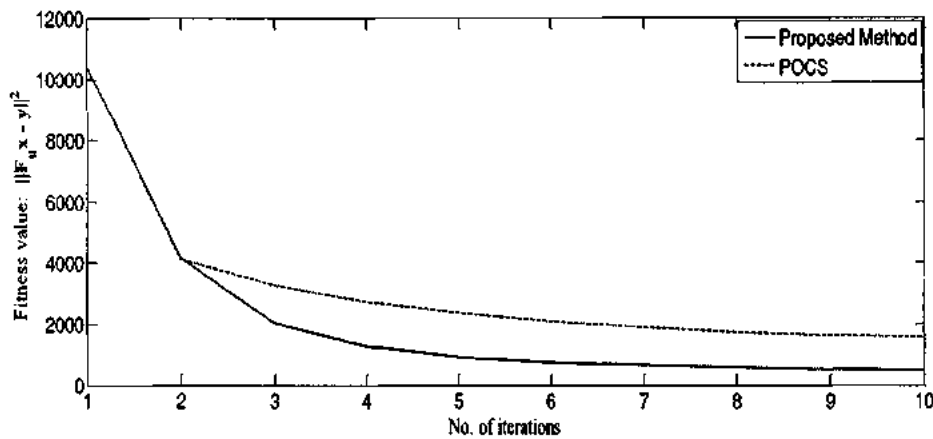


Figure-4.7: Comparison on the basis of fitness value (brain image)

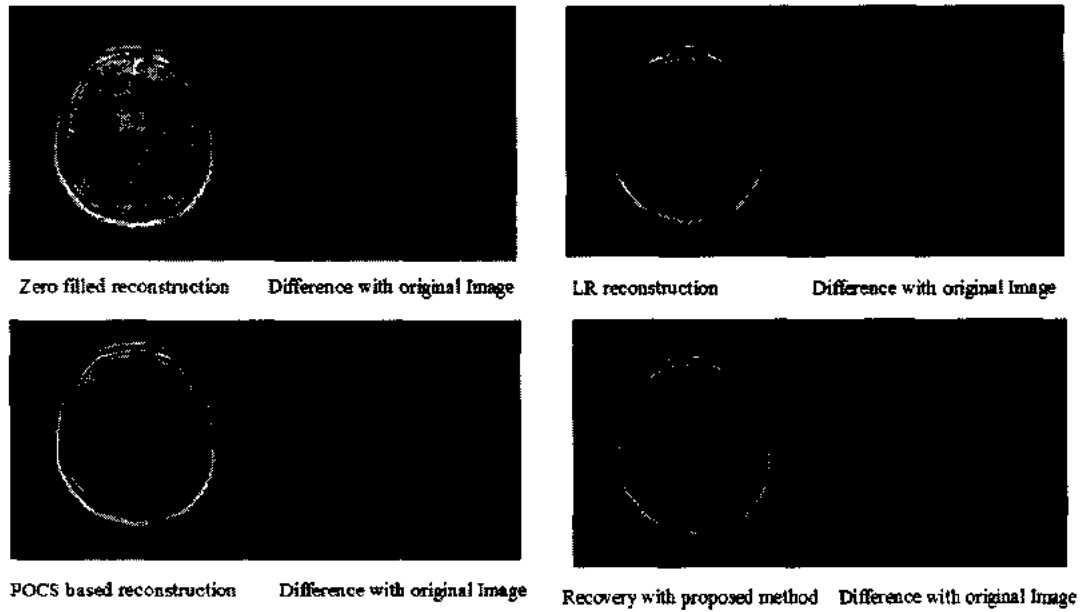


Figure-4.8: Difference of the recovered images with the original brain image.

	PSNR	Artifact power	Correlation
LR	8.6419	0.0062	0.9796
POCS	16.3936	0.0047	0.9965
SSF	20.9532	0.0022	0.9982

Table-4.1: Comparison of MR brain image based on PSNR, AP and correlation

4.5 Recovery of parallel beam CT using the proposed method

The proposed SSF based algorithm can be used to recover the original CT image from a reduced set of projections. It brings the projection data into the Fourier domain ensuring data consistency during each iteration. To apply the algorithm, a 512×512 Shepp-Logan is generated, as shown in Fig-4.9(a). Each pixel value of the image represents the attenuation coefficient. The projection data is generated by computing

the line integrals across the image at various angles. It is shown in Fig-4.9(b) and is commonly known as ‘sinogram’.

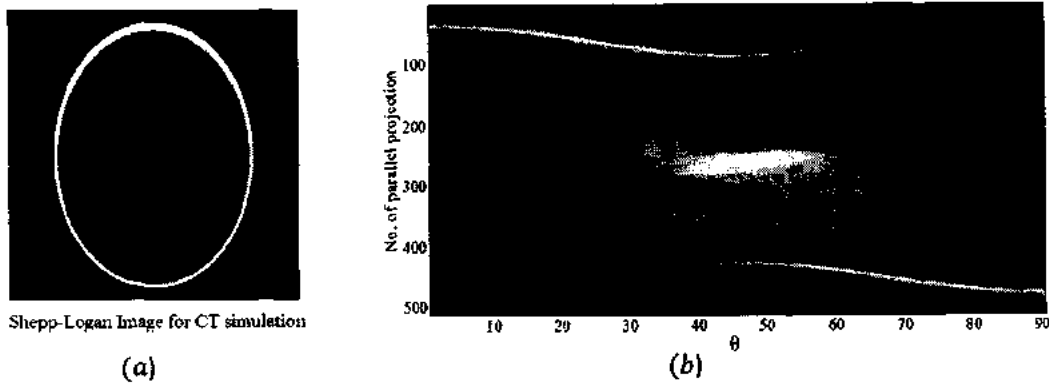


Figure-4.9: CT phantom image (a) and corresponding sinogram (b)

The image is compressively sampled in the Fourier domain using radial lines. The star-shaped sampling pattern is shown in Fig-4.10(a) that is used to acquire only 43028 Fourier measurements of the original image. Fig-4.10(b) shows the reconstructed image that is computed by replacing the missing data with zero. This corresponds to the minimum energy solution.

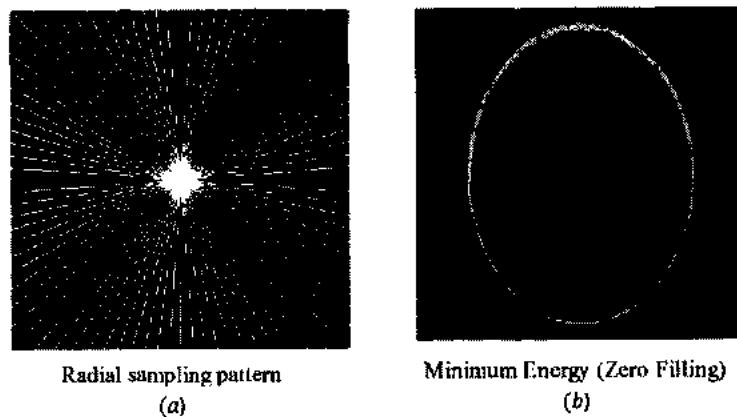


Figure-4.10: (a) undersampling pattern (b) aliased CT image

The proposed algorithm is compared with POCS based recovery and filtered back projection (FBP) reconstruction. The necessary parameters of the proposed recovery algorithms such as SSF constant c , number of iterations etc. are kept the same as those used for MR experiments. Normally TV is used as sparsifying transform for CT reconstruction. However, in our experiment we use Wavelet domain for thresholding. The final reconstructed images with FBP, POCS and SSF based algorithms are shown in Fig-4.11 having Peak-Signal-to-Noise ratios 63.38 db, 74.71 db and 80.16 db respectively.

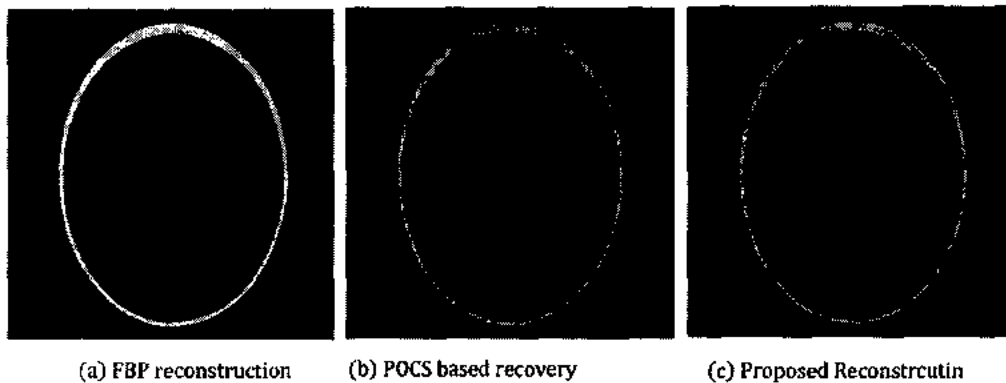


Figure-4.11: Final reconstructed CT image with various algorithms

4.6 Reconstruction of MWI using SSF based method

The CS based near field microwave imaging experiment was performed in our group at the Electromagnetic and Acoustic Imaging and prognostics (LEAP) lab of the University of Colorado Denver and Anschutz Medical Campus, using a customized coaxial tip antenna with the following imaging parameters: excitation frequency = 10 GHz, lift-off distance = 1mm (much smaller than a couple of wavelengths) and step

size = 5×5 steps where 1 inch=200 steps. A 6×1.5 inches microwave backscattering image is acquired by using raster scanning for a sample under-test (SUT), shown in Fig-4.12. It is worth noting that the spatial resolution using this high resolution microwave imaging technique exceeds the Abbe's limit (best spatial resolution determined by half wavelength, which is 1.5 cm here) by measuring the evanescent waves in the near field regime. Millimeter-to sub-mm scale resolution has been obtained under current imaging setup. However, the point to point raster scanning mode make the data acquisition (DAQ) tedious and time consuming. For CS reconstruction the SUT is compressively undersampled using a sampling mask shown in Fig-4.13 during DAQ phase. The probe stop at a random position while scanning the SUT line by line. The undersampled image obtained is noisy and blurred.

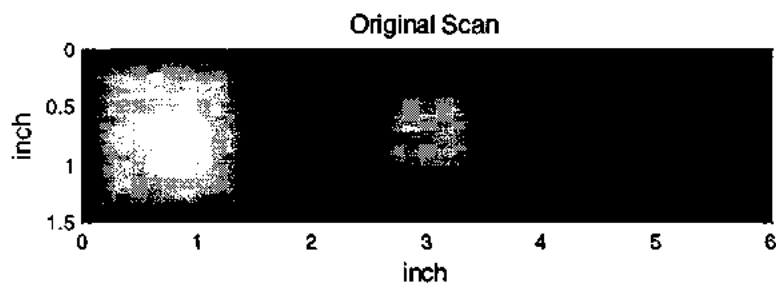


Figure-4.12: fully sampled SAR image of SUT

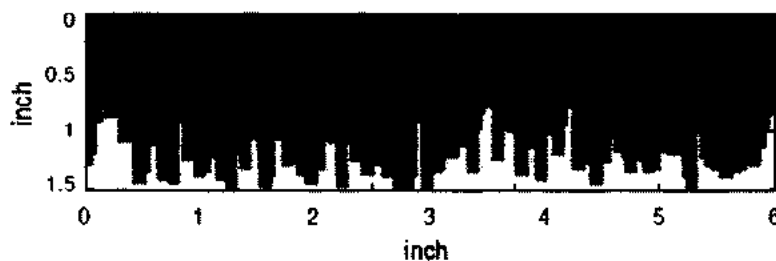


Figure-4.13: Selective raster scanning for MWI acquisition

The proposed algorithm is applied to recover the original microwave image from the under sampled image which is illustrated in Fig-4.14. Here DCT is used as a sparsifying transform i.e. $\Psi = \text{DCT}$ matrix. The rest of the parameters for the reconstruction algorithm are the same as those used for MR and CT recovery problems.

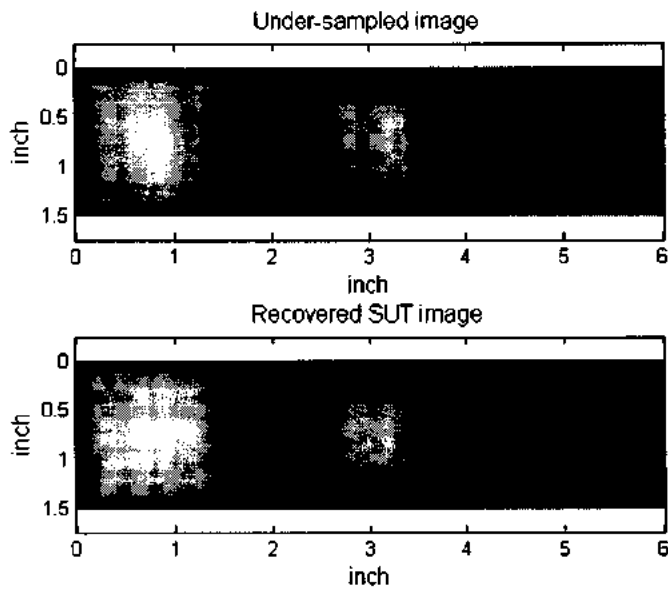


Figure-4.14: Under-sampled (top) and recovered microwave image (bottom)

The aforementioned three experiments of Fourier encoded biomedical imaging validates that the proposed SSF based recovery algorithm can be used to reconstruct the original MR, parallel beam CT and MW images from compressively sampled data.

4.7 Summary

A novel CS reconstruction method for under-sampled Fourier-encoded images has been presented. The recovery technique is based on the SSF algorithm with data consistency ensured in the frequency domain. The proposed technique iteratively implements

shrinkage in the wavelet domain to minimize the mixed $l_1 - l_2$ reconstruction cost function. During each iteration, the algorithm synthesizes the missing Fourier data using back-projection and soft-thresholding, making the final image close to the original. It has been demonstrated that the proposed technique can be used to faithfully reconstruct the phantom as well as the original MR, parallel beam CT and microwave images from compressively sampled data. The experimental results show that the SSF-based recovery technique as applied to the partial Fourier data outperforms the LR, POCS, FBP and linear recovery methods in term of PSNR, AP, correlation and ISNR.

CHAPTER-5
SPARSE SIGNAL RECONSTRUCTION USING HYBRID EVOLUTIONARY
ALGORITHMS

This chapter presents some novel ideas of recovering a k -sparse (1-D) signal from compressed measurements using evolutionary techniques such as genetic algorithms (GA) and particle swarm optimization (PSO) along with iterative shrinkage algorithms. The proposed hybrid mechanisms with proper regularization constraints not only accelerate the convergence of the evolutionary algorithms, but also estimate the original sparse signal with an acceptable precision. Finally, a modified POCS algorithm for Fourier-encoded images is presented that can recover the biomedical images from compressively sampled incomplete Fourier data. The proposed algorithm is based on the combined idea of POCS and evolutionary computing techniques, specifically genetic algorithms.

5.1 Evolutionary algorithms

Unlike heuristic algorithms, deterministic algorithms are mathematically elegant, but require a good starting point for convergence and are never user-friendly. GA and PSO are examples of evolutionary algorithms which are simpler, but lack rigorous mathematical foundations [95]. These algorithms are considered to be unconstrained search techniques. So the application of GA and PSO for solving constrained optimization is quite challenging [96-99]. Heuristic algorithms are considered suitable for solving computationally intractable problems of the form:

$$\hat{\mathbf{x}} = \underset{\mathbf{x}}{\operatorname{argmin}} \|\Phi \mathbf{x} - \mathbf{y}\|_2^2 \text{ subject to } \|\mathbf{x}\|_0 \leq k \quad (5.1)$$

However to speed up the convergence, a deterministic algorithm is required for solving the l_0 minimization problem of (5.1) [100].

5.1.1 Particle Swarm Optimization (PSO)

PSO is a general-purpose heuristic optimization approach having simple structure that uses a population (group of candidate solutions) of search agents called particles [101-104]. The PSO based algorithm assigns randomized velocities to each particle to explore the search space. The velocities of particles are iteratively updated, based on their previous velocities and their distances from local and global bests. The velocity update equation is given by [105]:

$$\mathbf{v}_i = w \times \mathbf{v}_{i-1} + c_1 r_1 (\mathbf{p}_i - \mathbf{x}_{i-1}) + c_2 r_2 (\mathbf{p}_g - \mathbf{x}_{i-1}) \quad (5.2)$$

Where c_1 , c_2 are problem dependent constants while r_1 and r_2 are two different uniformly distributed random numbers in the interval (0,1). The scalar $w \in [0,1]$ is the inertial weight. \mathbf{p}_g is the particle having best fitness in the entire population and is referred to as global best. \mathbf{p}_i is the local best that represents the best previous position of i th particle as determined by the cost function. Varying the free parameters c_1 , c_2 and the inertial weight w can greatly affect the performance of the algorithm [106].

In the conventional PSO, the position \mathbf{x}_i of the i^{th} particle is updated according to its velocity:

$$\mathbf{x}_i = \mathbf{x}_{i-1} + \mathbf{v}_i \quad (5.3)$$

The algorithm generally starts with a random population of size ranging from 20 to 50 particles depending on problem. During each iteration, particles move based on their velocity while the velocity itself is updated using the global and local best positions.

5.1.2 Genetic Algorithms (GA)

Genetic algorithm is another heuristic algorithm that is based on the principles of genetics [107-110]. In GA, every individual in the population is referred to as a chromosome that acts as a candidate solution. The chromosome comprises of elements that are called genes. The effectiveness or cost of each chromosome is determined through a fitness function ($\|\Phi\mathbf{x} - \mathbf{y}\|_2^2$). With the help of cross over, the genes of different chromosomes (parents) can be combined in a variety of ways to produce the offsprings having different fitness values. The new population is formed with the natural selection by combining the best (in terms of fitness) parents and offsprings. In this way the algorithm proceeds to search for the best candidate solution (chromosome). The steps involved in using GA to solve an optimization problem are shown in Fig-5.1 [108,111].

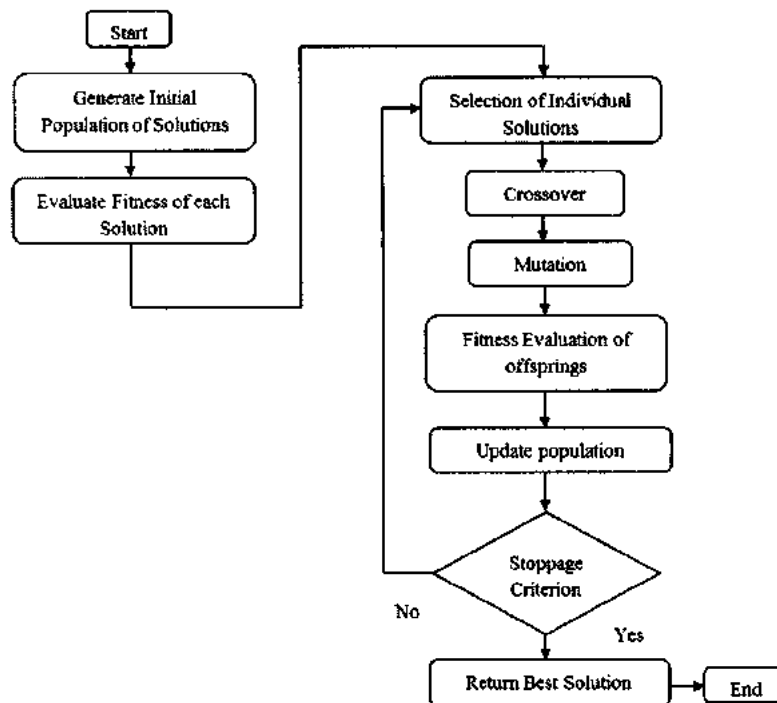


Figure-5.1: Flow chart of generic GA

In spite of many achievements, one of the main problems of GA is the premature convergence which is related to the loss of genetic diversity of the population [112-113]. One way to avoid this problem is through mutation. However, for sparse signal recovery, the ordinary mutation will not work, making the chromosome denser and compromising the sparsity constraint. Constraints can be incorporated in the fitness function (indirect constraint handling) as well as in the chromosomes (direct constraint handling). However, indirect constraint handling does not work well for the sparse problems [96,114].

5.2 The Proposed Hybrid Particle Swarm Optimization

The proposed technique uses a combination of stochastic (PSO) and deterministic (SSF) algorithms to solve the sparse recovery problem for solving the constrained optimization of (5.1). The desired sparsity level is guaranteed in all the initial particles (population). However, the particles lose their sparsity after velocity updates, so hard thresholding is followed by the next position update to make sure that the sparsity constraint is properly maintained throughout.

When the fitness (mean square error) of the global best particle does not change in the specified iterations, then SSF algorithm is accessed to update the position of the second best particle in the population using:

$$\mathbf{x}_i = T_\beta(\mathbf{x}_{i-1} + rand \times \Phi^T(\mathbf{y} - \Phi\mathbf{x}_{i-1})) \quad (5.4)$$

where *rand* is a positive random number and T_β is the shrinkage operator with threshold β . The loss of sparsity is compensated by using the hard thresholding after each SSF update.

Figure-5.2 describes the proposed hybrid PSO algorithm in detail for Matlab implementation. The vector **indx** contains the indices of the array when sorted in the descending order. The hard thresholding operator $[z]_k$ sets all except the k largest elements of vector z to zero.

<p>Input: Dictionary $\Phi \in R^{m \times n}$, compressed measurement $y \in R^m$, sparsity level k, population size N, PSO parameters c_1, c_2 and w. SSF parameter β for thresholding. Output: A k-sparse vector $x \in R^n$</p>
<p>1) Initialization: Generate N particles randomly with desired sparsity level $X = [x_1, x_2, \dots, x_N]$, $x_i \in R^n$ and $\ x_i\ _0 \leq k \quad \forall i \leq 1 \leq N$ $V = 0$, Velocity matrix</p> <p>2) Fitness Evaluation: Compute fitness of each particle $f_x = fit(x_1, x_2, \dots, x_N)$ $= [f_1, f_2, \dots, f_N]$, $f_i = (\Phi x_i - y)^T (\Phi x_i - y)$ $[f_{xs} \text{ indx}] = \text{sort}(f_x, \text{descend})$ $f_{xs} = [f_{x1}, f_{x2}, \dots, f_{xN}]$ With $f_{x1} < f_{x2} \dots < f_{xN}$</p> <p>3) Local and global best (Initial): Matrix P contains local best particles $P = X(\text{indx})$ $= [p_1, p_2, \dots, p_N]$ where p_i has fitness f_{xi} $p_g = p_1$, initial global best</p> <p>4) Velocity & Position update: Velocity and position update of each particle according to Eq-5.2 and Eq-5.3 respectively. $V = \text{velocity}(V, P, X, p_g, c_1, c_2, w)$ $= [v_1, v_2, \dots, v_N]$ $X = \text{position}(X, V)$ $= [x_1]_k, [x_2]_k, \dots, [x_N]_k$, where $x_i = x_{i-1} + v_i$</p> <p>5) SSF Algorithm: If f_{x1} remains the same in the specified consecutive iterations then replace the second particle with SSF update: $x_2 = T_\beta(x_1 + \text{rand} \times \Phi^T(y - \Phi x_1))$, $\ x_2\ _0 \leq k$</p> <p>6) Update local and global best: Based on fitness, local and global best particles are updated $f_{x2} = fit(X)$ $[f_{x2s} \text{ indx}] = \text{sort}(f_{x2}, \text{descend})$ $f_{x2s} = [f_{x21}, f_{x22}, \dots, f_{x2N}]$ With $f_{x21} < f_{x22} \dots < f_{x2N}$ $X_2 = X(\text{indx})$ $= [x_{21}, x_{22}, \dots, x_{2N}]$ where x_{2i} has fitness f_{x2i}</p> <p>If $(f_{x21} < f_{x1})$ then $p_g = x_{21}$ and $f_{x1} = f_{x21}$ (new global best)</p> <p>If $(f_{x2i} < f_{xi})$ then $p_i = x_{2i}$ and $f_{xi} = f_{x2i}$, $\forall i \leq 1 \leq N$ (Local bests)</p> <p>Loop to step (4) until the stopping criteria (a sufficiently good fitness or maximum number of iterations) is meet.</p> <p>7) Output: Global best $x = p_g$</p>

Figure-5.2: The proposed hybrid PSO algorithm

5.3 Proposed Hybrid Genetic Algorithm

Solving (5.1) with the conventional GA is not possible as offsprings may not follow the sparsity constraint even if it is fulfilled by the parents. In the proposed algorithm, the direct constraint handling has been used to ensure the desired sparsity level before and after cross-over through hard thresholding. Like hybrid PSO, SSF is used to update a chromosome when the fitness of the best chromosome does not change in a predefined consecutive iterations, thereby preventing the convergence issue. These modifications allow the hybrid GA to recover the sparse signal with an acceptable level of accuracy.

Figure-5.2 lists the detailed description of the proposed hybrid genetic algorithm.

<p>Input: Sensing matrix $\Phi \in R^{m \times n}$, measurement vector $y \in R^m$, sparsity level k, population size N, thresholding parameter β for SSF.</p> <p>Output: An k-sparse vector $x \in R^n$</p>
<p>1) Population Generation: Randomly generate N chromosomes $G = [g_1, g_2, \dots, g_N]$, $g_i \in R^n$ and $\ g_i\ _0 \leq k \quad \forall i \leq 1 \leq N$</p> <p>2) Fitness Evaluation of parents & Sorting: Evaluate the fitness of each chromosome and sort them in the descending order (the lower the fitness, the better the chromosome) $f_p = fit(g_1, g_2, \dots, g_N)$ $= [f_{p1}, f_{p2}, \dots, f_{pN}]$, $f_{pi} = (\Phi g_i - y)^T (\Phi g_i - y)$ $[f_{ps} \text{ indx}] = sort(f_p, \text{descend})$ $f_{ps} = [f_1, f_2, \dots, f_N]$ With $f_1 < f_2 < \dots < f_N$ $G_s = G(\text{indx})$ $= [g_{s1}, g_{s2}, \dots, g_{sN}]$ where g_{si} has fitness f_i</p> <p>3) SSF Algorithm: If f_1 remains the same in the specified consecutive iterations then replace the second particle with SSF update: $g_{s2} = T_\beta(g_{s1} + rand \times \Phi^T(y - \Phi g_{s1}))$, $\ g_{s2}\ _0 \leq k$</p> <p>4) Cross over: offsprings of size half of the population are generated in random fashion: $C = \text{cover}(G_s)$ $= [c_1, c_2, \dots, c_{\frac{N}{2}}]$ $c_j = [g_{sj} + \gamma(g_{sj} - E_{ssrand})]_k \quad 1 \leq j \leq \frac{N}{2} \text{ and } 1 \leq i \leq N$</p> <p>5) Fitness Evaluation of children & Sorting: Same as step-2 but executed for offspring $f_c = fit(c_1, c_2, \dots, c_{\frac{N}{2}})$ $[f_{cs} \text{ indx}] = sort(f_c, \text{descend})$ $C_s = C(\text{indx})$ $= [c_{s1}, c_{s2}, \dots, c_{s\frac{N}{2}}]$</p> <p>6) New population: Generate new population using half of the best parents and all children. $G = [g_{s1}, g_{s2}, \dots, g_{s\frac{N}{2}}, c_{s1}, c_{s2}, \dots, c_{s\frac{N}{2}}]$ Repeat (2) - (6) until the stopping criteria meet.</p> <p>7) Output: The chromosome with best fitness is the candidate solution $x = g_{s1}$</p>

Figure-5.3: The proposed hybrid genetic algorithm for sparse signal recovery

5.4 Results and Discussions

The results produced are based on the random Gaussian measurement matrix $\Phi \in R^{256 \times 512}$. The rows of sensing matrix represent the measurements i.e. $m = 256$ and its columns denote the size of the sparse signal i.e. $n = 512$. This matrix is generated by taking the first m rows of an orthonormal matrix built through Gram-Schmidt procedure using an $n \times n$ matrix consisting of ± 1 random entries. A one-dimensional test signal $\mathbf{x}_0 \in R^{512}$ having sparsity $k=85$ with random support and magnitude is used for sparse signal reconstruction. This signal is compressively sampled to produce the measurement vector $\mathbf{y} = \Phi \mathbf{x}_0 \in R^{256}$. The population size comprising of $N=20$ random particles (chromosomes for GA), having proper sparsity is used in the experiments. The thresholding parameter (β) required for SSF is taken as 0.001. For PSO, the required parameters are set as follows: $c_1 = c_2 = 2$ and inertia weight $w = 0.9$. Fig-5.4 shows the effect of decrease in the cost function by keeping all other simulation parameters same but varying the inertial weight only. It is clear that $w = 0.9$ produces optimum results for the current experiment.

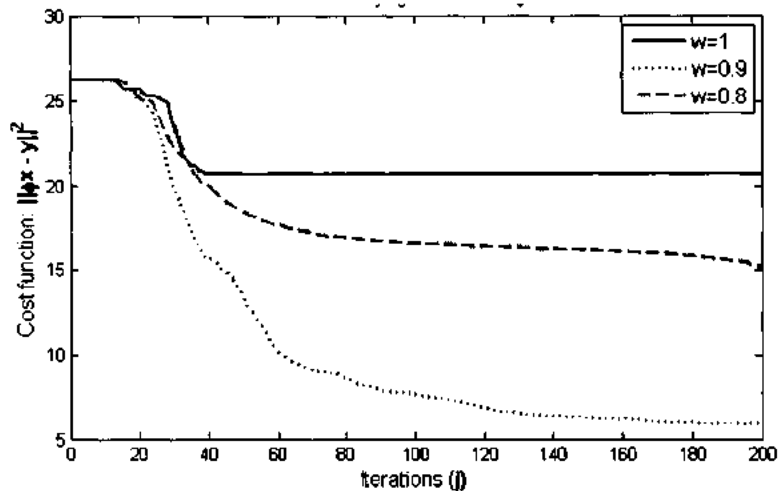


Figure-5.4: Performance of PSO with varying inertial weights

Figure-5.5 shows how the proposed algorithm accelerates the convergence of the conventional PSO. In the initial iterations, the SSF is not used, so the decrease in the cost function is similar for both PSO and hybrid algorithm. However, when the algorithm starts using SSF based on the access criteria, then the convergence of the proposed method becomes faster.

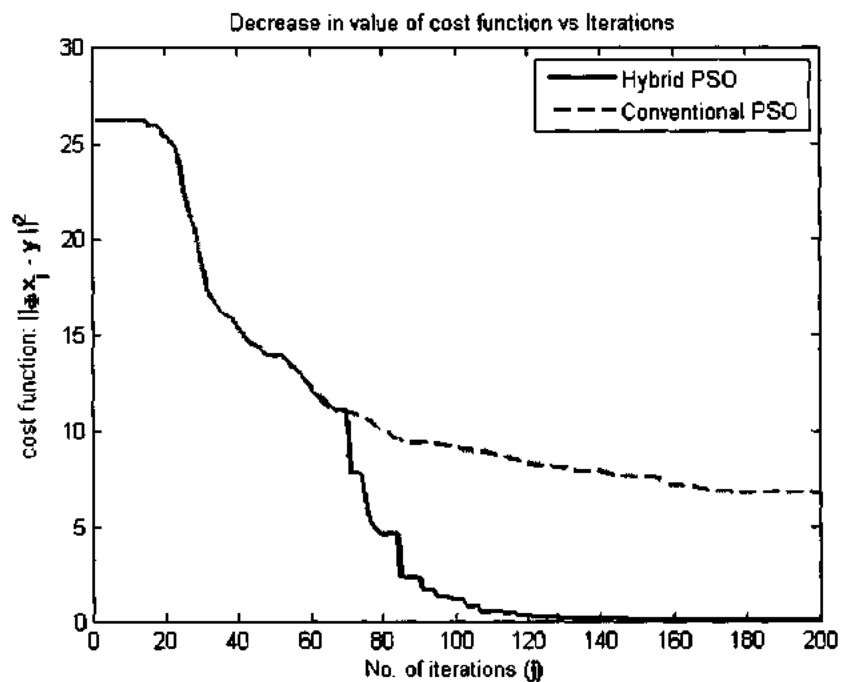


Figure-5.5 showing fast convergence achieved with the proposed method

Fig-5.6 shows the signal amplitude values of recovered signal using conventional and the proposed hybrid PSO only. It is clear that the sparse signal reconstruction with the proposed algorithm can recover both the support as well as the signal amplitude values to an acceptable limit.

Similarly, integrating SSF with GA also produces similar results. Fig-5.7 shows the comparison of hybrid GA with parallel coordinate descend (PCD) and SSF based on the normalized MSE.

Table-5.1 lists the performance comparison based on other parameters like fitness value and correlation of the final reconstructed signals through various algorithms showing that the proposed hybrid algorithms can recover the original test signal precisely.

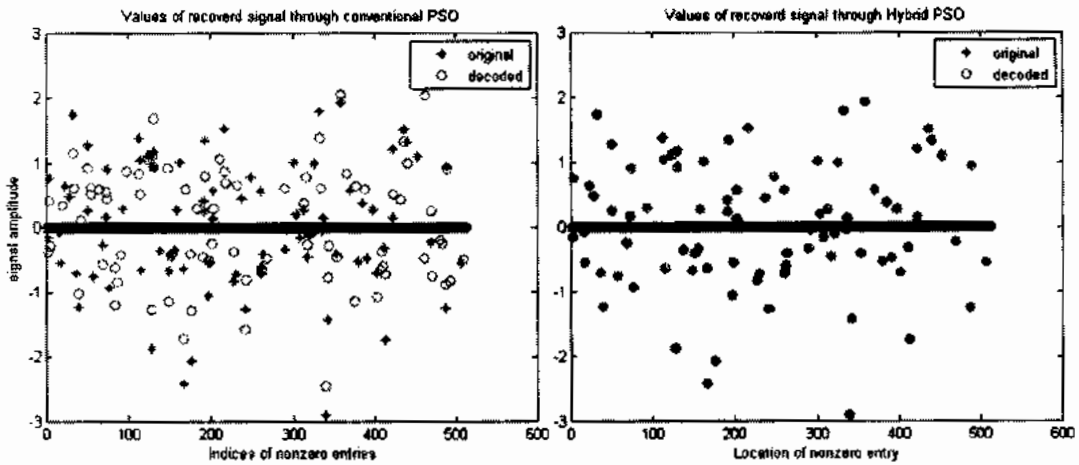


Figure-5.6: Signal reconstruction through conventional and hybrid PSO

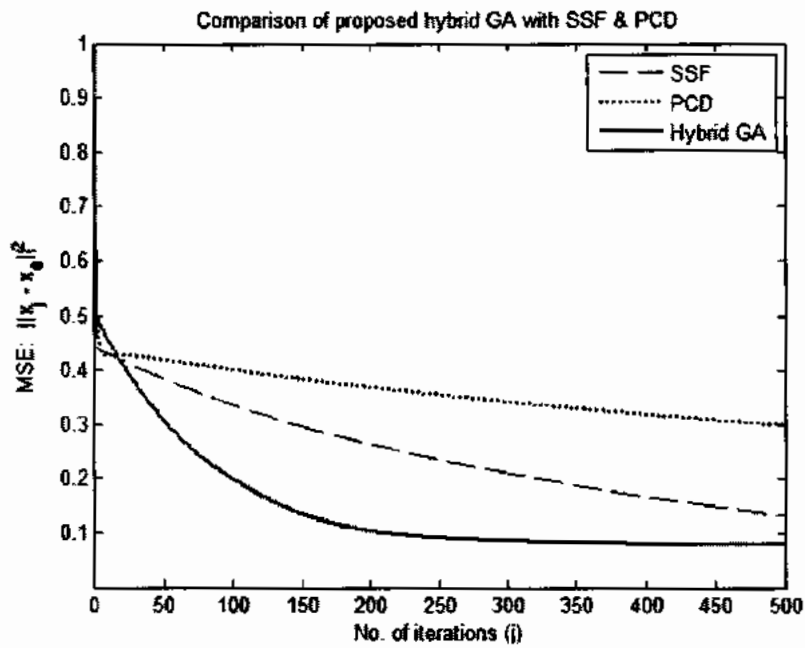


Figure-5.7: Comparison of hybrid GA based on mean-square-error

Algorithm Used	Correlation	MSE	Fitness
SSF	0.9087	0.2017	2.7383
PCD	0.7195	0.4836	6.8735
PSO	0.8563	0.2668	5.1068
GA	0.6102	0.6276	11.9948
Hybrid GA	1.0000	8.0656e-06	1.5115e-04
Hybrid PSO	1.0000	3.6982e-06	8.5285e-05

Table-5.1: Values of various parameters such as correlation, MSE etc. achieved by different recovery algorithms

The direct application of hybrid GA and PSO to recover biomedical images is computationally inefficient because of the large dimensions of the problem. An initial population of 20 particles or chromosomes mean that these algorithms will start with 20 different biomedical images requiring lot of memory and computation power. All these images will need to undergo velocity and position updates in case of PSO. Similarly applying GA means that mutation and crossover will be applied to generate offsprings. However, some of the ideas of heuristic algorithms can be incorporated in iterative shrinkage algorithms to reconstruct biomedical images.

5.4 Proposed modified POCS algorithm for biomedical images

This section presents a novel CS reconstruction method for Fourier encoded images. It is based on POCS algorithm but it takes two images and then randomly combines them at each iteration to estimate the original MR image. Like POCS algorithm, the proposed technique iterates between soft-thresholding in the sparsifying domain with data consistency constraint in the frequency domain. Similarly, like GA it uses a random combination of the previous (two) estimates to reduce the mean square error of the reconstructed (offspring) image. During each iteration, the candidate solution is

updated based on the fitness (i.e. MSE) values. The detail description of the proposed algorithm is shown in Fig-5.8. The algorithm can be used to recover compressively sampled Fourier encoded images.

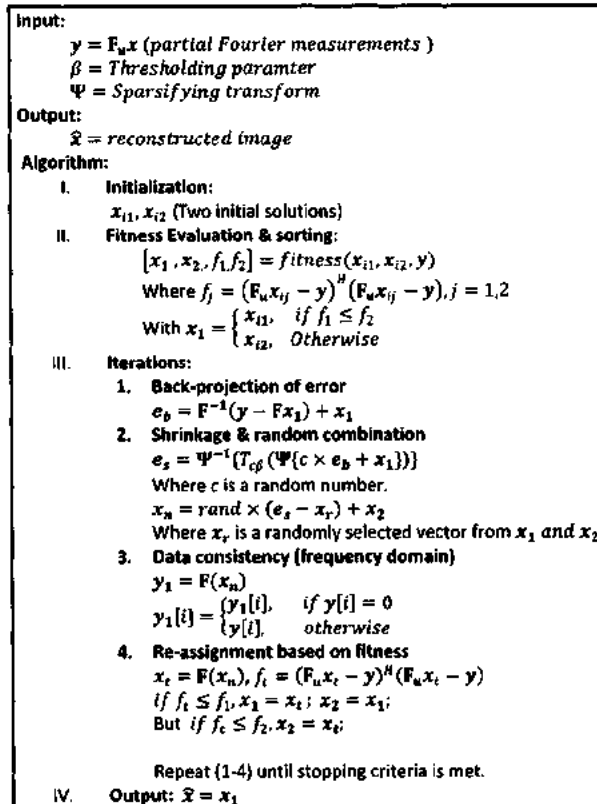


Figure-5.8: Modified POCS based algorithm for CS recovery

For the purpose of demonstration, the proposed modified POCS algorithm is applied to recover the original MR image from variable density undersampling scheme. The algorithm is initialized with two images (x_{i1} and x_{i2}) that are directly reconstructed from the undersampled data using zero filling with and without density compensation. During the first iteration, the two images are combined together to compute a new estimate. In the remaining iterations, the algorithm is used to consider two best (on the

basis of fitness value) out of the three images to refine the estimated image. The final reconstructed image is shown in Fig-5.9. The Daubechies D4 Wavelet is used as sparsifying transform (Ψ) with scaling coefficients:

$$h = \{0.4830, 0.8365, 0.2241, -0.1294\}.$$

Fig-5.10 shows the comparison of POCS and SSF based reconstruction methods with the proposed algorithm. For the same number of iterations, the proposed algorithm achieves better value of fitness value (i.e. MSE) indicating that it outperforms SSF and POCS based recovery techniques.

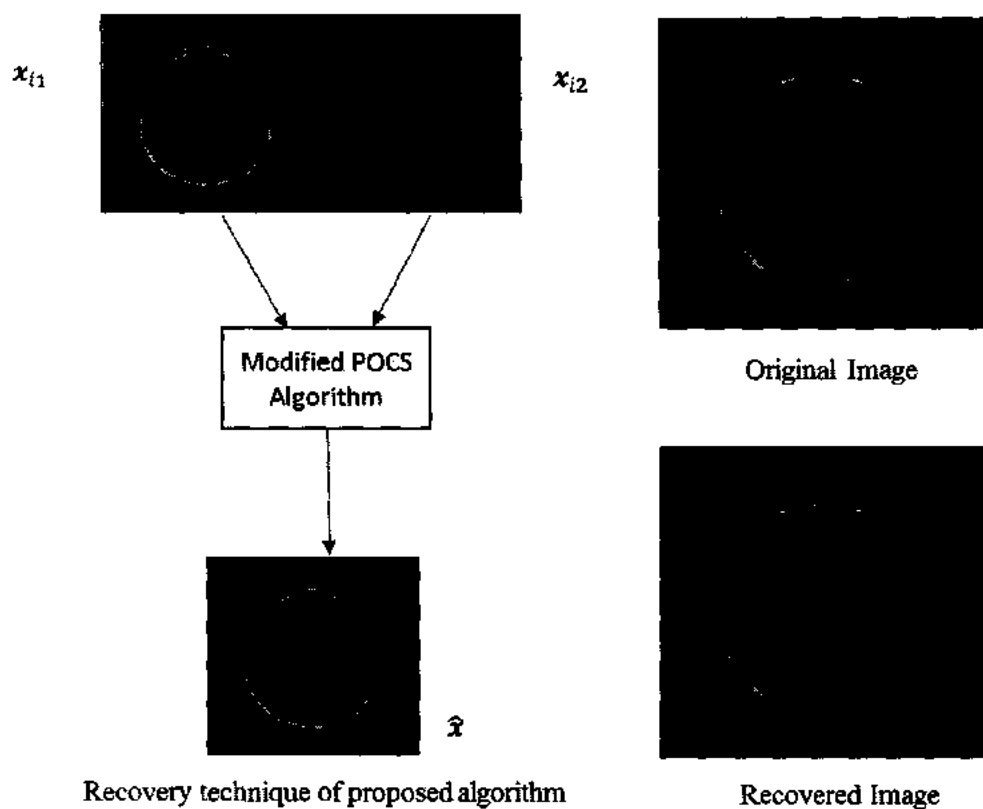


Figure-5.9: Final image recovery with modified POCS algorithm

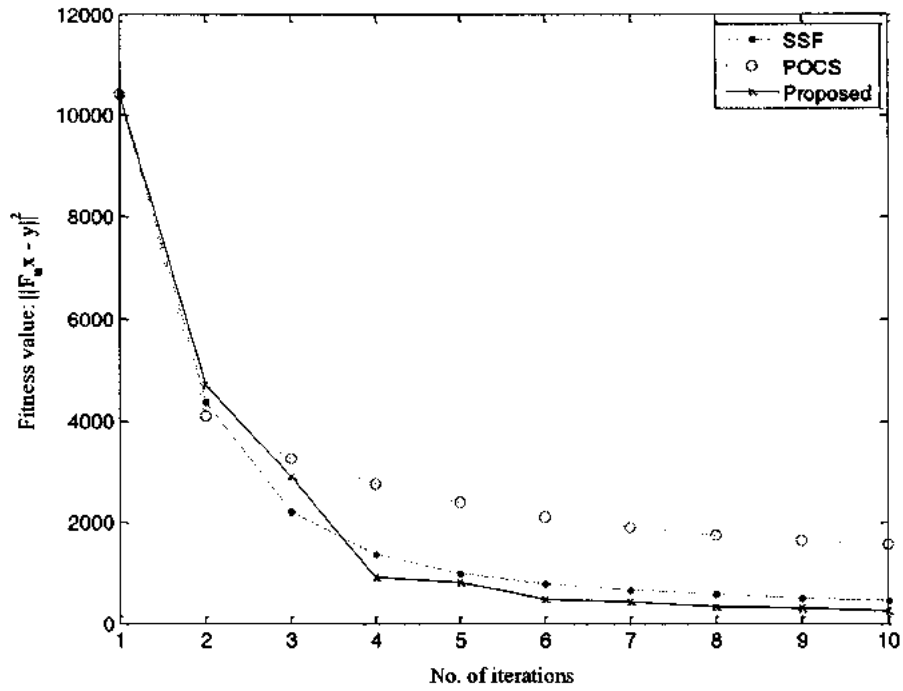


Figure-5.10: Comparison of proposed algorithm with POCS and SSF

Table-5.2 shows the summary of the various performance metrics achieved by applying different recovery techniques to the same undersampled MR image. The algorithm can be applied to recover other Fourier encoded images including parallel beam CT and MWI.

	PSNR	Artifact power	Correlation
LR	8.6419	0.0062	0.9796
POCS	16.3936	0.0047	0.9965
SSF	20.9532	0.0022	0.9982
x_{i1}	8.9166	0.0325	0.9818
x_{i2}	6.7314	0.0538	0.9753
Proposed	21.422	0.0021	0.9988

Table-5.2: Comparison of algorithms for MR image reconstruction

5.6 Summary

Solving the NP-hard l_0 -minimization problem with the conventional PSO and genetic algorithms has the issue of slow convergence. Using the sparsity-constrained version of PSO and GA along with SSF not only accelerates the convergence but also precisely recover the support of the original sparse signal. The proposed hybrid combination is able to reconstruct the target (1-D) signal faithfully from less number of non-adaptive Gaussian projections. Based on the idea of GA, a modified POCS based algorithm is presented for the recovery of Fourier encoded imaging. MRI related experiments show that the novel algorithm performs better than the POCS and SSF based recovery techniques.

CHAPTER-6

CS RECOVERY BASED ON SMOOTH l_1 -NORM APPROXIMATION

Sparse signal reconstruction methods are used in a wide range of applications such as compressive sensing, denoising, signal separation and general linear inverse problems. The numerical algorithms used for the sparse signal recovery frequently involve finding solution to the least squares optimization problem with l_1 -norm regularization. As the l_1 -norm penalty is not differentiable, so it rules out the possibility of using the efficient optimization techniques that call for the derivative of the objective function. This chapter presents a hyperbolic tangent based surrogate function to closely approximate the l_1 -norm regularization. Simultaneously, an iterative algorithm is developed for sparse signal reconstruction that utilizes the gradient of the proposed smooth function. The algorithm can be used to recover the compressively sampled (1-D) signals as well as images from a reduced set of measurements. Various numerical and imaging experiments are used to illustrate the performance of the promising recovery method. It has been shown that the algorithm can be applied to reconstruct the compressively sampled Fourier encoded images from less number of acquired data, which makes fast imaging possible without compromising high spatial resolutions.

6.1 Problem Statement

It is a well-known fact that most of the efficient unconstrained optimization techniques such as method of steepest descent, Gauss-Newton method and least-mean-square (LMS) algorithm need the gradient of the cost function to obtain the optimum solution [115-117]. However, we cannot directly use these methods to minimize the objective

function of problem (4.1) which involves expression of the form $\sum_{i=1}^n |x_i|$. The function $f(x) = |x|$ is continuous but not smooth everywhere, since it has kink at $x = 0$ and is not differentiable [118,119]. Differentiability is also an essential requirement for the non-linear activation function used to model a neuron in a neural network [120,121]. It is, therefore, necessary to use a smooth surrogate function to approximate $|x|$.

6.2 Proposed hyperbolic Tangent based surrogate function

We propose a hyperbolic tangent based surrogate function that can be used to closely approximate $|x|$.

The hyperbolic tangent is an odd, non-convex, smooth and strictly increasing analytical bounded function. For the general case of $y = z(x) = c \tanh(\gamma x)$, the slope of the function at the origin can be adjusted to any desired value with proper selection of the parameters c and γ i.e.:

$$y' = \frac{\gamma}{c} (c - y)(c + y), \text{ with } y'(0) = \gamma c \quad (6.1)$$

For the aforementioned general case, the inverse output-input relation can be expressed as:

$$x = z^{-1}(y) = -\frac{1}{2\gamma} (\log_e(c + y) - \log_e(c - y)) \quad (6.2)$$

The role of hyperbolic tangent to approximate various functions is not uncommon in the field of signal processing and neural networks [121,122]. It can be used to approximate the signum (discontinuous) function, which is widely used for hard thresholding:

$$\text{sig}(x) = \begin{cases} -1, & \text{if } x < 0 \\ +1, & \text{if } x > 0 \end{cases} \cong \tanh(\gamma x), \gamma \gg 1 \quad (6.3)$$

In neural networks, hyperbolic tangent function is used for non-linear mapping because of its “S-shaped” curve. It performs better than other sigmoid activation functions with respect to computability, training times etc. and therefore plays a vital role in the backpropagation and Hopfield networks. The hyperbolic tangent is essentially equivalent to the logistic sigmoid function in that, one can be expressed in terms of the other, by scaling and translation transformation [121,123,124].

$$\frac{1}{1+e^{-x}} - \frac{1}{2} = \frac{1}{2} \tanh\left(\frac{x}{2}\right) \quad (6.4)$$

Recently, the hyperbolic tangent function has been used in the application of sparse signal processing to approximate the l_0 norm [125, 126]. The proposed smooth approximation is shown to perform better than the Gaussian and inverse tangent function based approximations.

The facts that the hyperbolic tangent function has adjustable slope at the origin and is bounded by the line $y = \pm 1$, make it suitable surrogate function for the l_1 norm. We use it to approximate the non-differentiable function $|x|$ that is used to compute the l_1 norm i.e.:

$$|x| \approx xz(x) = cx \tanh(\gamma x) \quad [6.5]$$

Fig-6.1 shows the comparison of approximations for $c = 1$ and $\gamma = 1,2,4$. It is clear that larger γ provides a close estimate of the function.

From Eq-6.3 and Eq-6.5, it is clear that for $c = 1$ and $\gamma \gg 1$, the approximation error is negligible for larger values of x . Fig-6.2 shows the plot of mean-square-error of the proposed approximation, with respect to various selections of γ , using three different bounds of x . These results show that, for better approximation, the appropriate value of the parameter γ depends on range (magnitude values) the signal x . A signal with smaller values requires large value of γ for better approximation near the origin. It is

also worth mention that the function $f(x) = x \tanh(x)$ is convex in the interval $x \in [1, -1]$.

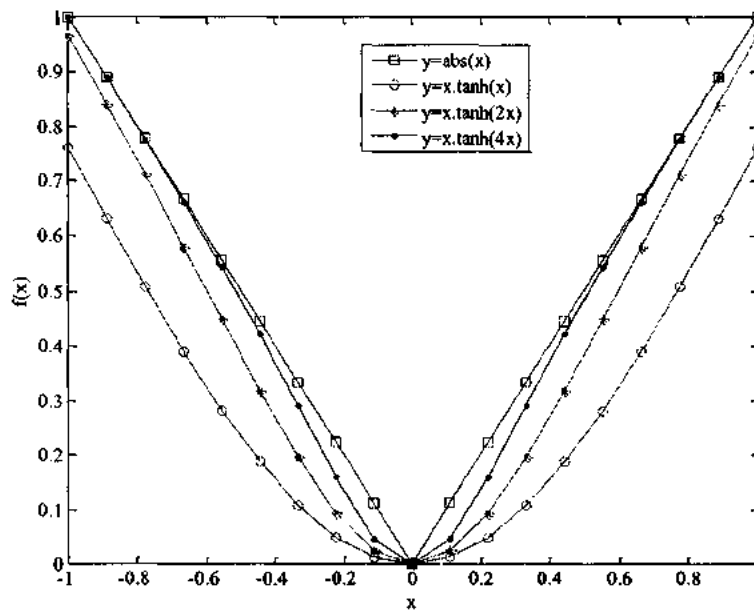


Figure-6.1 Comparison of approximation for different values of γ

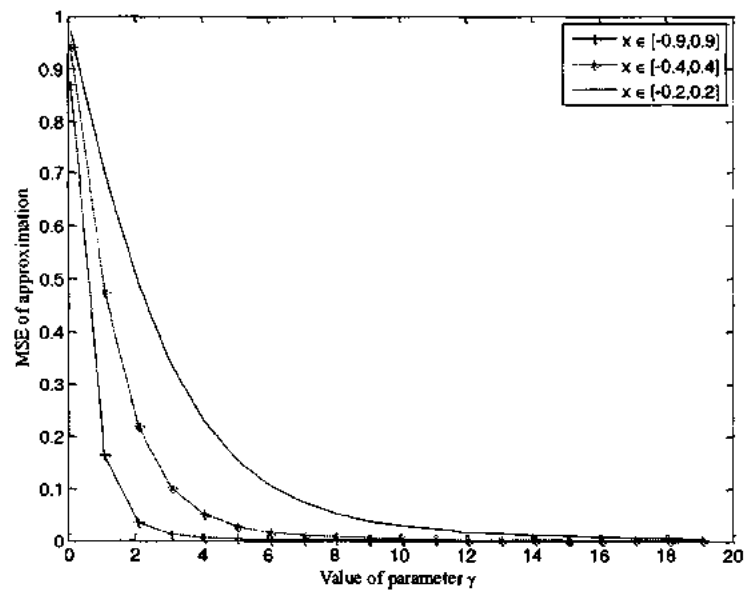


Figure-6.2 Mean-square error of the approximation for different bounds of signal

6.3 Proposed Recovery Algorithm

For the scalar case of problem (4.1), the proposed approximation leads to the following minimization problem:

$$T_\beta(y) := \arg \min_x f(x) = \operatorname{argmin}_x \left\{ \frac{1}{2} (y - x)^2 + \beta (x \tanh(\gamma x)) \right\} \quad (6.6)$$

where $x, y, T_\beta(y) \in \mathbb{R}$. The solution $T_\beta(y)$ of problem (6.6) depends on the value of y and the Lagrangian multiplier β .

Differentiating $f(x)$, equating to zero and solving for y yields:

$$\begin{aligned} y &= x + \beta [\gamma x (1 - \tanh^2(\gamma x)) + \tanh(\gamma x)] \\ &\cong x + \beta \tanh(\gamma x), \quad |\gamma x| \gg 1 \end{aligned} \quad (6.7)$$

A closed form mathematical equation for $T_\beta(y)$ cannot be obtained by solving the non-linear Eq-6.7. However, it can be solved either graphically or using the approximation of Eq-6.3. Solving Eq-6.7 graphically is shown in Fig-6.3, where the solution $T_\beta(y)$ in Fig-6.3b is obtained by exchanging the axes of Fig-6.3a. Using the approximation of Eq-6.3 leads to the following closed form solution:

$$T_\beta(y) \cong \begin{cases} y - \beta, & y > \beta \\ y + \beta, & y < -\beta \\ 0, & \text{Otherwise} \end{cases} \quad (6.8)$$

The update equation for the iterative form of the algorithm is derived by using the classical steepest descent method:

$$\mathbf{x}_{k+1} = \mathbf{x}_k - \eta \nabla f(\mathbf{x}_k) \quad (6.9)$$

where η is a positive constant called the stepsize or learning rate. $\nabla f(\mathbf{x}_k)$ represents the gradient operator of the cost function at the k -th iteration. Assuming $z(x_i) = c x_i \tanh(\gamma x_i)$, the cost function is

$$f(\mathbf{x}) = \frac{1}{2} \|\Phi \mathbf{x} - \mathbf{y}\|_2^2 + \beta \sum_{i=1}^n z(x_i) \quad (6.10)$$

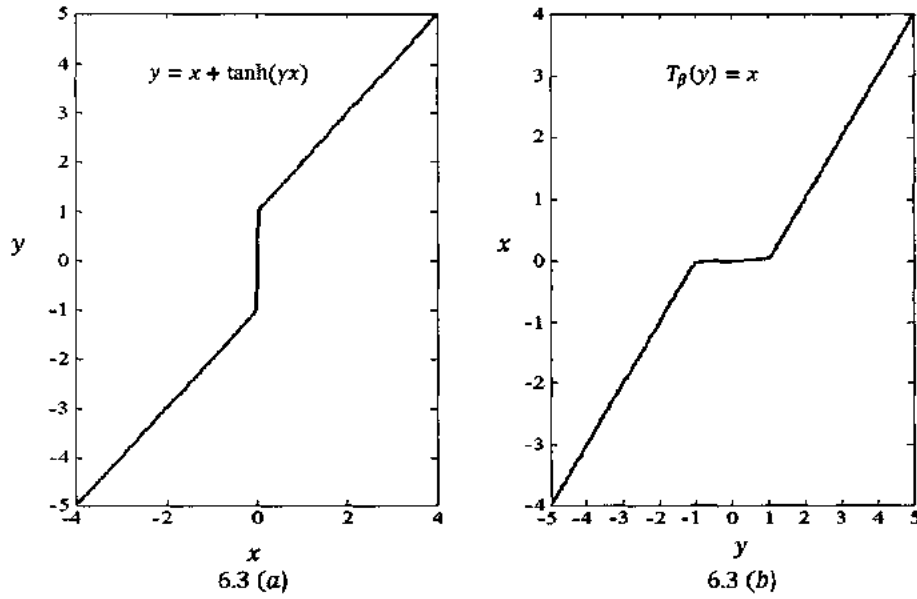


Figure-6.3: Graphical solution to Eq-6.7 corresponding to $\gamma = 50$.

The gradient of the cost function is easy to compute:

$$\nabla f(\mathbf{x}) = \Phi^T(\Phi \mathbf{x} - \mathbf{y}) + \beta \sum_{j=1}^n z'(x_j) \quad (6.11)$$

where for $\alpha_i = c \tanh(\gamma x_i)$,

$$z'(x_i) = \frac{\gamma}{c} x_i (c - \alpha_i)(c + \alpha_i) + \alpha_i \quad (6.12)$$

The complete description of the proposed iterative recovery algorithm is shown in Fig-6.4. The algorithm is initialized by using the minimum l_2 norm solution i.e. $\mathbf{x}_0 = \Phi^T(\Phi \Phi^T) \mathbf{y}$.

The stepsize can be set empirically or can be adaptively computed using the well-known Barzilai and Borwein method [127]. As the proposed algorithm is based on the standard gradient-descent method using smooth regularization penalty, its convergence can be followed directly in the optimization literature.

Input: Sensing matrix $\Phi \in R^{m \times n}$, measurement vector $y \in R^m$, parameters γ, β, η and sparsity level $k = \|x\|_0$ (optional),

Output: A k -sparse vector $\hat{x} \in R^n$

Initialization: Select x_0 according to Eq.[12], index $i=0$

Step-1 (Gradient Computation): Find $\nabla f(x_i)$ using Eqs-6.11 & 6.12

Step-2 (Solution Update): Compute x_{i+1} using Eq-6.9

Step-3 (Shrinkage): Estimate Solution using (6.8) i.e. $\hat{x}_i = T_\beta(x_{i+1})$

Step-4 (Optional): Incorporate Sparsity, $\hat{x}_i = [\hat{x}_i]_k$

where the operator $[x]_k$ sets all except the k largest elements of vector x to zero

Step-5 (Repeat): If stopping criterion is not met, $i=i+1$ and go to step-1

Output: $\hat{x} = \hat{x}_i$

Figure-6.4: Proposed hyperbolic tangent based iterative algorithm for (1-D) sparse recovery

The algorithm works well even if the sparsity of the signal is not known. However, the prior knowledge about the sparsity can greatly reduce the number of iterations by using the optional (step-4) of the algorithm. In order to use the proposed algorithm for the recovery of compressively sampled biomedical images such as MRI and microwave imaging, we also need to take the data consistency constraint into the consideration.

The algorithm can be halted either after a fixed number of iterations or when the MSE of the estimated signal $\|\Phi\hat{x} - y\|_2^2$ reaches an acceptable limit.

6.4 Results of Simulation with Discussions

In order to validate and evaluate the performance of the proposed algorithm, it is applied to reconstruct 1-D sparse signal followed by CS recovery of biomedical images.

6.4.1 Sparse Signal Recovery (1-D)

In the first experiment, we generate a one dimensional sparse signal $x \in \mathbb{R}^{512}$ having sparsity level $k = \|x\|_0 = 85$. The non-zero elements of the signal are randomly distributed at various locations. The signal is sampled using a random Gaussian matrix $\Phi \in \mathbb{R}^{256 \times 512}$ to obtain linear measurements. The values of several necessary parameters for the recovery algorithm are set as follows: $\eta = 0.9, \lambda = 0.01, \gamma \geq 10$. The proposed algorithm takes the measurement vector $y = \Phi x \in \mathbb{R}^{256}$ and estimates the locations and values of the non-zero entries in the original signal.

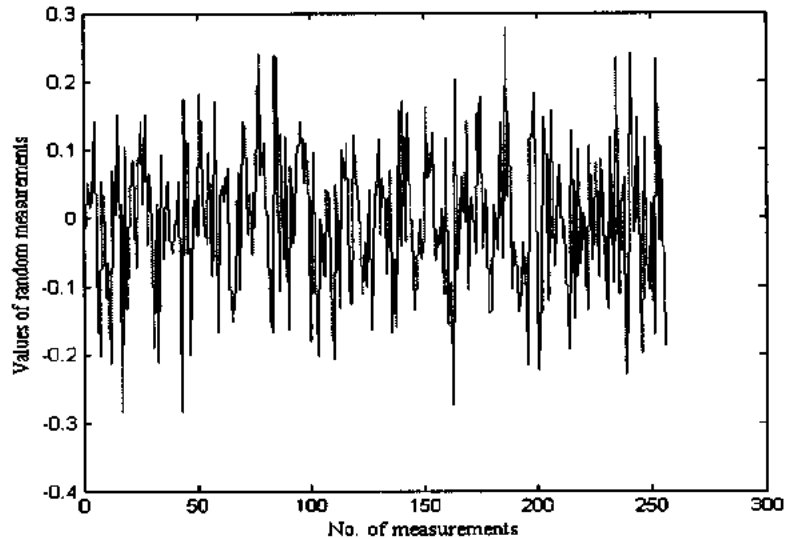


Figure-6.5: Compressively sampled sparse signal

Fig-6.5 shows the random measurements obtained after sub-sampling the original signal. We take only 50% random projections as compared to the dimensionality of the original signal. Fig-6.6 shows the recovery of the signal using the minimum norm solution and the proposed algorithm. It is clear that the proposed recovery method is

able to reconstruct the original signal almost perfectly from the sub-sampled signal of Fig-6.5. The hyperbolic tangent based L_1 -norm approximation can also be used to recover the signal even if the level of sparsity is not known in advance. However, the algorithm takes more iterations to converge. Fig-6.7 shows the comparison of signal recovery using the proposed algorithm with and without the knowledge of sparsity.

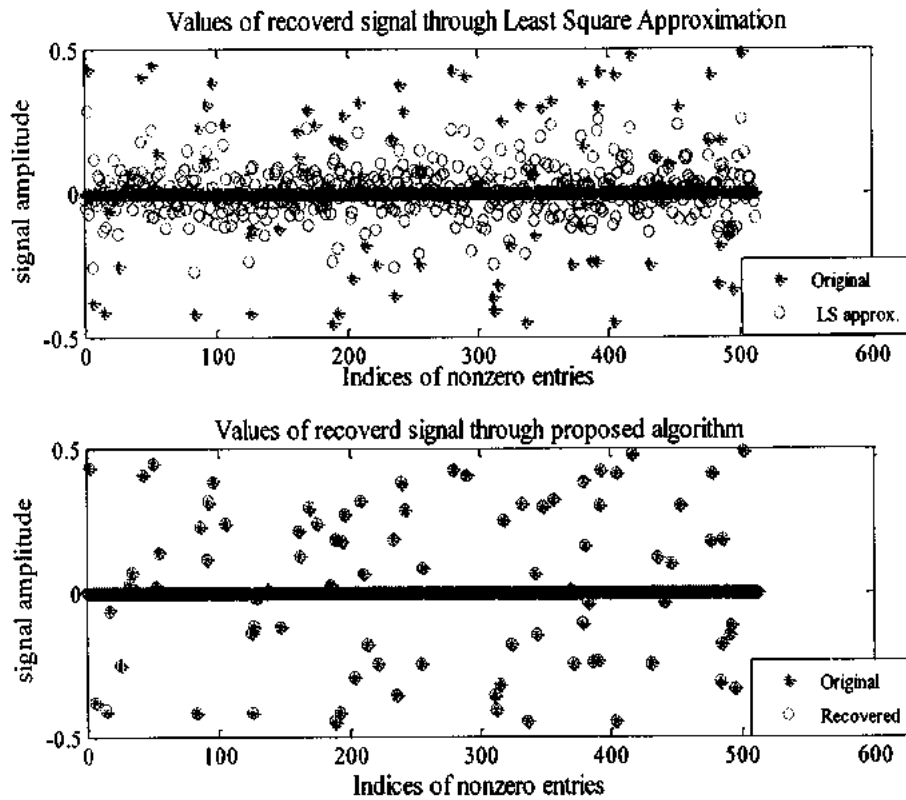


Figure-6.6: Recovery with the proposed reconstruction algorithm

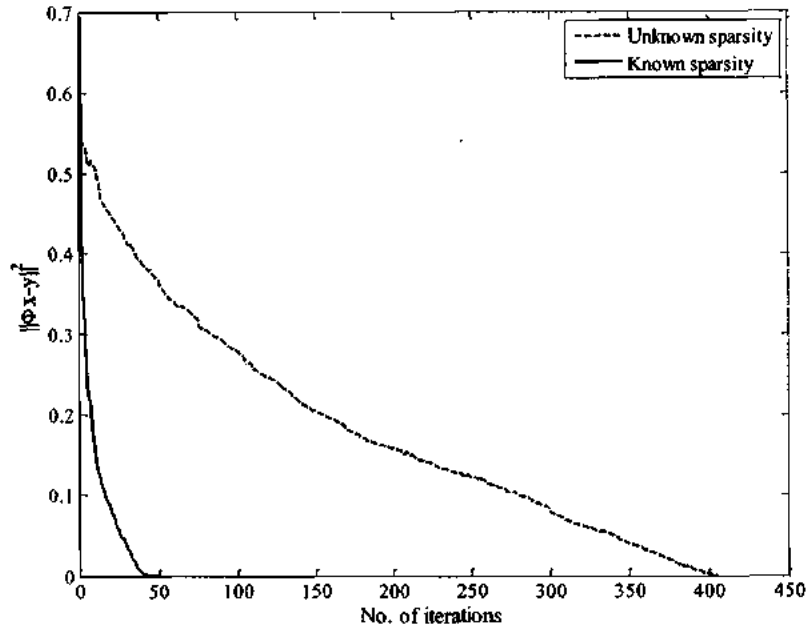


Figure-6.7: Signal recovery with and without knowledge of sparsity

6.4.2 CS recovery of biomedical images

As biomedical images are generally considered to be sparse in the transformed domain (such as DCT and Wavelet), so the non-linear shrinkage function of Fig-6.3 is applied to the entries of the estimated images in the sparsifying domain. Additionally, the algorithm incorporates the data-consistency in the Fourier domain and only estimates the missing Fourier samples. The already acquired Fourier samples remain unaltered during each iteration. The detailed description of the proposed algorithm for the CS reconstruction of biomedical images is shown in Fig-6.8.

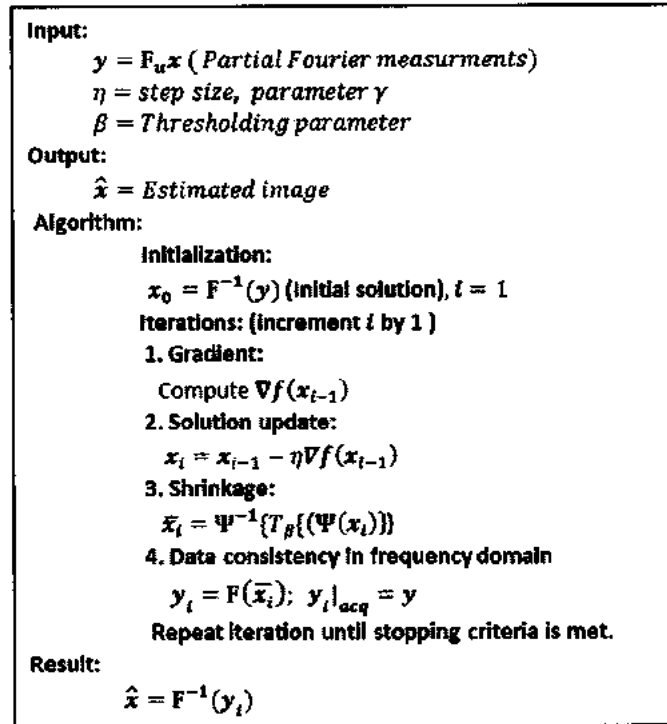


Figure-6.8: Proposed hyperbolic tangent based algorithm for CS recovery of Fourier encoded imaging

6.4.1 Experimental results with 2-D imaging

In order to further validate the performance, we apply the proposed algorithm to recover the parallel-beam CT, MR and microwave images from partial Fourier data. All the images are compressively sampled in the frequency domain (k -space for MRI) by skipping 20% of their frequency data points. Different sampling patterns are used to check the robustness of the proposed recovery algorithm. The algorithm is then run for 15 iterations to recover the images. The various necessary parameters needed for the algorithm are set as: $\gamma = 50$, $\lambda = 0.02$ and $\eta = 0.9$.

Fig-6.9 shows a 512×512 Shepp-Logan phantom that has been undersampled using radial sampling. The proposed algorithm is applied to reconstruct the original image. The recovered parallel-beam CT image along with the undersampled version are shown in Fig-6.10.

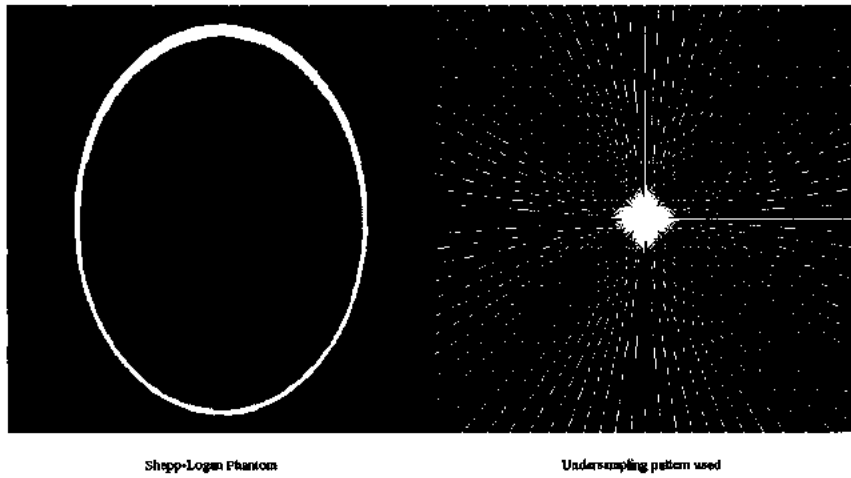


Figure-6.9: Phantom image and the under-sampling pattern used

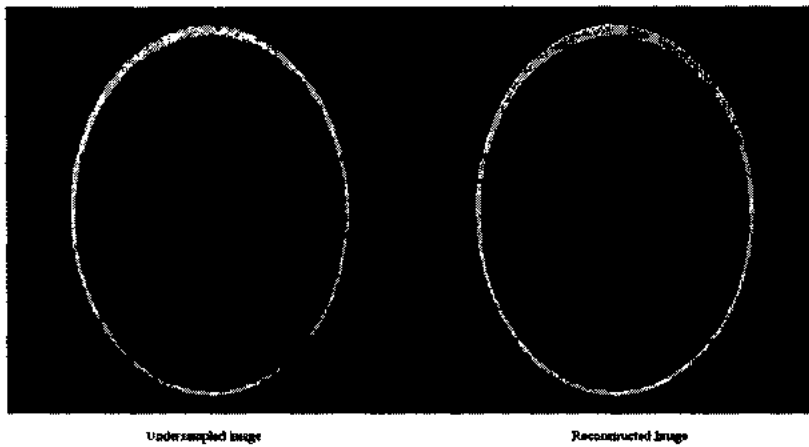


Figure-6.10: Recovery of phantom image (parallel-beam CT) with proposed algorithm

For the recovery of MR images, the original human brain MR image obtained from 1.5 Tesla GE HDxt scanner is used for the recovery. The image is undersampled using a variable density pattern. The original MR image and the corresponding variable density sampling pattern are shown in Fig-6.11, while Fig-6.12 depicts the undersampled and the reconstructed images. It is clear that the proposed algorithm can accurately reconstruct the compressively sampled MR images from the reduced data set of k -space samples.

Standard metrics such as structural similarity index (SSIM), correlation, artifact power (AP), improved signal-to-noise ratio etc. are used to evaluate the performance of the proposed algorithm for MR images [22,23]. Fig-6.13 shows the improvement in SSIM during the recovery process for both the original and phantom MR images.

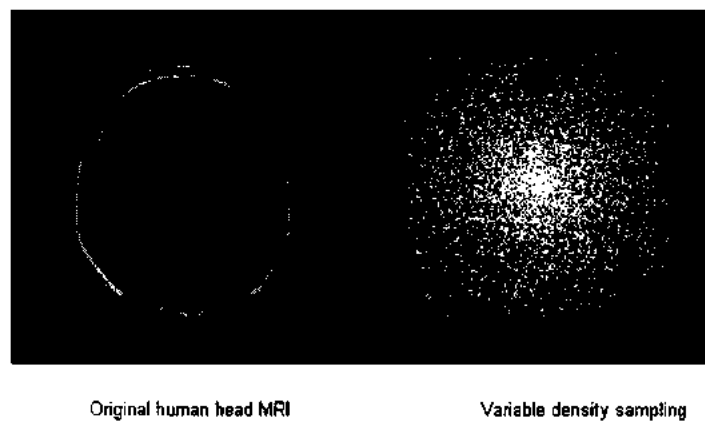


Figure:-6.11: Original human head MR image and the corresponding sampling pattern

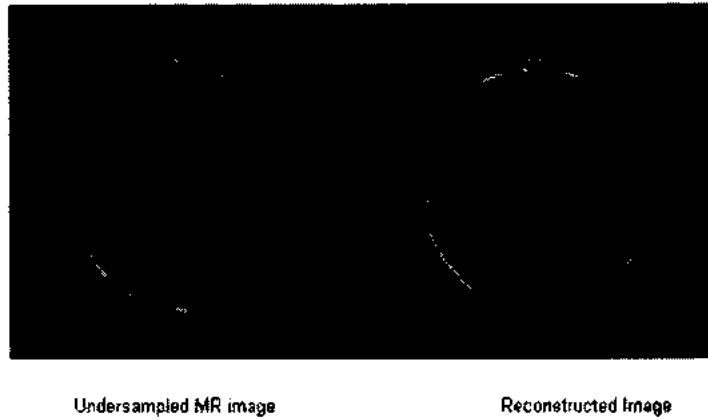


Figure-6.12: Recovery of original MR image using proposed algorithm

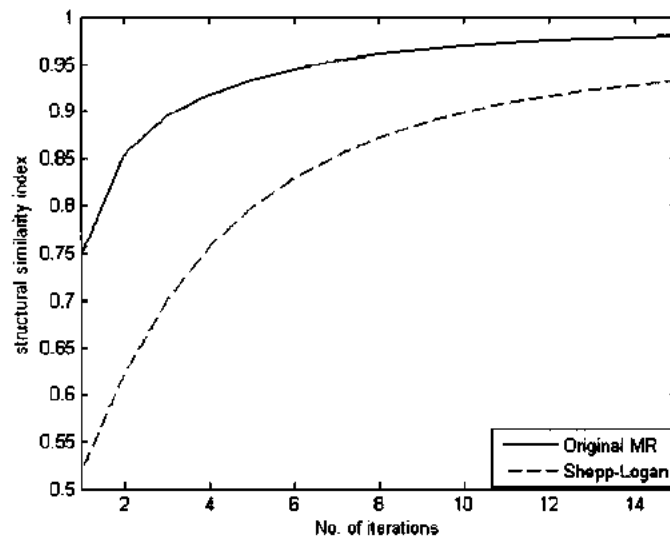


Figure-6.13: SSIM improvement of the reconstruction images in each iteration

The CS based near field microwave imaging experiment was performed in our group at the Electromagnetic and Acoustic Imaging and prognostics (LEAP) lab of the University of Colorado Denver and Anschutz Medical Campus by acquiring a 6×1.5 inches microwave backscattering image using raster scanning for a sample under-test (SUT), shown in Fig-6.14. The SUT is compressively undersampled using a

random sampling mask shown in Fig-13 during DAQ phase. Here DCT is used as a sparsifying transform. The rest of the parameters for the reconstruction algorithm are the same as those used for MR image recovery problem. The proposed algorithm is applied to recover the original microwave image from the under sampled image which is illustrated in Fig-6.15.

Finally, table-6.1 provides the numerical values of the various performance metrics such as AP, SSIM and ISNR etc. for the final images reconstructed using the proposed algorithm.

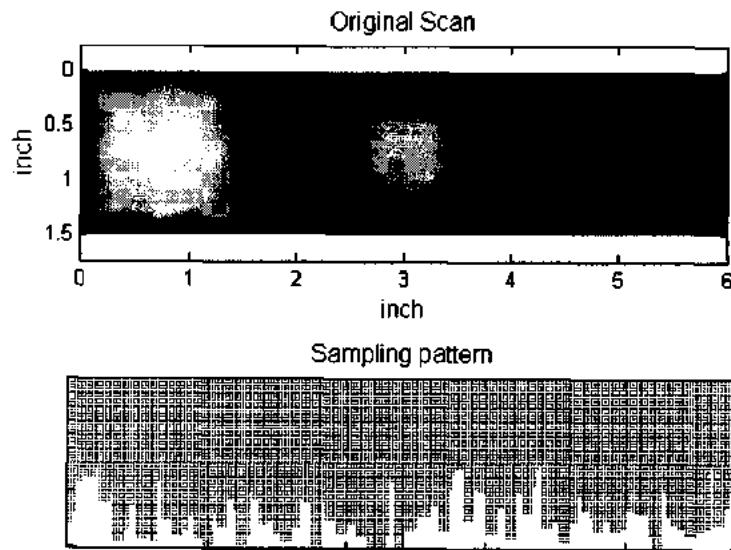


Figure-6.14: SAR image and corresponding under-sampling pattern used

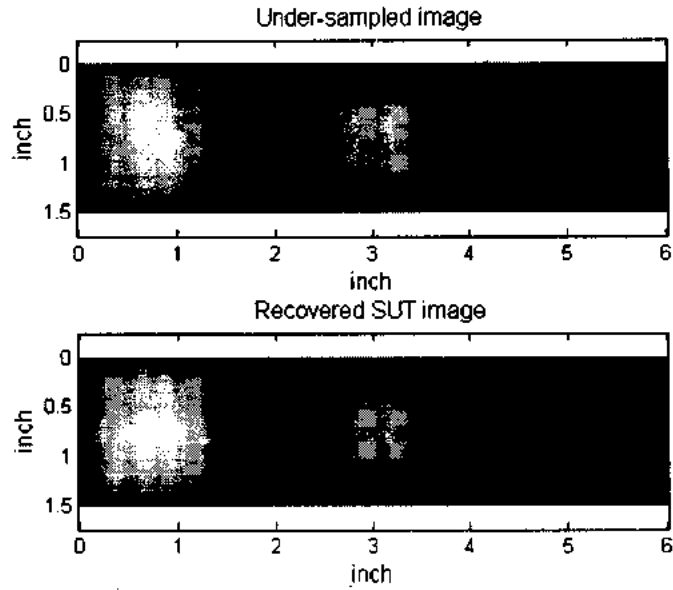


Figure-6.15: Under-sampled and recovered microwave image

	CT (Phantom Image)		Original MRI		Microwave Image	
	Under-sampled	Recovered	Under-sampled	Recovered	Under-sampled	Recovered
Correlation	0.9630	0.9973	0.9818	0.9987	0.9572	0.9978
ISNR (db)	14.0975	26.4193	16.9548	28.5396	16.8199	30.7623
SSIM	0.4193	0.9575	0.5099	0.9640	0.8131	0.9601
AP	0.0697	0.0041	0.0325	0.0021	0.0380	0.0015

Table-6.1: Comparison based on various performance metrics

6.5 Summary

In this chapter, a hyperbolic tangent based approximation for the l_1 -norm is presented. Based on the differentiable surrogate function of the l_1 penalty, a novel sparse recovery algorithm is developed. The algorithm can reconstruct a 1-D sparse signal with and without the knowledge of the sparsity of the original signal. It has been demonstrated that by incorporating the data-consistency constraint, the proposed technique can be

used to recover the compressively sampled MR and high resolution microwave images from less number of samples. The performance of the algorithm is verified by using different types of under-sampling patterns and sparsifying transforms. The proposed method has the potential to speed up the imaging acquisition while retaining the superior spatial resolutions.

CHAPTER-7

A FLEXIBLE SOFT THRESHOLDING FOR ITERATIVE SHRINKAGE ALGORITHMS

There is an equivalence between undersampling and additive Gaussian noise. In fact, CS undersampling introduces noise in the linear reconstructed images that can be modeled by the Gaussian like probability distribution function (pdf). The denoising algorithms generally require a thresholding step to set small coefficients to zero and shrink the larger coefficients towards zero. This chapter introduces a novel soft-thresholding method based on the hyperbolic tangent function. The proposed nonlinear function has adjustable parameters and can lead to various nonlinear shrinkage curves. It can be used with any iterative algorithm for denoising or equivalently CS recovery. Using the proposed thresholding function in the sparsifying domain and a data consistency step in the frequency domain, the iterative-shrinkage algorithms can be used to effectively recover the under-sampled Fourier encoded images.

7.1 CS Recovery and denoising

The elementary denoising algorithms aim to estimate a signal or image from its perturbed observations. i.e.

$$\mathbf{y} = \mathbf{x} + \mathbf{v} \quad (7.1)$$

Here $\mathbf{x} \in \mathbb{R}^n$ is the original image vector that is measured in the presence of an additive zero mean Gaussian noise \mathbf{v} having probability distribution function (pdf) given by:

$$p_{\mathbf{v}}(\theta) = \frac{1}{\sqrt{2\pi\sigma_v^2}} e^{-\frac{\|\theta\|_2^2}{2\sigma_v^2}}$$

If the image has a sparse representation in a transform domain ($x = A\alpha$), then the denoising algorithm seeks to find solution to the following optimization problem:

$$\min_{\alpha} \|\alpha\|_0 \text{ subject to } \|y - A\alpha\|_2^2 \leq \vartheta$$

The threshold ϑ is closely related to the noise power [128-131].

Assuming A to be an orthonormal basis e.g. DCT or wavelet, the solution of (7.1) can be easily obtained by simplifying the constrained term:

$$\begin{aligned} \|y - A\alpha\|_2^2 &= \|A(A^H y - \alpha)\|_2^2 \\ &= \|A^H y - \alpha\|_2^2 = \|z - \alpha\|_2^2 \end{aligned}$$

here $z = A^H y$ are the transformed domain coefficients. Incorporating the sparsity part (by applying thresholding), the following simple relationship can be used to estimate the denoised image [128,132]:

$$\hat{y} = AS_{\beta}(z) = AS_{\beta}(A^H y) = A\hat{\alpha} \quad (7.2)$$

Where the scalar β is thresholding parameter which depends on the noise power and sparsifying transform used. S_{β} is the scalar-valued hard-thresholding operator defined by:

$$S_{\beta}(z) = \begin{cases} z, & |z| \geq \beta \\ 0, & \text{Otherwise} \end{cases} \quad (7.3)$$

The step by step description of computing the denoised version of the image using wavelet transform ($A^H = \Psi$) is shown in Fig-7.1

1. **Compute transform coefficients:** $z = \Psi y$
2. **Use element-wise hard-thresholding:** $\hat{\alpha} = S_{\beta}(z) = [z]_k$
3. **Denoise image:** $\hat{y} = \Psi^{-1} \hat{\alpha}$

Figure-7.1: Transformed based image denoising

To improve the results under various assumptions, different mathematical thresholding operators have been proposed in literature [133-136]. The idea is to map the values near the origin to zero and those away from the origin are shrunk towards zero.

The random and irregular sampling at the CS encoder results in an incoherent (noise like) artifacts in the sparsifying domain. For the case of MRI or other Fourier encoded biomedical imaging ($y = F_u x$), the linear reconstruction (by simply replacing the missing Fourier data with zeros and taking inverse FFT) results in artifacts that are much like additive Gaussian noise. The actual resulting noise due to subsampling depends on the undersampling pattern used [52].

For the variable density and radial undersampling patterns, used in our experiments, the histogram of the noise (in image domain) is shown in Fig-7.2. The error is obtained by the relation:

$$\begin{aligned} e &= x - \hat{x} \\ &= x - F^H y \end{aligned} \tag{7.4}$$

In order to recover the original image, the CS decoder has to estimate the noise first. This essentially makes the CS recovery as a denoising problem. The CS reconstruction algorithm iteratively estimates the target signal from the noisy measurements.

Fig-7.3 shows the histogram of the reconstructed error after 10 iterations of the SSF algorithm when applied to the brain MR image. It can be seen that the width of the Gaussian like error has decreased significantly. The variance (width) of the distribution is the mean-square-error of the estimated vector.

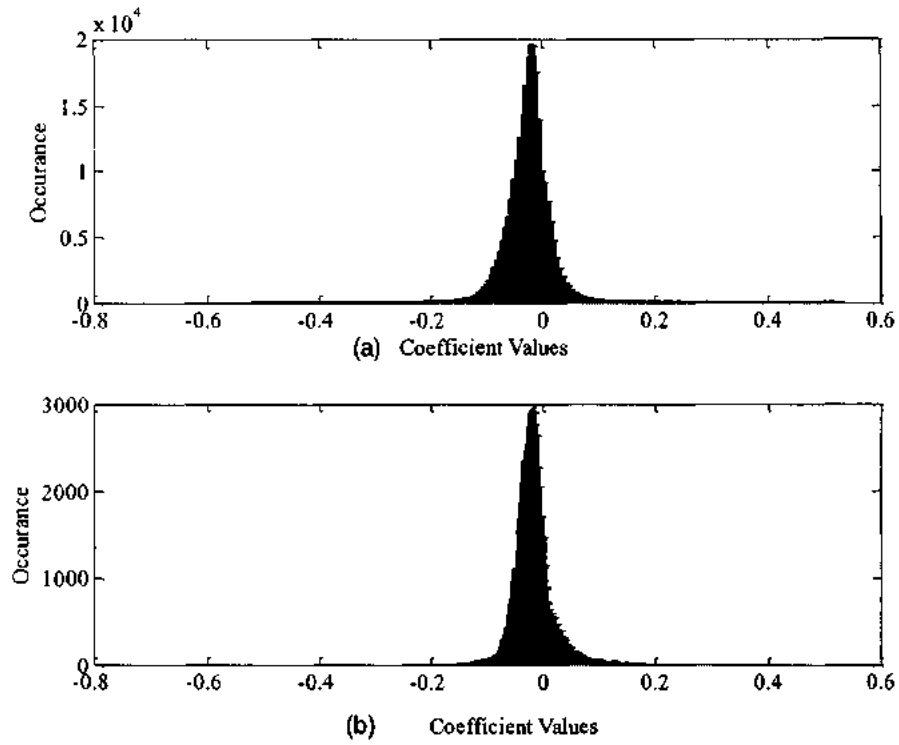


Figure-7.2: Histogram of error (between original Fourier encoded image and linear reconstructed image) for (a) parallel beam CT (b) MRI

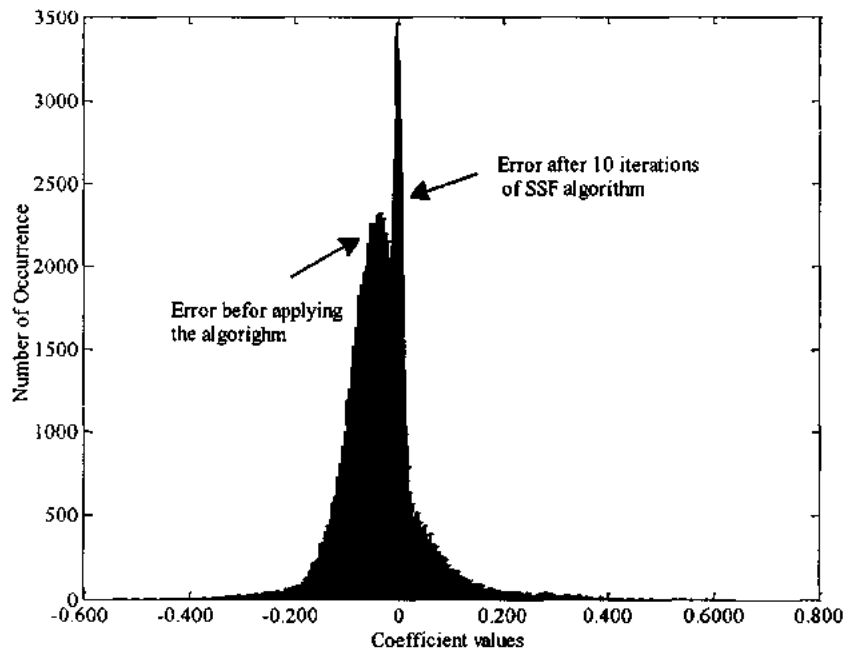


Figure-7.3: Reduction in the variance of error during CS recovery

7.2 MAP estimator for denoising and proposed thresholding

Any linear transform of the zero-mean Gaussian noise results in a zero-mean Gaussian noise in the transformed domain. So applying wavelet transform to Eq-7.1 results in:

$$\mathbf{z} = \mathbf{w} + \mathbf{v} \quad (7.5)$$

Where the random vectors $\mathbf{z} = \Psi\mathbf{y}$ and $\mathbf{w} = \Psi\mathbf{x}$ are the wavelet coefficients of the noisy observations and noise-free image respectively. The maximum a posteriori (MAP) estimator for the random vector \mathbf{w} is given by:

$$\hat{\mathbf{w}} = \operatorname{argmax}_{\mathbf{w} \in \mathbb{R}^n} p(\mathbf{w}|\mathbf{z})$$

Using Baye's rule and ignoring $P(\mathbf{z})$ as using the fact that $p(\mathbf{z})$ does not depend on \mathbf{w} , the MAP estimator takes the form:

$$\hat{\mathbf{w}} = \operatorname{argmax}_{\mathbf{w} \in \mathbb{R}^n} p(\mathbf{z}|\mathbf{w})p_{\mathbf{w}}(\mathbf{w}) \quad (7.6)$$

The problem of (7.6) can be simplified by using some simple mathematics starting with $p(\mathbf{z}|\mathbf{w}) = p_{\mathbf{v}}(\mathbf{z} - \mathbf{w})$:

$$\begin{aligned} \hat{\mathbf{w}} &= \operatorname{argmax}_{\mathbf{w}} [p_{\mathbf{v}}(\mathbf{z} - \mathbf{w})]p_{\mathbf{w}}(\mathbf{w}) \\ &= \operatorname{argmax}_{\mathbf{w}} [\ln([p_{\mathbf{v}}(\mathbf{z} - \mathbf{w}) + \ln p_{\mathbf{w}}(\mathbf{w})]) \\ &= \operatorname{argmax}_{\mathbf{w}} \left[\ln\left(\frac{1}{\sqrt{2\pi\sigma_v^2}} e^{-\frac{\|\mathbf{z}-\mathbf{w}\|_2^2}{2\sigma_v^2}}\right) + \ln p_{\mathbf{w}}(\mathbf{w}) \right] \\ &= \operatorname{argmax}_{\mathbf{w}} \left[\ln \left\{ \left(\frac{1}{\sqrt{2\pi\sigma_v^2}}\right)^n e^{-\frac{\|\mathbf{z}-\mathbf{w}\|_2^2}{2\sigma_v^2}} \right\} + \ln p_{\mathbf{w}}(\mathbf{w}) \right] \\ &= \operatorname{argmax}_{\mathbf{w}} \left[-\frac{\|\mathbf{z} - \mathbf{w}\|_2^2}{2\sigma_v^2} + f(\mathbf{w}) \right] \end{aligned} \quad (7.7)$$

Where $f(\mathbf{w}) = \ln p_{\mathbf{w}}(\mathbf{w})$. The MAP estimator for the wavelet coefficients of the original image can be obtained by differentiating the argument of (7.7) w.r.t. \mathbf{w} and equating the result to zero i.e.

$$\frac{(z_i - \hat{w}_i)}{\sigma_v^2} + f'(\hat{w}_i) = 0, \quad 1 \leq i \leq n \quad (7.8)$$

For natural and biomedical images, the pdf of wavelet domain coefficients is generally more peaked at the center than Gaussian. Assuming the distribution of transformed domain coefficients be Laplacian i.e.

$$p_w(w_i) = \frac{1}{\sqrt{2}\sigma} e^{-\frac{\sqrt{2}}{\sigma}|w_i|}$$

gives $f'(\hat{w}_i) = -\frac{\sqrt{2}}{\sigma} \text{sig}(\hat{w}_i)$. Solving Eq-7.8 results in

$$z_i = \hat{w}_i + \frac{\sqrt{2}\sigma_v^2}{\sigma} \cdot \text{sig}(\hat{w}_i) \quad (7.9)$$

Representing $\frac{\sqrt{2}\sigma_v^2}{\sigma} = \beta$ and solving Eq-7.9 for \hat{w}_i to get the nonlinear shrinkage:

$$\hat{w}_i(z) = T_\beta(z) = \max\{|z| - \beta, 0\} \cdot \text{sig}(z) \quad (7.10)$$

Eq-7.10 indicates that the Laplacian distributed wavelet coefficients of the original image can be estimated by applying the element-wise shrinkage of Eq-7.10 to wavelet coefficients of the noisy image (or compressively undersampled image in case of CS). It means that the hard-thresholding (step-2) of Fig-7.1 will be replaced by Eq-7.10.

In practice, the noise distribution may not be exactly Laplacian. So, the shrinkage function may slightly vary. We present a soft-thresholding nonlinear function based on hyperbolic tangent function that can closely approximate the operator of Eq-7.10. However, the proposed thresholding scheme is versatile and provides various adjustable parameters. The general form of the novel shrinkage operator is given by:

$$T_\beta(z) = \begin{cases} 0 & \text{if } |z| < \beta \\ cz \{ \tanh(\gamma(|z| - \beta)) \} & \text{if } |z| \geq \beta \end{cases} \quad (7.11)$$

As shown in Fig-7.4, the parameter c and γ can be tuned to get various magnitude levels and adjustable rise of the thresholding function respectively. Fig-7.4 demonstrates

another fact that Eq-7.11 can also be used to approximate Eq-7.10 very closely if $k \in [-1, +1]$ and $\beta \leq 0.2$ by taking $c = (1 - \beta)$ and fixing $\gamma = (1/\beta - 1)$. This is helpful because an image can always be normalized so that its values fall in the interval $[-1, 1]$ either in pixel domain or in a transformed domain such as Wavelet and Fourier.

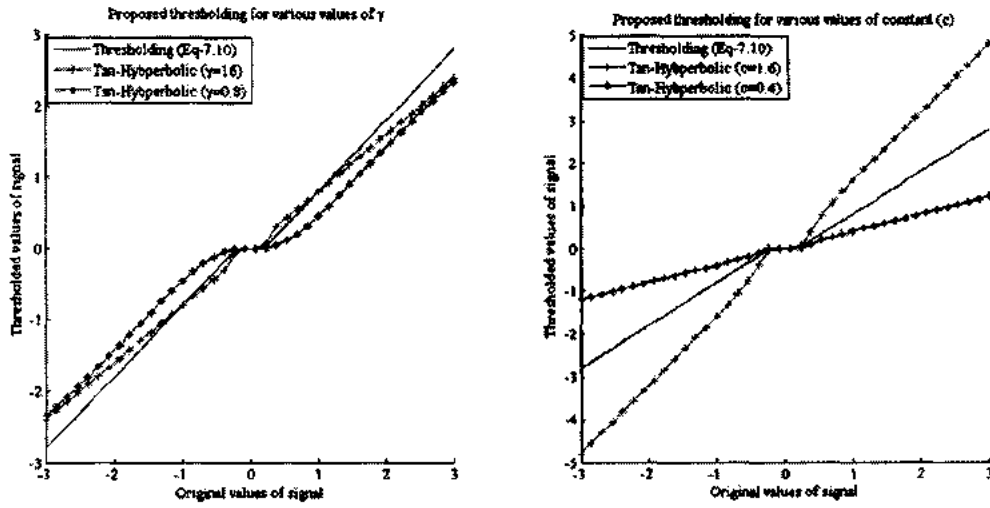


Figure-7.4: Versatility of the hyperbolic-tangent based soft-thresholding

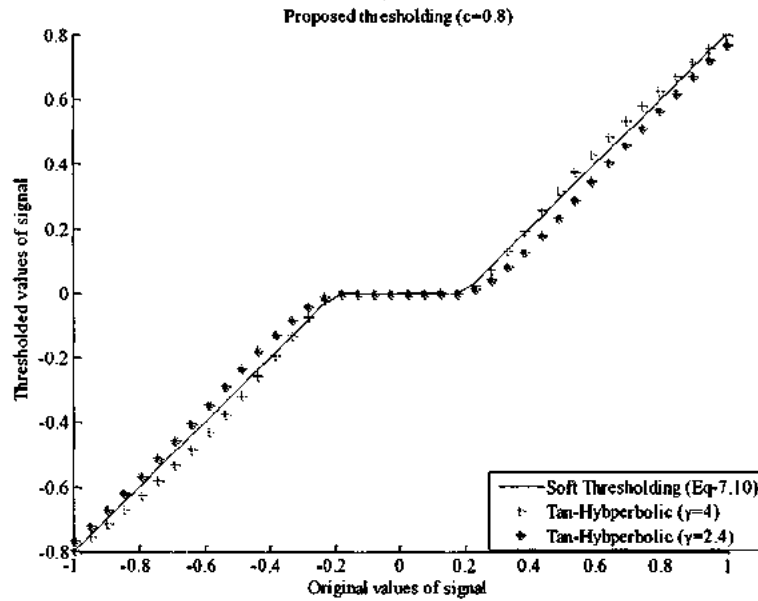


Figure-7.5: Approximation of Eq-7.10 using the proposed soft-thresholding (Eq-7.11)

The proposed thresholding function can be used with any iterative shrinkage algorithm. To show its performance, a 1-D sparse signal $x \in \mathbb{R}^{512}(k=85)$ is recovered by applying the algorithm of Fig-6.4 but replacing the original shrinkage step (Step-3) by the proposed one (Eq-7.11). Similarly the same signal is recovered with SSF using the soft-thresholding of Eq-7.10. The shrinkage is performed on the estimated signal directly as it is assumed to be sparse in the time-domain. The promising results of the proposed algorithm are clear from Fig-6.4.

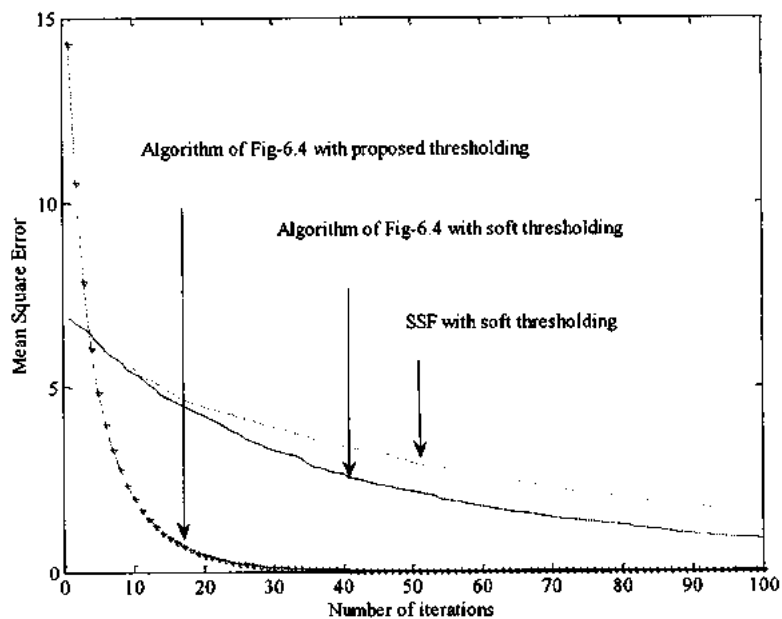


Figure-7.6: performance of the proposed thresholding function

The proposed nonlinear thresholding can be used with any iterative shrinkage algorithm to recover the compressively sampled Fourier encoded images.

7.3 CS recovery of biomedical imaging (Denoising approach)

In general, the iterative shrinkage algorithms estimate the denoised image by thresholding the wavelet coefficients i.e.

$$\hat{x}_{denoise} = \Psi^{-1}\{T_{\beta}(\Psi\hat{x})\} \quad (7.11)$$

The error between the denoised version and the original image is estimated and incorporated in the update equation. Assuming the acquisition transform to be orthonormal, the linear estimate of the error can be computed as:

$$\begin{aligned} \hat{e} &= x - \hat{x}_{denoise} \\ &= A^H(y - A\hat{x}_{denoise}) \end{aligned} \quad (7.12)$$

where $y = Ax$ are the encoded measurements of the original image vector. The solution can be refined by using the update equation that considers the denoised image and the error estimate together. In general, the update equation takes the form:

$$\hat{x} = \hat{x}_{denoise} + W\hat{e} \quad (7.13)$$

where W is the diagonal weight matrix. For SSF algorithm, $W = I$. For PCD, the weight matrix is computed offline using $W = (A^H A)^{-1}$ [56,57].

Eq-7.13 represents one iteration of the iterative shrinkage algorithms which comprises of a denoising step combined with the estimate of error.

For the Fourier encoded biomedical images, $A = F$. So at the i^{th} iteration, Eq-7.13 takes the form:

$$x_i = \Psi^{-1}\{T_{\beta}(\Psi\{W(F^{-1}(y_{i-1} - Fx_{i-1}) + x_{i-1}))\})\} \quad (7.14)$$

The thresholding parameter is usually scaled with different values that depends on the algorithm. For Fourier encoded biomedical imaging, the data consistency condition is also incorporated in the frequency domain at each iteration which means that the

originally acquired Fourier samples remain intact. The general description of CS recovery is shown in Fig-7.7

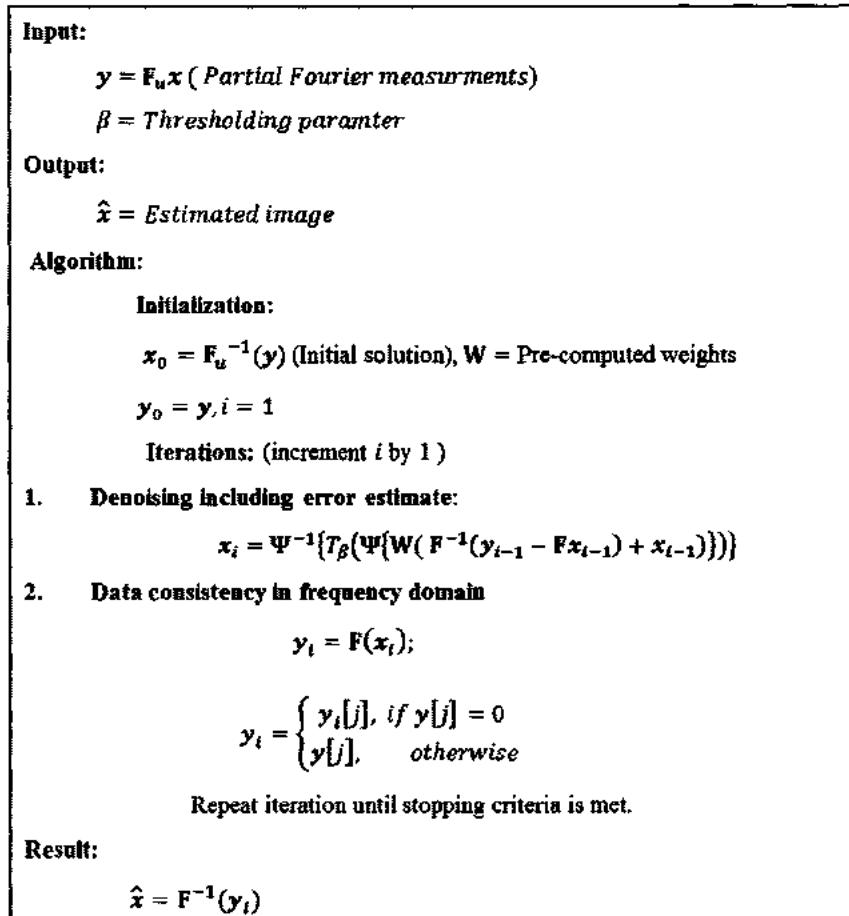


Figure-7.7: A general denoising based CS recovery algorithm

7.4 Experimental results

For the purpose of demonstration, the algorithm of Fig-7.7 is applied to recover the original MR image using variable density undersampling scheme. The weight matrix is directly computed from the undersampled image by taking the inverse of the matrix

corresponding to zero-filled reconstruction and then normalizing its value to the range $[0, 1]$. For the shrinkage, the proposed function of Eq-7.11 is applied. Fig-7.8 shows the distribution (histogram) of the original MR image in the pixel (image) domain while Fig-7.9 displays the histogram of linear reconstructed image. The algorithm runs for 10 iterations to reconstruct the original image. Each iteration comprises of linear estimate of the error, denoising and data consistency. The histogram of the recovered image is shown in figure in Fig-7.10 which is very close to that of Fig-7.8.

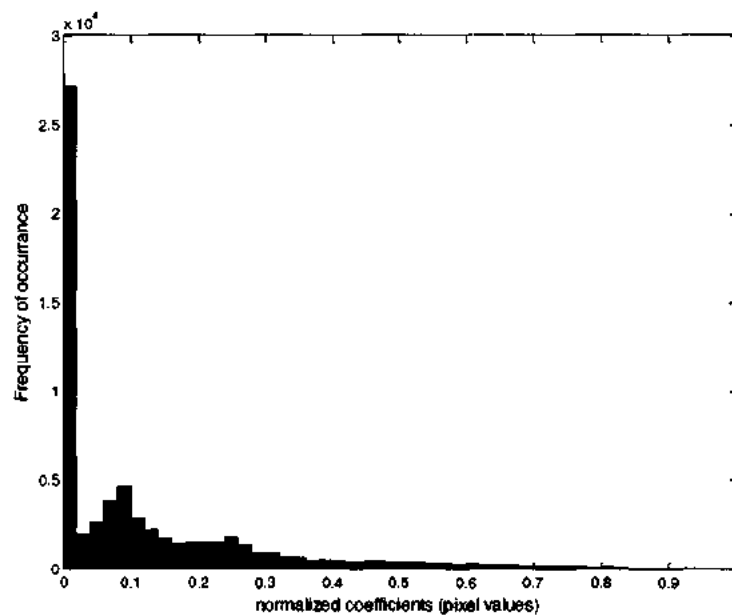


Figure-7.8: Distribution of pixel values of the original MR image

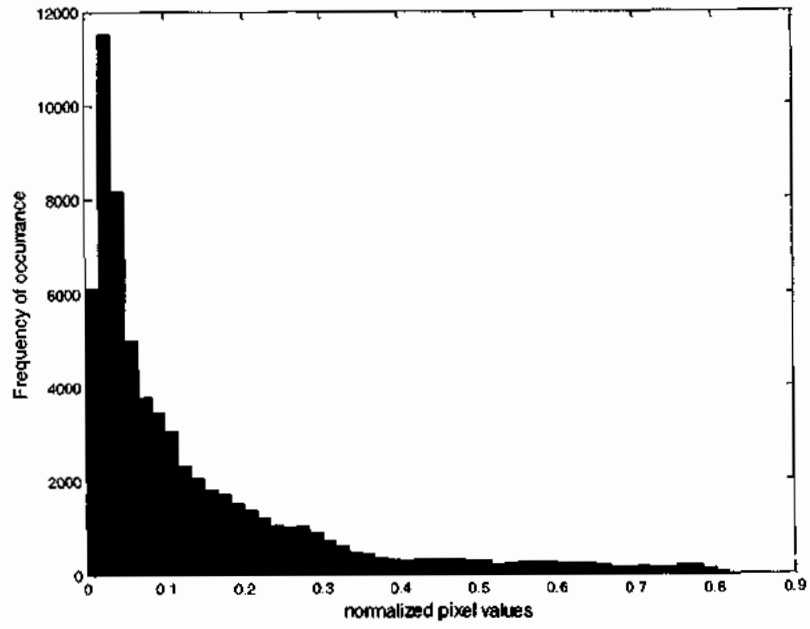


Figure-7.9: Distribution of pixel values of the original undersampled image

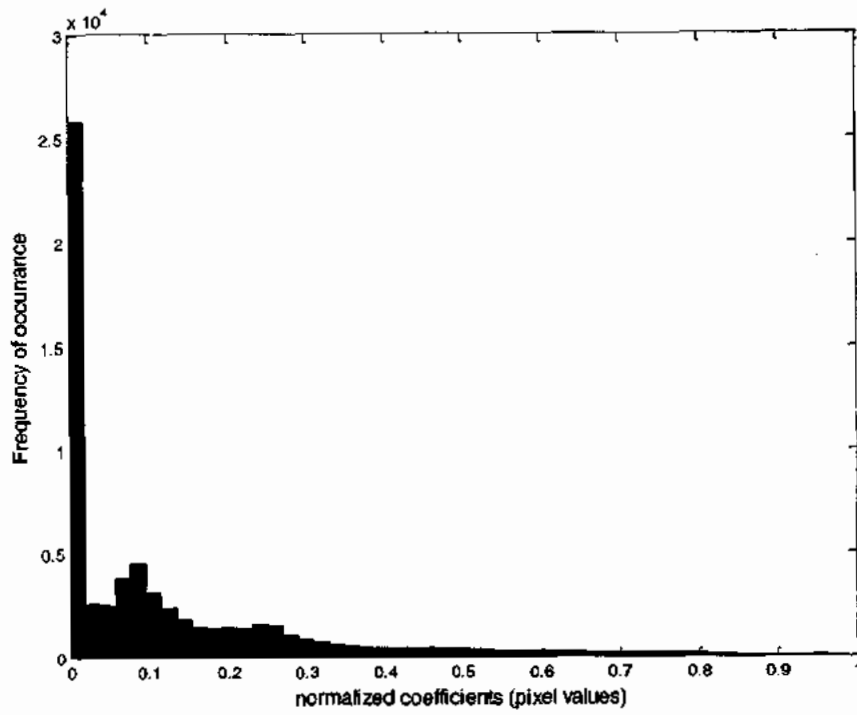


Figure-7.10: Distribution of pixel values of the reconstructed image

In the second experiment, the MR phantom image taken at St. Marry hospital London is compressively sampled and recovered through the algorithm of Fig-6.4 using (a) soft-thresholding of Eq-7.10 and (b) proposed hyperbolic soft-thresholding of Eq-7.11. The sampling pattern, number of iterations and other common parameters are kept the same to have better performance comparison. The correlation based results are shown in Fig-7.11. The original as well as recovered images are shown in Fig-7.12.

The versatility of the proposed hyperbolic tangent based soft thresholding has been validated using the SSF algorithm with both non-linear thresholding functions. Fig-7.13 depicts the improvement in SSIM achieved using the proposed nonlinear function of Eq-7.11. As shown in Fig-7.14, the image reconstructed with the proposed nonlinear shrinkage has reasonably good quality as compared to the one recovered using soft-thresholding of Eq-7.10.

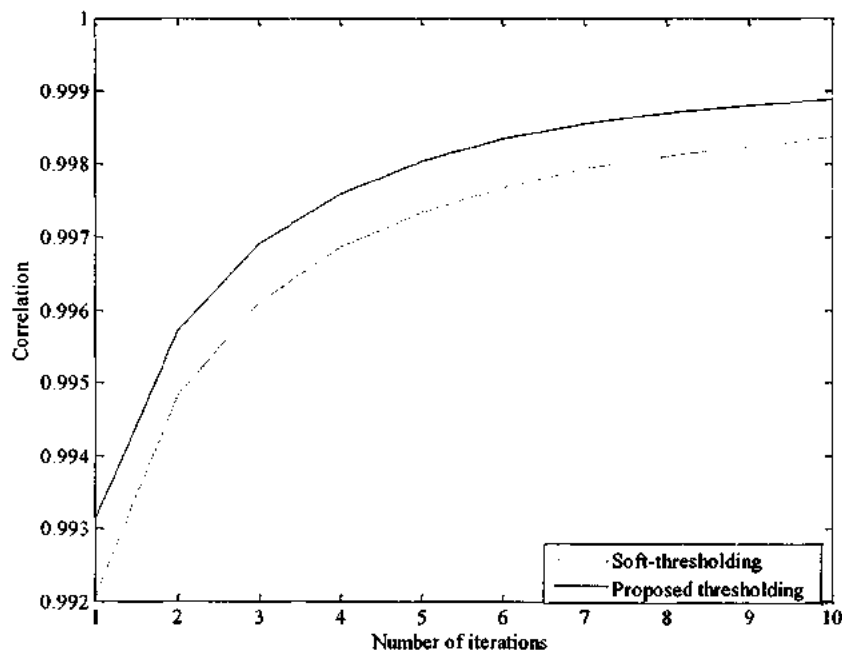


Figure-7.11: Improvement in correlation using soft (Eq-7.10) and proposed (Eq-7.11) thresholding function for MR recovery

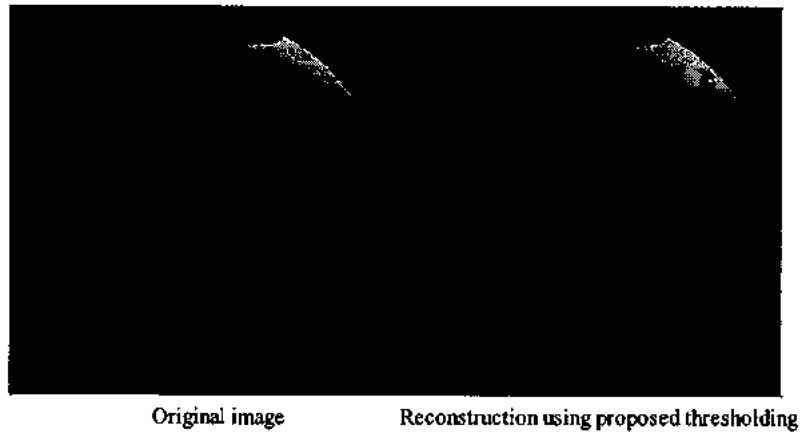


Figure-7.12: Reconstruction of MR phantom image using thresholding of Eq-7.11

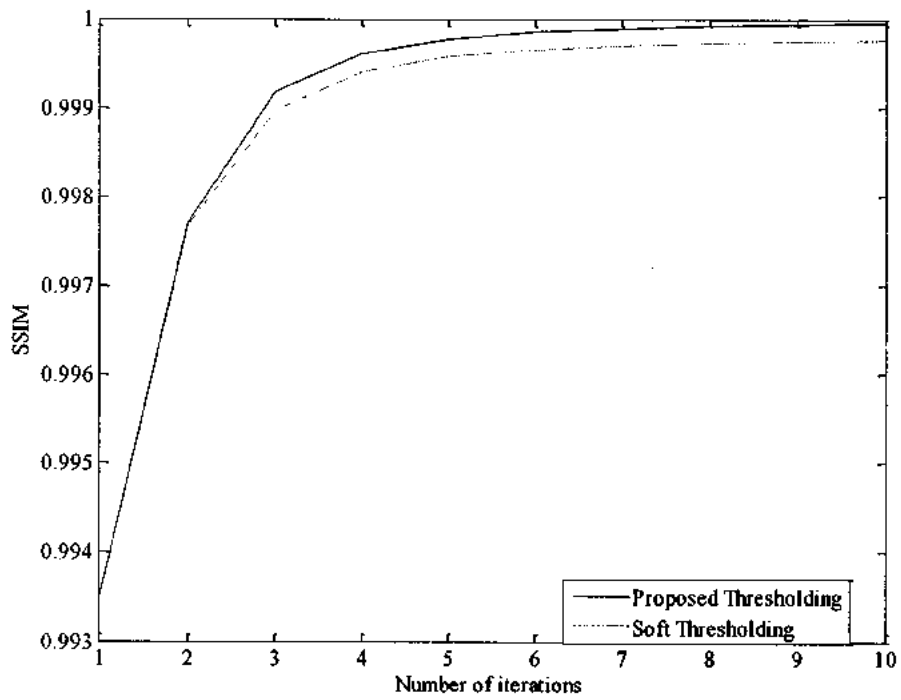


Figure-7.13: Comparison based on SSIM using two different thresholding

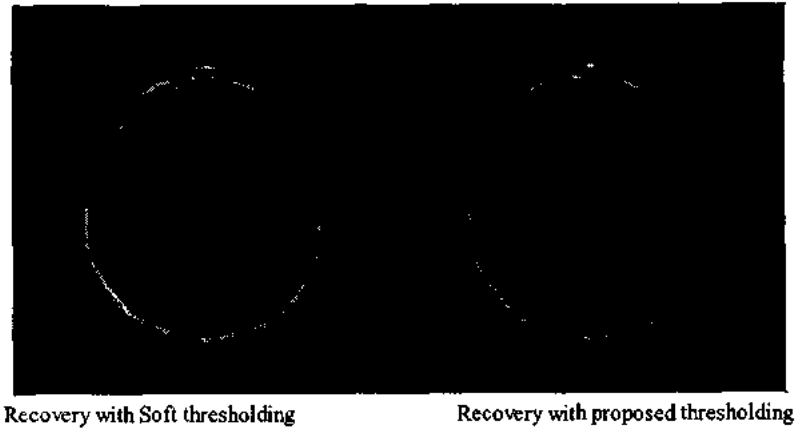


Figure-7.14: SSF based Original MR Image reconstruction using soft-thresholding (Eq-7.10) and the proposed (Eq-7.11)

7.5 Summary

This chapter explores the connection between CS recovery and denoising. Undersampling in CS essentially leads to the addition of Gaussian noise in the original image. CS recovery using iterative thresholding algorithms effectively comprise of denoising step (computing the linear estimate of the error and applying thresholding) followed by data consistency in frequency domain. Nonlinear shrinkage curves plays a vital role in the reconstruction process. A novel shrinkage function (based on hyperbolic tangent) with adjustable parameters is also presented that performs well in the CS recovery as compared to the soft-thresholding.

CHAPTER-8

CONCLUSION

8.1 Summary of thesis

Compressed sensing is a novel acquisition protocol that operates at low sampling rates and has the ability to reduce the acquisition time; a feature that is highly desirable in biomedical applications such as magnetic resonance imaging (MRI), microwave imaging (MWD) and computed tomography (CT) where conventional acquisition techniques are time consuming or require longer exposure to hazardous radiations. The application of CS to biomedical imaging modalities has shorten the acquisition time and the amount of raw data, unfortunately the computation time of the image recovery has increased. In the initial work of CS, convex optimization based methods were applied to solve the non-linear CS recovery problem. However, these general purpose reconstruction algorithms are often slow and inefficient requiring too many computations especially for high-dimensional biomedical images. The main focus of this dissertation is to propose a novel suite of algorithms that can efficiently reconstruct Fourier-encoded biomedical images from sub-sample measurements. The proposed algorithms are used to estimate the missing Fourier samples by using data-consistency in the Fourier domain and shrinkage in the sparsity domain. The techniques presented are mainly derived from the iterative-shrinkage algorithms that are widely used for image denoising.

- It has been shown that a simple projection-onto-convex set algorithm can be applied to MR and microwave imaging modalities to reconstruct the final image

from a reduced set of Fourier measurements. POCS estimates the missing samples by simply applying soft-thresholding in the sparsifying domain.

- A novel CS recovery algorithm based on separable surrogate functional (SSF) method is presented next. The update equation of SSF incorporates the linear estimate of residual error before applying non-linear shrinkage. Experimental results validate that the SSF based reconstruction yields a better image quality as compared to POCS.
- Evolutionary techniques such as genetic algorithms (GA) and particle swarm optimization (PSO) are used in combination with SSF algorithm for the recovery of 1-D sparse signals. This (heuristic-deterministic) hybrid mechanism greatly improves the convergence of GA and PSO. Based on the idea of GA, a modified POCS algorithm is also proposed for the reconstruction of Fourier encoded images. The novel recovery algorithm uses multiple initialization and randomly combines them during each iteration to estimate the original image. Introducing randomness in the recovery process provides improved results as compared to SSF based recovery.
- CS recovery algorithms generally use to reconstruct a high-quality image from the sub-sampled incoherent measurements by finding solution to the least squares optimization problem with l_1 -norm regularization. However, the l_1 -norm is not differential at the origin as the function $f(x) = |x|$ has a kink at $x = 0$. To overcome this problem, a hyperbolic tangent based approximation has been proposed. Simultaneously, a gradient based algorithm is developed for the recovery of Fourier-encoded images. The proposed technique also proves its ability to recover a sparse signal with and without the knowledge of sparsity.

- Shrinkage is an appealing and well-known denoising technique. Undersampling in CS results in an image corrupted by Gaussian-like noise. The MAP estimator of a Laplace random variable in Gaussian noise leads to the soft-thresholding. However, in practice, the assumption of Gaussian noise and Laplacian distribution of transformed coefficients may not meet exactly. Therefore, a novel hyperbolic-tangent based shrinkage is proposed that can closely approximate the non-linear soft-thresholding function. The proposed non-linear shrinkage has adjustable parameters and is shown to perform well in reconstructing biomedical images from partial Fourier measurements.

8.2 Directions for future work

There are several directions and extensions for the future research work based on the ideas presented in this dissertation. For example:

- The work can be extended to dynamic MR imaging which requires rapid data acquisition to monitor fast signal-intensity changes. Because of the computational simplicity, the proposed algorithms can be also be used with parallel imaging to reconstruct rapid dynamic volumetric MR images with high temporal resolution, spatial resolution and motion robustness.
- In the current work, analytical sparsifying transforms (dictionary) were used. The recovery process may improve if an adaptive dictionary learning mechanism is incorporated in the reconstruction. The currently used dictionary learning algorithms such as K-SVD etc. are computationally intensive. These

learning techniques usually use pursuit algorithms for sparse coding which can be easily replaced by the proposed computationally low cost algorithms.

- The proposed CS reconstruction algorithms can be used for the recovery of videos from compressed measurements. However, it may need to incorporate an intelligent sensing mechanism to exploit the high correlation in a video sequence.
- Instead of recovering the entire biomedical image at once, the iterative shrinkage based CS recovery can be extended to patch-based CS reconstruction. Additionally, the non-linear shrinkage functions/curves for each patch may be learned adaptively. This shift from global to local and adaptive modeling is expected to provide better reconstruction quality.

REFERENCES

- [1] E. J. Candès, J. Romberg, and T. Tao, "Robust uncertainty principles: Exact signal reconstruction from highly incomplete frequency information," *Information Theory, IEEE Transactions on*, vol. 52, pp. 489-509, 2006.
- [2] D. L. Donoho, "Compressed sensing," *IEEE Transactions on Information Theory*, vol. 52, pp. 1289-1306, Apr 2006.
- [3] R. G. Baraniuk, E. Candes, R. Nowak, and M. Vetterli, "Compressive sampling," *IEEE Signal Processing Magazine*, vol. 25, pp. 12-13, Mar 2008.
- [4] E. J. Candes and M. B. Wakin, "An introduction to compressive sampling," *IEEE Signal Processing Magazine*, vol. 25, pp. 21-30, Mar 2008.
- [5] J. Romberg, "Imaging via compressive sampling [introduction to compressive sampling and recovery via convex programming]," *IEEE Signal Processing Magazine*, vol. 25, pp. 14-20, 2008.
- [6] M. Lustig, D. Donoho, and J. M. Pauly, "Sparse MRI: The application of compressed sensing for rapid MR imaging," *Magnetic Resonance in Medicine*, vol. 58, pp. 1182-1195, Dec 2007.
- [7] M. Lustig, D. L. Donoho, J. M. Santos, and J. M. Pauly, "Compressed sensing MRI," *IEEE Signal Processing Magazine*, vol. 25, pp. 72-82, Mar 2008.
- [8] J. P. Haldar, D. Hernando, and Z.-P. Liang, "Compressed-sensing MRI with random encoding," *Medical Imaging, IEEE Transactions on*, vol. 30, pp. 893-903, 2011.

- [9] M. Elad and M. Aharon, "Image denoising via sparse and redundant representations over learned dictionaries," *IEEE Trans Image Process*, vol. 15, pp. 3736-45, Dec 2006.
- [10] S. Ravishankar and Y. Bresler, "MR image reconstruction from highly undersampled k-space data by dictionary learning," *Medical Imaging, IEEE Transactions on*, vol. 30, pp. 1028-1041, 2011.
- [11] V. M. Patel, R. Maleh, A. C. Gilbert, and R. Chellappa, "Gradient-Based Image Recovery Methods From Incomplete Fourier Measurements," *IEEE Transactions on Image Processing*, vol. 21, pp. 94-105, Jan 2012.
- [12] S. S. Chen, D. L. Donoho, and M. A. Saunders, "Atomic decomposition by basis pursuit," *SIAM journal on scientific computing*, vol. 20, pp. 33-61, 1998.
- [13] B. Ayazifar, "Rethinking Fourier's legacy in signals and systems education," in *Circuits and Systems (ISCAS), 2011 IEEE International Symposium on*, 2011, pp. 599-602.
- [14] P. J. Olver and C. Shakiban, "Applied linear algebra," Upper Saddle River, 2006.
- [15] E. Candes and J. Romberg, "Signal recovery from random projections," in *Proc. SPIE*, 2005, pp. 76-86.
- [16] S. Mallat, *A wavelet tour of signal processing: the sparse way*: Academic press, 2008.
- [17] G. Strang, "The discrete cosine transform," *SIAM review*, vol. 41, pp. 135-147, 1999.

- [18] V. Strela, P. N. Heller, G. Strang, P. Topiwala, and C. Heil, "The application of multiwavelet filterbanks to image processing," *Image Processing, IEEE Transactions on*, vol. 8, pp. 548-563, 1999.
- [19] M. Rabbani and D. Santa-Cruz, "The JPEG2000 still-image compression standard," in *Course given at the 2001 International Conference in Image Processing (ICIP), Thessaloniki, Greece, 2001*.
- [20] I. Bayram and M. E. Kamasak, "Directional total variation," *Signal Processing Letters, IEEE*, vol. 19, pp. 781-784, 2012.
- [21] K. Choi, J. Wang, L. Zhu, T.-S. Suh, S. Boyd, and L. Xing, "Compressed sensing based cone-beam computed tomography reconstruction with a first-order method)," *Medical physics*, vol. 37, pp. 5113-5125, 2010.
- [22] R. Baraniuk, M. Davenport, R. DeVore, and M. Wakin, "A simple proof of the restricted isometry property for random matrices," *Constructive Approximation*, vol. 28, pp. 253-263, 2008.
- [23] E. J. Candes, "The restricted isometry property and its implications for compressed sensing," *Comptes Rendus Mathematique*, vol. 346, pp. 589-592, 2008.
- [24] H. Kajbaf, R. Z. YAHONG, and R. Zoughi, "Improving Efficiency of Microwave Wideband Imaging using Compressed Sensing Techniques," *Materials evaluation*, vol. 70, pp. 1420-1432, 2012.
- [25] I. F. Gorodnitsky, J. S. George, and B. D. Rao, "Neuromagnetic source imaging with FOCUSS: a recursive weighted minimum norm algorithm,"

Electroencephalography and clinical Neurophysiology, vol. 95, pp. 231-251, 1995.

- [26] J. C. Ye, Y. Bresler, and P. Moulin, "A self-referencing level-set method for image reconstruction from sparse Fourier samples," *International Journal of Computer Vision*, vol. 50, pp. 253-270, 2002.
- [27] M. Akçakaya, S. Nam, P. Hu, M. H. Moghari, L. H. Ngo, V. Tarokh, et al., "Compressed sensing with wavelet domain dependencies for coronary MRI: a retrospective study," *Medical Imaging, IEEE Transactions on*, vol. 30, pp. 1090-1099, 2011.
- [28] M. Lustig, J. M. Santos, D. L. Donoho, and J. M. Pauly, "kt SPARSE: High frame rate dynamic MRI exploiting spatio-temporal sparsity," in *Proceedings of the 13th Annual Meeting of ISMRM, Seattle, 2006*.
- [29] L. Feng, R. Grimm, K. T. Block, H. Chandarana, S. Kim, J. Xu, et al., "Golden-angle radial sparse parallel MRI: Combination of compressed sensing, parallel imaging, and golden-angle radial sampling for fast and flexible dynamic volumetric MRI," *Magnetic Resonance in Medicine*, 2013.
- [30] S. Vasanawala, M. Murphy, M. T. Alley, P. Lai, K. Keutzer, J. M. Pauly, et al., "Practical parallel imaging compressed sensing MRI: Summary of two years of experience in accelerating body MRI of pediatric patients," in *Biomedical Imaging: From Nano to Macro, 2011 IEEE International Symposium on*, 2011, pp. 1039-1043.
- [31] M. Murphy, M. Alley, J. Demmel, K. Keutzer, S. Vasanawala, and M. Lustig, "Fast-SPIRiT compressed sensing parallel imaging MRI: scalable parallel

- implementation and clinically feasible runtime," *Medical Imaging, IEEE Transactions on*, vol. 31, pp. 1250-1262, 2012.
- [32] S. Bélanger, X. Intes, C. Casanova, F. Lesage, and M. Abran, "Real-time diffuse optical tomography based on structured illumination," *Journal of biomedical optics*, vol. 15, pp. 016006-016006-7, 2010.
- [33] J. Provost and F. Lesage, "The application of compressed sensing for photoacoustic tomography," *Medical Imaging, IEEE Transactions on*, vol. 28, pp. 585-594, 2009.
- [34] G.-H. Chen, J. Tang, and S. Leng, "Prior image constrained compressed sensing (PICCS)," in *Proc Soc Photo Opt Instrum Eng*, 2008, p. 685618.
- [35] H. Yu and G. Wang, "A soft-threshold filtering approach for reconstruction from a limited number of projections," *Physics in medicine and biology*, vol. 55, p. 3905, 2010.
- [36] Z. T. Harmany, R. F. Marcia, and R. M. Willett, "Sparsity-regularized photon-limited imaging," in *Biomedical Imaging: From Nano to Macro, 2010 IEEE International Symposium on*, 2010, pp. 772-775.
- [37] W. Ge, Y. Bresler, and V. Ntziachristos, "Guest Editorial Compressive Sensing for Biomedical Imaging," *Medical Imaging, IEEE Transactions on*, vol. 30, pp. 1013-1016, 2011.
- [38] C. Quinsac, A. Basarab, and D. Kouamé, "Frequency domain compressive sampling for ultrasound imaging," *Advances in Acoustics and Vibration*, vol. 2012, 2012.

- [39] M. Usman, D. Atkinson, F. Odille, C. Kolbitsch, G. Vaillant, T. Schaeffter, et al., "Motion corrected compressed sensing for free-breathing dynamic cardiac MRI," *Magnetic Resonance in Medicine*, vol. 70, pp. 504-516, 2013.
- [40] X. Li, "Compressed sensing and matrix completion with constant proportion of corruptions," *Constructive Approximation*, vol. 37, pp. 73-99, 2013.
- [41] J. Liu, P. Musialski, P. Wonka, and J. Ye, "Tensor completion for estimating missing values in visual data," *Pattern Analysis and Machine Intelligence, IEEE Transactions on*, vol. 35, pp. 208-220, 2013.
- [42] Q. Liu, M. Zhang, and J. Zhao, "Adaptive dictionary learning in sparse gradient domain for CT reconstruction," in *Biomedical Imaging (ISBI), 2014 IEEE 11th International Symposium on*, 2014, pp. 169-172.
- [43] J. A. Tropp and S. J. Wright, "Computational methods for sparse solution of linear inverse problems," *Proceedings of the IEEE*, vol. 98, pp. 948-958, 2010.
- [44] Y. C. Pati, R. Rezaifar, and P. Krishnaprasad, "Orthogonal matching pursuit: Recursive function approximation with applications to wavelet decomposition," in *Signals, Systems and Computers, 1993. 1993 Conference Record of The Twenty-Seventh Asilomar Conference on*, 1993, pp. 40-44.
- [45] D. L. Donoho, Y. Tsaig, I. Drori, and J.-L. Starck, "Sparse solution of underdetermined systems of linear equations by stagewise orthogonal matching pursuit," *Information Theory, IEEE Transactions on*, vol. 58, pp. 1094-1121, 2012.

- [46] D. Needell and J. A. Tropp, "CoSaMP: Iterative signal recovery from incomplete and inaccurate samples," *Applied and Computational Harmonic Analysis*, vol. 26, pp. 301-321, 2009.
- [47] J. Z. Duan, Y. Liu, and L. Y. Zhang, "Bregman Iteration Based Efficient Algorithm for MR Image Reconstruction From Undersampled K-Space Data," *IEEE Signal Processing Letters*, vol. 20, pp. 831-834, Aug 2013.
- [48] M. A. Figueiredo, R. D. Nowak, and S. J. Wright, "Gradient projection for sparse reconstruction: Application to compressed sensing and other inverse problems," *Selected Topics in Signal Processing, IEEE Journal of*, vol. 1, pp. 586-597, 2007.
- [49] S. J. Wright, R. D. Nowak, and M. A. Figueiredo, "Sparse reconstruction by separable approximation," *Signal Processing, IEEE Transactions on*, vol. 57, pp. 2479-2493, 2009.
- [50] Y. Le Montagner, E. Angelini, and J.-C. Olivo-Marin, "Comparison of reconstruction algorithms in compressed sensing applied to biological imaging," in *Biomedical Imaging: From Nano to Macro, 2011 IEEE International Symposium on*, 2011, pp. 105-108.
- [51] C. A. Metzler, A. Maleki, and R. G. Baraniuk, "From denoising to compressed sensing," *arXiv preprint arXiv:1406.4175*, 2014.
- [52] J. Jin, B. Yang, K. Liang, and X. Wang, "General image denoising framework based on compressive sensing theory," *Computers & Graphics*, vol. 38, pp. 382-391, 2014.

- [53] M. Elad, "Why simple shrinkage is still relevant for redundant representations?," *Information Theory, IEEE Transactions on*, vol. 52, pp. 5559-5569, 2006.
- [54] T. Blumensath, "Accelerated iterative hard thresholding," *Signal Processing*, vol. 92, pp. 752-756, 2012.
- [55] A. Beck and M. Teboulle, "A Fast Iterative Shrinkage-Thresholding Algorithm for Linear Inverse Problems," *Siam Journal on Imaging Sciences*, vol. 2, pp. 183-202, 2009.
- [56] M. Elad, B. Matalon, and M. Zibulevsky, "Coordinate and subspace optimization methods for linear least squares with non-quadratic regularization," *Applied and Computational Harmonic Analysis*, vol. 23, pp. 346-367, 2007.
- [57] M. Zibulevsky and M. Elad, "L1-L2 Optimization in Signal and Image Processing," *IEEE Signal Processing Magazine*, vol. 27, pp. 76-88, May 2010.
- [58] Z. Wang, A. C. Bovik, H. R. Sheikh, and E. P. Simoncelli, "Image quality assessment: from error visibility to structural similarity," *Image Processing, IEEE Transactions on*, vol. 13, pp. 600-612, 2004.
- [59] D. W. McRobbie, E. A. Moore, M. J. Graves, and M. R. Prince, *MRI from Picture to Proton: Cambridge University Press*, 2006.
- [60] T. Schaeffter, M. S. Hansen, and T. S. Sørensen, "Fast Implementation of Iterative Image Reconstruction," in *International Society for Magnetic Resonance in Medicine*.

- [61] H. Omer and R. Dickinson, "Regularization in Parallel MR Image Reconstruction," *Concepts in Magnetic Resonance Part A*, vol. 38A, pp. 52-60, Mar 2011.
- [62] C. M. Tsai and D. G. Nishimura, "Reduced aliasing artifacts using variable-density k-space sampling trajectories," *Magnetic resonance in medicine*, vol. 43, pp. 452-458, 2000.
- [63] R. Cierniak and M. Butynski, *X-ray computed tomography in biomedical engineering*: Springer, 2011.
- [64] O. Barkan, A. Averbuch, S. Dekel, and Y. Tenzer, "A Mathematical Model for Extremely Low Dose Adaptive Computed Tomography Acquisition," in *Mathematical Methods for Curves and Surfaces*, ed: Springer, 2014, pp. 13-33.
- [65] R. Maleh, "Efficient sparse approximation methods for medical imaging," The University of Michigan, 2009.
- [66] Z. Wang, E. G. Lim, Y. Tang, and M. Leach, "Medical Applications of Microwave Imaging," *The Scientific World Journal*, vol. 2014, 2014.
- [67] D. M. Sheen, D. L. McMakin, and T. E. Hall, "Three-dimensional millimeter-wave imaging for concealed weapon detection," *Microwave Theory and Techniques, IEEE Transactions on*, vol. 49, pp. 1581-1592, 2001.
- [68] B. Zhang, W. Hong, and Y. Wu, "Sparse microwave imaging: Principles and applications," *Science China Information Sciences*, vol. 55, pp. 1722-1754, 2012.

- [69] L. C. Potter, E. Ertin, J. T. Parker, and M. Cetin, "Sparsity and compressed sensing in radar imaging," *Proceedings of the IEEE*, vol. 98, pp. 1006-1020, 2010.
- [70] L. Bregman, "The method of successive projection for finding a common point of convex sets (Theorems for determining common point of convex sets by method of successive projection)," *Soviet Mathematics*, vol. 6, pp. 688-692, 1965.
- [71] D. C. Youla and H. Webb, "Image Restoration by the Method of Convex Projections: Part 1 Theory," *Medical Imaging, IEEE Transactions on*, vol. 1, pp. 81-94, 1982.
- [72] M. Elad, B. Matalon, J. Shtok, and M. Zibulevsky, "A wide-angle view at iterated shrinkage algorithms," in *Optical Engineering+ Applications, 2007*, pp. 670102-670102-19.
- [73] M. Elad, *Sparse and redundant representations: from theory to applications in signal and image processing*: Springer, 2010.
- [74] M. Lustig, D. Donoho, and J. Pauly, "Rapid MR imaging with compressed sensing and randomly under-sampled 3DFT trajectories," in *Proc. 14th Ann. Meeting ISMRM, 2006*.
- [75] U. Gamper, P. Boesiger, and S. Kozerke, "Compressed sensing in dynamic MRI," *Magnetic Resonance in Medicine*, vol. 59, pp. 365-373, 2008.
- [76] G. A. Wright, "Magnetic resonance imaging," *IEEE Signal Processing Magazine*, vol. 14, pp. 56-66, Jan 1997.

- [77] M. K. Stehling, R. Turner, and P. Mansfield, "Echo-planar imaging: magnetic resonance imaging in a fraction of a second," *Science*, vol. 254, pp. 43-50, 1991.
- [78] F. Schmitt, M. K. Stehling, and R. Turner, "Echo-planar imaging," 1998.
- [79] M. Lustig and J. M. Pauly, "SPIRiT: Iterative self-consistent parallel imaging reconstruction from arbitrary k-space," *Magnetic Resonance in Medicine*, vol. 64, pp. 457-471, 2010.
- [80] K. Scheffler and J. Hennig, "Reduced circular field-of-view imaging," *Magnetic resonance in medicine*, vol. 40, pp. 474-480, 1998.
- [81] A. Deshmane, V. Gulani, M. A. Griswold, and N. Seiberlich, "Parallel MR imaging," *Journal of Magnetic Resonance Imaging*, vol. 36, pp. 55-72, 2012.
- [82] K. P. Pruessmann, "Encoding and reconstruction in parallel MRI," *NMR in Biomedicine*, vol. 19, pp. 288-299, 2006.
- [83] L. Grady and J. R. Polimeni, "Method for reconstructing images of an imaged subject from a parallel MRI acquisition," ed: Google Patents, 2014.
- [84] M. Uecker, P. Lai, M. J. Murphy, P. Virtue, M. Elad, J. M. Pauly, et al., "ESPIRiT—an eigenvalue approach to autocalibrating parallel MRI: where SENSE meets GRAPPA," *Magnetic Resonance in Medicine*, vol. 71, pp. 990-1001, 2014.
- [85] K. L. Wright, J. I. Hamilton, M. A. Griswold, V. Gulani, and N. Seiberlich, "Non-Cartesian parallel imaging reconstruction," *Journal of Magnetic Resonance Imaging*, vol. 40, pp. 1022-1040, 2014.

- [86] D. h. Kim, E. Adalsteinsson, and D. M. Spielman, "Simple analytic variable density spiral design," *Magnetic resonance in medicine*, vol. 50, pp. 214-219, 2003.
- [87] X. Li, S. Luo, A. Talbert, R. Eisner, and F. DiBianca, "A compressed sensing-based iterative algorithm for CT reconstruction and its possible application to phase contrast imaging," *Biomed Eng Online*, vol. 10, pp. 1-14, 2011.
- [88] H. Kudo, "Introduction to advanced image reconstruction methods and compressed sensing in medical computed tomography," *Microscopy*, vol. 63, pp. i15-i15, 2014.
- [89] R. Chartrand, E. Y. Sidky, and X. Pan, "Nonconvex compressive sensing for X-ray CT: an algorithm comparison," in *Signals, Systems and Computers, 2013 Asilomar Conference on*, 2013, pp. 665-669.
- [90] S. Uğur and O. Arikan, "SAR image reconstruction and autofocus by compressed sensing," *Digital Signal Processing*, vol. 22, pp. 923-932, 2012.
- [91] G. Oliveri, L. Poli, and A. Massa, "On the exploitation of the a-priori information through the Bayesian compressive sensing for microwave imaging," in *Antennas and Propagation (EUCAP), 2012 6th European Conference on*, 2012, pp. 1502-1503.
- [92] A. Korn, M. Fenchel, B. Bender, S. Danz, T.-K. Hauser, D. Ketelsen, et al., "Iterative reconstruction in head CT: image quality of routine and low-dose protocols in comparison with standard filtered back-projection," *American journal of neuroradiology*, vol. 33, pp. 218-224, 2012.

- [93] A. Moscariello, R. A. Takx, U. J. Schoepf, M. Renker, P. L. Zwerner, T. X. O'Brien, et al., "Coronary CT angiography: image quality, diagnostic accuracy, and potential for radiation dose reduction using a novel iterative image reconstruction technique—comparison with traditional filtered back projection," *European radiology*, vol. 21, pp. 2130-2138, 2011.
- [94] P. L. Combettes and J.-C. Pesquet, "Proximal splitting methods in signal processing," in *Fixed-point algorithms for inverse problems in science and engineering*, ed: Springer, 2011, pp. 185-212.
- [95] E. Gopi, *Algorithm collections for digital signal processing applications using Matlab: Springer Science & Business Media*, 2007.
- [96] B. Craenen, A. Eiben, and E. Marchiori, "How to handle constraints with evolutionary algorithms," *Practical Handbook Of Genetic Algorithms: Applications*, pp. 341-361, 2001.
- [97] G. T. Pulido and C. A. C. Coello, "A constraint-handling mechanism for particle swarm optimization," in *Evolutionary Computation, 2004. CEC2004. Congress on, 2004*, pp. 1396-1403.
- [98] Y. Wang, Z. Cai, Y. Zhou, and Z. Fan, "Constrained optimization based on hybrid evolutionary algorithm and adaptive constraint-handling technique," *Structural and Multidisciplinary Optimization*, vol. 37, pp. 395-413, 2009.
- [99] G. Coath and S. Halgamuge, "A comparison of constraint-handling methods for the application of particle swarm optimization to constrained nonlinear optimization problems," in *Evolutionary Computation, 2003. CEC'03. The 2003 Congress on, 2003*, pp. 2419-2425.

- [100] J. A. Shah, I. Qureshi, A. A. Khaliq, and H. Omer, "Sparse Signal Recovery based on Hybrid Genetic Algorithm," *Research Journal of Recent Sciences*, vol. 2277, p. 2502, 2013.
- [101] J. Kennedy, "Particle swarm optimization," in *Encyclopedia of Machine Learning*, ed: Springer, 2010, pp. 760-766.
- [102] G. Venter and J. Sobieszczanski-Sobieski, "Particle swarm optimization," *AIAA journal*, vol. 41, pp. 1583-1589, 2003.
- [103] Y. Shi, "Particle swarm optimization," *IEEE Connections*, vol. 2, pp. 8-13, 2004.
- [104] R. Poli, J. Kennedy, and T. Blackwell, "Particle swarm optimization," *Swarm intelligence*, vol. 1, pp. 33-57, 2007.
- [105] M. Clerc, *Particle swarm optimization* vol. 93: John Wiley & Sons, 2010.
- [106] R. C. Eberhart and Y. Shi, "Particle swarm optimization: developments, applications and resources," in *Evolutionary Computation, 2001. Proceedings of the 2001 Congress on*, 2001, pp. 81-86.
- [107] K. De Jong, "Learning with genetic algorithms: An overview," *Machine learning*, vol. 3, pp. 121-138, 1988.
- [108] M. Mitchell, "Genetic algorithms: An overview," *Complexity*, vol. 1, pp. 31-39, 1995.
- [109] M. Mitchell, *An introduction to genetic algorithms*: MIT press, 1998.
- [110] R. L. Haupt and S. E. Haupt, *Practical genetic algorithms*: John Wiley & Sons, 2004.

- [111] C. R. Houck, J. Joines, and M. G. Kay, "A genetic algorithm for function optimization: a Matlab implementation," NCSU-IE TR, vol. 95, 1995.
- [112] L. J. Eshelman and J. D. Schaffer, "Preventing Premature Convergence in Genetic Algorithms by Preventing Incest," in ICGA, 1991, pp. 115-122.
- [113] M. Rocha and J. Neves, "Preventing premature convergence to local optima in genetic algorithms via random offspring generation," in Multiple Approaches to Intelligent Systems, ed: Springer, 1999, pp. 127-136.
- [114] M. Schoenauer and S. Xanthakis, "Constrained GA Optimization," in ICGA, 1993, pp. 573-580.
- [115] B. Widrow, J. M. McCool, M. Larimore, and C. R. Johnson, "Stationary and nonstationary learning characteristics of the LMS adaptive filter," Proceedings of the IEEE, vol. 64, pp. 1151-1162, 1976.
- [116] S. S. Haykin, Adaptive filter theory: Pearson Education India, 2008.
- [117] J. R. Treichler, C. R. Johnson, and M. G. Larimore, Theory and design of adaptive filters: Wiley, 1987.
- [118] H. R. Miller, Optimization: foundations and applications: John Wiley & Sons, 2011.
- [119] S. Boyd and L. Vandenberghe, Convex optimization: Cambridge university press, 2004.
- [120] S. Grossberg, "Nonlinear neural networks: Principles, mechanisms, and architectures," Neural networks, vol. 1, pp. 17-61, 1988.

- [121] S. S. Haykin, S. S. Haykin, S. S. Haykin, and S. S. Haykin, *Neural networks and learning machines vol. 3: Pearson Education Upper Saddle River, 2009.*
- [122] B. I. Yun, "A non-iterative method for solving non-linear equations," *Applied Mathematics and Computation*, vol. 198, pp. 691-699, 2008.
- [123] A. Menon, K. Mehrotra, C. K. Mohan, and S. Ranka, "Characterization of a class of sigmoid functions with applications to neural networks," *Neural Networks*, vol. 9, pp. 819-835, 1996.
- [124] B. L. Kalman and S. C. Kwasny, "Why Tanh: choosing a sigmoidal function," in *Neural Networks, 1992. IJCNN., International Joint Conference on, 1992*, pp. 578-581.
- [125] X.-F. Fang, J.-S. Zhang, and Y.-Q. Li, "Sparse Signal Reconstruction Based on Multiparameter Approximation Function with Smoothed Norm," *Mathematical Problems in Engineering*, vol. 2014, p. 9, 2014.
- [126] W. Wang and Q. Wang, "Approximated Function Based Spectral Gradient Algorithm for Sparse Signal Recovery," *Statistics, Optimization & Information Computing*, vol. 2, pp. 10-20, 2014.
- [127] J. Barzilai and J. M. Borwein, "Two-point step size gradient methods," *IMA Journal of Numerical Analysis*, vol. 8, pp. 141-148, 1988.
- [128] D. L. Donoho, "De-noising by soft-thresholding," *Information Theory, IEEE Transactions on*, vol. 41, pp. 613-627, 1995.
- [129] F. Luisier, T. Blu, and M. Unser, "A new SURE approach to image denoising: Interscale orthonormal wavelet thresholding," *Image Processing, IEEE Transactions on*, vol. 16, pp. 593-606, 2007.

- [130] S. G. Chang, B. Yu, and M. Vetterli, "Adaptive wavelet thresholding for image denoising and compression," *Image Processing, IEEE Transactions on*, vol. 9, pp. 1532-1546, 2000.
- [131] I. K. Fodor and C. Kamath, "Denoising through wavelet shrinkage: an empirical study," *Journal of Electronic Imaging*, vol. 12, pp. 151-160, 2003.
- [132] R. Rangarajan, R. Venkataramanan, and S. Shah, "Image denoising using wavelets," *Wavelet and Time Frequencies*, 2002.
- [133] L. Breiman, "Better subset regression using the nonnegative garrote," *Technometrics*, vol. 37, pp. 373-384, 1995.
- [134] L. Sendur and I. W. Selesnick, "Bivariate shrinkage functions for wavelet-based denoising exploiting interscale dependency," *Signal Processing, IEEE Transactions on*, vol. 50, pp. 2744-2756, 2002.
- [135] M. Nasri and H. Nezamabadi-pour, "Image denoising in the wavelet domain using a new adaptive thresholding function," *Neurocomputing*, vol. 72, pp. 1012-1025, 2009.
- [136] J. Prinosil, Z. Smekal, and K. Bartusek, "Wavelet thresholding techniques in MRI domain," in *Biosciences (BIOSCIENCESWORLD), 2010 International Conference on*, 2010, pp. 58-63.